

10. Site 845¹

Shipboard Scientific Party²

HOLE 845A

Date occupied: 13 May 1991
Date departed: 16 May 1991
Time on hole: 2 days, 11 hr, 58 min
Position: 9°34.950'N, 94°35.448'W
Bottom felt (rig floor; m, drill-pipe measurement): 3715.9
Distance between rig floor and sea level (m): 11.7
Water depth (drill-pipe measurement from sea level, m): 3704.2
Total depth (rig floor; m): 4007.5
Penetration (m): 291.6
Number of cores (including cores with no recovery): 31
Total length of cored section (m): 291.6
Total core recovered (m): 292.63
Core recovery (%): 100.4
Oldest sediment cored:
Depth (mbsf): 291.60
Nature: foraminifer nannofossil ooze and metalliferous sediment
Earliest age: early Miocene

HOLE 845B

Date occupied: 16 May 1991
Date departed: 17 May 1991
Time on hole: 22 hr, 51 min
Position: 9°34.931'N, 94°35.376'W
Bottom felt (rig floor; m, drill-pipe measurement): 3715.9
Distance between rig floor and sea level (m): 11.7
Water depth (drill-pipe measurement from sea level, m): 3704.2
Total depth (rig floor; m): 3918.5
Penetration (m): 202.6
Number of cores (including cores with no recovery): 21
Total length of cored section (m): 199.5
Total core recovered (m): 195.23
Core recovery (%): 97.9
Oldest sediment cored:
Depth (mbsf): 202.6
Nature: foraminifer nannofossil ooze
Earliest age: middle Miocene

HOLE 845C

Date occupied: 17 May 1991
Date departed: 17 May 1991
Time on hole: 10 hr, 4 min
Position: 9°34.985'N, 94°35.383'W
Bottom felt (rig floor; m, drill-pipe measurement): 3715.9
Distance between rig floor and sea level (m): 11.70
Water depth (drill-pipe measurement from sea level, m): 3704.2
Total depth (rig floor; m): 3764.4
Penetration (m): 48.5
Number of cores (including cores with no recovery): 3
Total length of cored section (m): 28.5
Total core recovered (m): 29.49
Core recovery (%): 103.5
Oldest sediment cored:
Depth (mbsf): 48.5
Nature: diatom radiolarian clay
Earliest age: Pliocene

Principal results: Site 845 (proposed Site EEQ-1), the northernmost site of Leg 138's eastern transect, is located in the Guatemala Basin of the eastern equatorial Pacific Ocean. Oceanographically, the site is in an area affected by both the westward-flowing North Equatorial Current (NEC) and the eastward-flowing North Equatorial Countercurrent (NECC). Our primary paleoceanographic objectives at Site 845 were (1) to collect a continuous, late Neogene high-resolution record of the paleoclimatic and paleoceanographic variabilities in this region and (2) to take advantage of the significant terrigenous component expected at this site to calibrate equatorial biostratigraphies with the paleomagnetic record.

Three holes were drilled at the site. Hole 845A was APC-cored to 207.1 mbsf, where excessive pullout required us to switch to XCB-coring. Drilling with the XCB continued in the hole to 291.6 mbsf, where basement was reached. Hole 845B was APC-cored to 202.6 mbsf. The interval between 20 and 48.5 mbsf was APC-cored (Hole 845C) to recover overlapping sections in an interval that was missed at Holes 845A and 845B. Compilation of magnetic susceptibility, GRAPE density, and color spectral reflectance data shows that a continuous section from the upper 207 mbsf was recovered with APC-coring.

The sediment sequence can be divided into two lithologic units. Lithologic Unit I (0–136 mbsf) is an upper Miocene–Pleistocene diatom and radiolarian clay having only one isolated occurrence of pelagic carbonate. Unit II (136–291 mbsf) is a lower Miocene to upper Miocene section of mainly nannofossil ooze, with a distinctive transitional siliceous-carbonate interval that includes clay- and iron-rich horizons at its top and a thin sequence of metalliferous sediments above the basaltic basement.

This continuous sedimentary section spans the time interval from the late Pleistocene to the early Miocene. Biostratigraphic age control was provided by all four of the chief planktonic microfossil groups, in addition to an excellent continuous paleomagnetic record that spanned the early Pliocene to middle Miocene. Calcareous nannofossils, radiolarians, and diatoms generally are present throughout the sequence and provide a

¹Mayer, L., Piasias, N., Janecek, T., et al., 1992. *Proc. ODP, Init. Repts.*, 138: College Station, TX (Ocean Drilling Program).

²Shipboard Scientific Party is as given in list of participants preceding the contents.

well-constrained biostratigraphy. Planktonic foraminifers are rare to absent in the upper half of the section, but are common to abundant through the remaining cored interval. Calcareous nannofossils have been dissolved in the Pliocene–Pleistocene section and show good preservation in the lower-to-middle Miocene sediments.

Paleomagnetic results from Site 845 indicate that a continuous and unambiguous paleomagnetic stratigraphy was recovered from the interval between 50 and 200 mbsf, which represents a 10-m.y. period from the middle Miocene (approximately 13.4 Ma) to the middle Pliocene (about 2.7 Ma.). In the upper 50 m, magnetization was too weak to be interpreted (possibly the result of high organic carbon content in this interval that may have resulted in the dissolution of magnetic minerals). For the middle Miocene section, however, Site 845 provided a high-resolution polarity record showing three short normal polarity features (Chronos C3A, C4, and C4A) that have not been recognized by currently accepted magnetic polarity time scales.

Three logging runs were conducted in Hole 845B using the standard lithostratigraphic string, the geochemical string, and the formation microscanner (FMS). Logs were of excellent quality and provided an important cross-check with both continuous and discrete physical properties measured in the laboratory. Logging units, defined by changes in the shape of the logs, correlate well with the independently determined lithologic units.

The 17-m.y. basement age is significantly older than the basement age estimated from subsidence modeling or calculated spreading from the East Pacific Rise. Recent published plate reconstructions suggest a basement age of less than 15 Ma for this site. Basement age estimates from DSDP Site 495 and results from Site 845 suggest early Miocene spreading rates of up to 81 mm/yr for this sector of the eastern Pacific Ocean. If the Berlanga Rise is a fossil spreading center, as proposed by Klitgord and Mammerickx (1982), then the estimated age of extinction is about 15 Ma.

The combination of complete recovery; well-defined magnetostratigraphy and biostratigraphy; multiple, continuous, high-resolution laboratory records (GRAPE, *P*-wave velocity, susceptibility, and color); and an excellent suite of logs ensure that Site 845 will be a silver mine for high-resolution paleoclimate and paleoceanographic studies, particularly for the middle Miocene.

BACKGROUND AND SCIENTIFIC OBJECTIVES

Site 845 is the northernmost drilling site in the eastern transect of Leg 138. This site is situated beneath the NEC near the boundary between this current and the eastward-flowing NECC (Fig. 1). This boundary is a zone of divergence-driven upwelling. The NEC is also a region influenced by southward advection from the eastern boundary current of the North Pacific Ocean—the southern continuation of the California Current (CAC).

Before drilling, we estimated that the site rested on 15-m.y.-old crust that had been generated at the East Pacific Rise. Magnetic anomalies in the region have been mapped, but not have not been correlated to a known magnetic sequence (Klitgord and Mammerickx, 1982). The 15-m.y. crustal age was based on present-day Cocos–Pacific Plate spreading rates and on subsidence calculations using the depth of the site. However, the site is located east of a topographic swell known as the Berlanga Rise, which is thought to be a fossil spreading center (Klitgord and Mammerickx, 1982; Fig. 2). Both Klitgord and Mammerickx (1982) and van Andel et al. (1975) suggest fossil spreading centers south of the Siqueiros Fracture Zone to account for the basement ages of DSDP Site 495 to the east of ODP Site 845 and for DSDP Site 79 to the west. This fossil spreading segment, however, has been mapped west of the present East Pacific Rise. It has been suggested that two spreading centers were active to account for the observed basement ages. The cessation of spreading on the segment to the west of the East Pacific Rise has been indirectly estimated to have occurred 10 to 11 Ma (Klitgord and Mammerickx, 1982).

Specific objectives addressed at Site 845 include

1. Calibration of equatorial biostratigraphies to the paleomagnetic time scale—a good magnetic record was expected as a result of the large component of terrigenous influx at this site.
2. Examination of the late Neogene record of the NEC and the influence of the North Pacific eastern boundary current on equatorial circulation and productivity. The southward backtracked path would allow the site to provide a record of the ancestral NECC.
3. Determination of basement age to help identify the previously undated magnetic anomaly sequence of the Guatemala Basin.

Seismic and SeaBeam bathymetric data collected during the site survey cruise (*Thomas Washington* Venture 1; see Mayer et al., this volume) reveal that the surficial relief in the area is moderate (50–100 m) although a pronounced northwest-southeast trend exists (Fig. 3). While basement relief also is moderate, the basement surface is rough, resulting in scattering and absence of coherency in the seismic reflection profiles from most of this area. The site is located in a small region where the basement reflector becomes smooth and the overlying sediment section shows continuous and undisturbed seismic reflections (Fig. 4). The section at Site 845 is 0.369 s (two-way traveltime) thick, which represents a thickness of 290 m.

OPERATIONS

Transit from Site 844 to Site 845

The transit from Site 844 to Site 845 covered 257 nmi to the first survey way point, at an average speed of 10.6 kt. The site survey for Site 845 began at 1648 hr (local time, L; all times reported in this section are local time, that is Universal Time Coordinated, UTC, minus 6 hr. All times in Table 1 are in UTC), 13 May 1991. At 1830L 13 May, a beacon was deployed successfully, and the survey was concluded at 1918L, 13 May. The depth to seafloor, based upon the precision depth recorder (PDR), was 3720.4 mbrf.

Hole 845A

Core 138-845A-1H was taken at 0315L 14 May at a depth of 3715.9 mbrf and 7.62 m of sediments was recovered. Cores 138-845A-2H through -21H were recovered successfully from 7.6 to 197.6 mbsf, with orientation of the APC cores beginning with Core 138-845A-4H (see Table 1 for coring statistics). An overpull of 60,000 lb was required to retrieve the core barrel at Core 138-845A-22H (197.6–207.1 mbsf), which forced termination of the APC-coring program for this hole. The average sediment recovery for the APC section at Hole 845A was 104.8%.

Coring resumed with the XCB-coring system at Core 138-845A-23X and advanced with no problems to Core 138-845A-31X (207.1–291.6 mbsf), where contact with the basement was confirmed by the recovery of 1.49 m of basalt. The depth objective for the hole was reached at this point, and it then was prepared for logging. The average sediment recovery for the XCB section of Hole 845A was 89.6%.

Downhole Measurements, Hole 845A

After the hole was swept with mud, the pipe was pulled back to 62.1 mbsf and then three standard ODP tool strings were run. A summary of these operations is presented in Table 2.

The geophysical tool string was run first, and the heave compensator was used for both the main and subsequent logging passes. The main logging run was from 292 to 100 mbsf, with a repeat run from 170.4 to 99.1 mbsf. No problems were encountered during either run.

The geochemical tool was run next, and minor problems were encountered during calibration of the string. One of the high voltage circuits was too far out of range for the feedback circuitry to correct the problem. The voltage on this circuit was reset manually, after

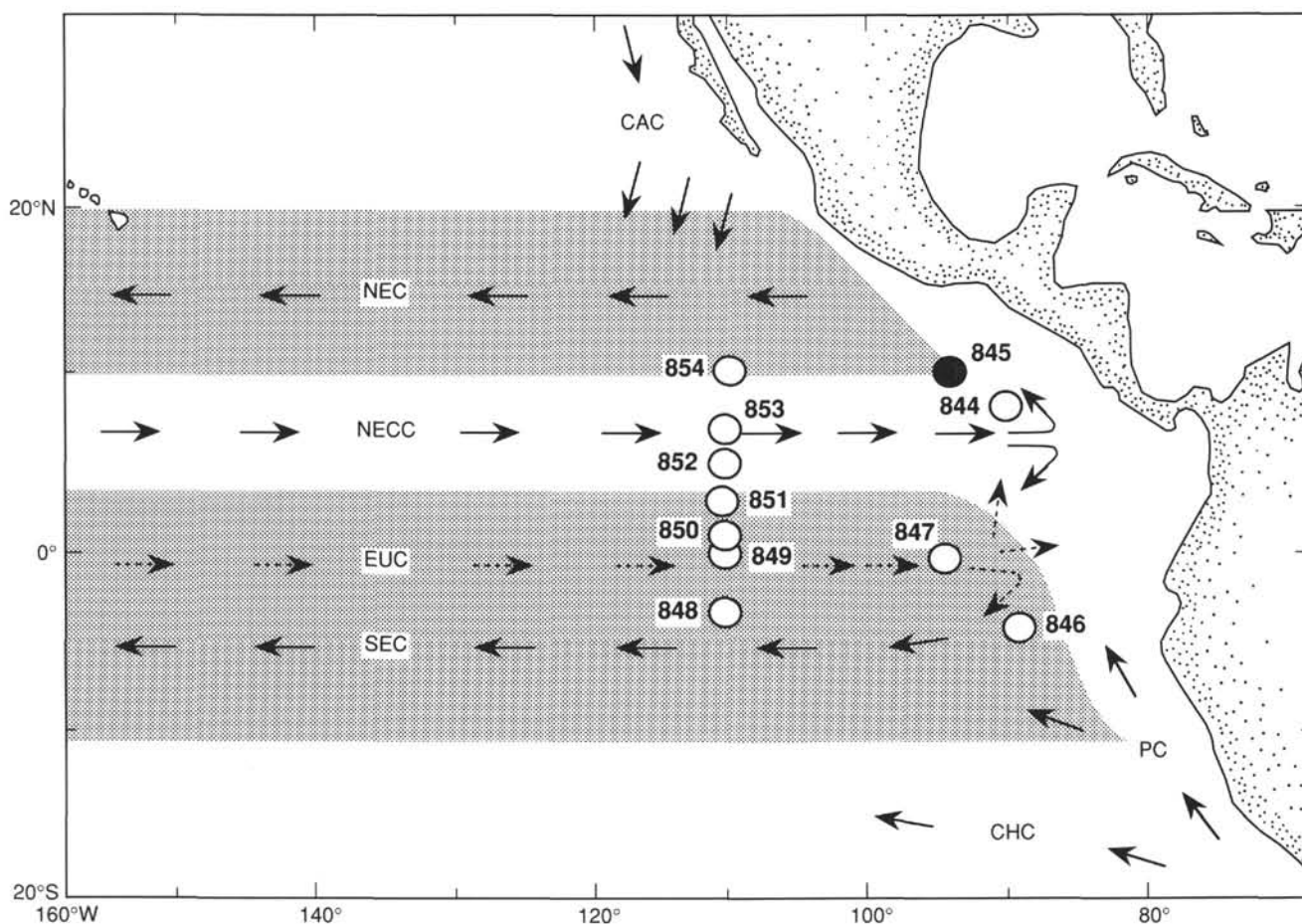


Figure 1. Site location and generalized circulation system of the eastern equatorial Pacific Ocean. Surface current shown as solid arrows; subsurface current as dashed arrows. CAC = California Current; NEC = North Equatorial Current; NECC = North Equatorial Countercurrent; EUC = Equatorial Undercurrent; SEC = South Equatorial Current; PC = Peru Current; and CHC = Chile Current. Shaded areas illustrate general latitudinal extent of the SEC and NEC.

which, the tool worked properly. During the time that the problem was being traced, the tool string was moved upward at a rate of 300 ft/hr (to 137.5 mbsf) to minimize neutron activation of hot spots in the borehole. Nevertheless, when examining the natural gamma-ray logs over the interval from the base of the hole to 137.5 mbsf one should take care because the formation may have been activated. Once the system was calibrated and the tool lowered to total depth (291.6 mbsf), logging was performed from the base of the hole up to the mud line with no further problems.

The third logging run (using the FMS) proceeded smoothly. Two runs were performed, one from 291.3 to 155.1 mbsf, and a second from 291.5 to 69.8 mbsf. No problems were encountered during either pass.

At the conclusion of the logging program, the drill string was pulled out of the hole. The bit cleared the mud line at 0629L, 16 May, which officially ended Hole 845A.

Hole 845B

The vessel was offset 20 m south and Hole 845B was begun by washing down to 3.1 mbsf. This starting depth for coring operations in Hole 845B corresponds to a 5-m vertical offset relative to Hole 845A. Core 138-845B-1H (3.1–12.6 mbsf) was recovered at 0810L 16 May, and coring continued until the depth objective at Core 138-845B-21H (202.6 mbsf) was reached. Every APC core was then oriented, starting with Core 138-845B-4H. During operations at this hole, wave height varied between 6 and 9 ft, with a ship's heave of 4 to 7 ft. These conditions probably were responsible for the lower than

expected recovery in the upper portion of the hole. After Core 138-845B-21H was retrieved, the pipe was pulled above the mud line to begin Hole 845C. Average sediment recovery for Hole 845B was 97.9%.

Hole 845C

The vessel was offset 20 m west, and Hole 845C was begun at 0600L 17 May, by washing it down to 20 mbsf. Three APC cores were retrieved over the interval from 20.0 to 48.5 mbsf to ensure that recovery overlapped with the other holes in the upper 50 m of the sedimentary section. After Core 138-845C-3H was retrieved, the drill string was pulled out of the hole and the bit was brought on deck at 1450L 17 May (Larry Mayer's birthday).

Concurrent with pulling out of the hole, a beacon was released remotely, and it reached the surface in 45 min. The crane operator easily plucked the unit out of the water, despite 6-ft seas. The hydrophones and thrusters were retracted, and the vessel was under way to Baltra in the Galapagos Islands at 1530L 17 May.

LITHOSTRATIGRAPHY

Introduction

The sediments at Site 845 comprise upper Miocene to Pleistocene diatom and radiolarian clays having only localized carbonate, underlain by upper-to-lower Miocene nannofossil oozes (Fig. 5). A complete sedimentary section was recovered above the basement, which was overlain by a thin sequence of metalliferous sediments.

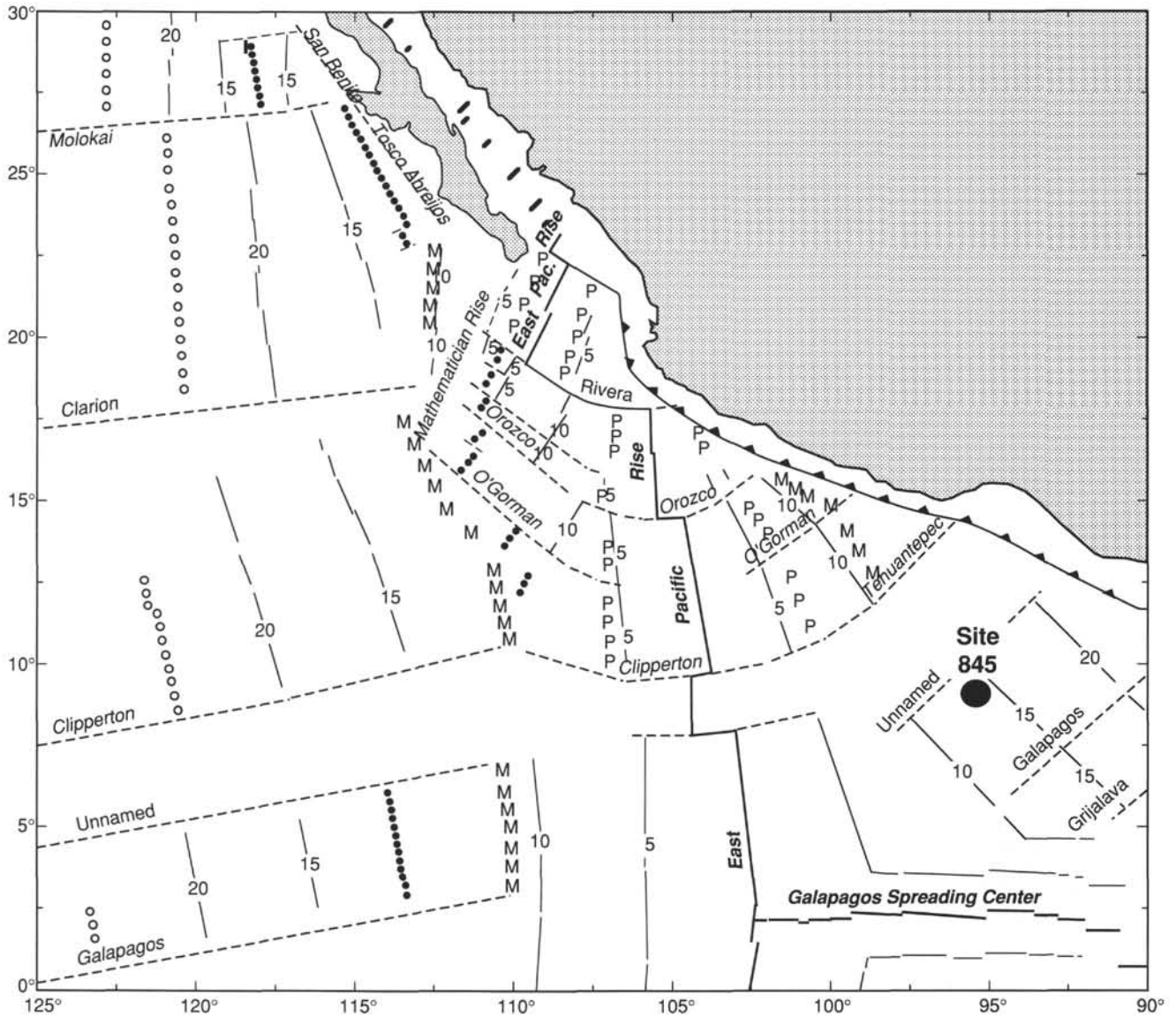


Figure 2. Tectonic setting and ages of basement for the eastern equator Pacific Ocean (from Hey, 1977) with location of Site 845 shown for reference.

We classified the sediments at Site 845 and then divided them into lithostratigraphic units primarily on the basis of visual core description; analysis of sediment composition obtained from smear slides (Fig. 6); and analyses of carbonate contents, X-ray diffraction, and X-ray fluorescence data. Other continuously measured lithologic parameters, including density (GRAPE), magnetic susceptibility, automated color analysis data, and downhole logs also were used to help us characterize the lithologies (Fig. 7). Fine-scale correlation among holes was performed on the basis of matching continuous densities (GRAPE), magnetic susceptibilities, and continuously measured color data, as well as on the basis of sedimentological features. These multiparameter data also were used to identify coring gaps and overlaps among holes. For Site 845, color data were particularly useful for verifying correlation between marker horizons and unit subdivisions. These color variations are summarized in Figure 8 and below.

The sediments from Site 845 were divided into two lithologic units (Fig. 5). Unit I is dominantly diatom and radiolarian clay that indicated only one isolated interval of carbonate (nanofossil-rich) sediment. Unit II comprises mainly nanofossil ooze, with a distinctive transitional siliceous/carbonate interval that includes clay- and oxide-

rich horizons at the top and a thin sequence of metalliferous sediments immediately above basaltic basement.

Description of Units

Unit I

Intervals:

- Hole 845A, Cores 138-845A-1H through -15H-4, 103 cm
- Hole 845B, Cores 138-845B-1H through -14H-7, 61 cm
- Hole 845C, Cores 138-845C-1H through -3H

Age: Pleistocene to late Miocene

Depth: 0-135.63 mbsf, Hole 845A; 0-136.23 mbsf, Hole 845B; 20-48.5 mbsf, Hole 845C

Unit I comprises predominantly clay-, radiolarian-, and diatom-rich sediments. The unit can be divided further to separate a Pliocene to Pleistocene sequence of mainly diatom radiolarian clay (Subunit IA), which includes an interval of about 10 m of clayey diatom ooze; an intermediate upper Miocene to Pliocene sequence of diatom radiolarian clay having thin intervals of clayey nanofossil

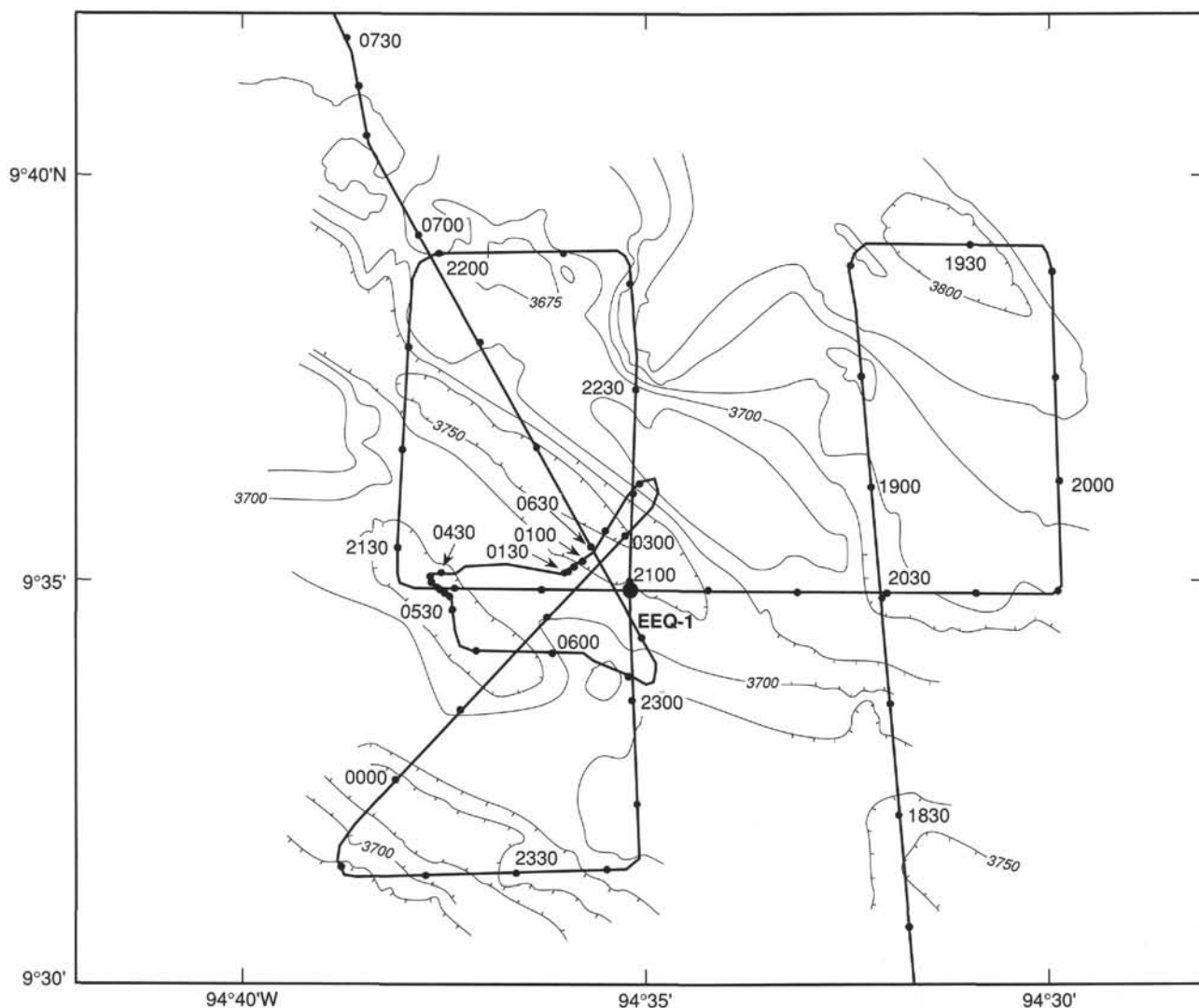


Figure 3. SeaBeam map hand-contoured from navigation-adjusted SeaBeam contour maps collected from the *Thomas Washington* during the Venture 1 cruise, September 1989. Proposed Site EEQ-1 is shown.

ooze (Subunit IB), and a lower sequence of upper Miocene clayey radiolarian ooze (Subunit IC).

Subunit IA

Intervals:

Hole 845A, Cores 138-845A-1H through -8H-3, 135 cm

Hole 845B, Cores 138-845B-1H through -7H-6, 110 cm

Hole 845C, Cores 138-845C-1H through -3H

Age: Pleistocene to Pliocene

Depth: 0–68.95 mbsf, Hole 845A; 0–68.7 mbsf, Hole 845B; 20–48.5 mbsf, Hole 845C

Subunit IA comprises 69 m of sediment composed of varying proportions of diatoms, radiolarians and clay that contains only minor amounts of carbonate. A few thin, carbonate-rich horizons are found in which foraminifers generally are more abundant than nannofossils. The lithologies described include radiolarian clay, diatom ooze, diatom clay, and diatom radiolarian clay. The top 10 m are clay-rich (60%–80%) and have similar proportions of diatoms and radiolarians. From about 10 to 20 mbsf, diatoms generally are the dominant siliceous microfossil, with

diatom ooze (up to 70% diatoms) occurring as frequent, olive gray horizons, and clayey radiolarian diatom ooze as the dominant lithology. Paler burrow fills commonly include more microfossil-rich concentrates; these incorporate the scattered foraminifers and nannofossils. Below this, the sediments are generally more clay-rich (50%–80%), with radiolarians generally the dominant siliceous microfossil (Fig. 6). The nonbiogenic fraction of the sediment (determined by X-ray diffraction analyses) is dominantly smectite, Na-rich anorthite, and quartz. Significant quantities of barite also are present. A 30-cm-thick horizon of a greenish-black, granular material was encountered in Section 138-845B-5H-4 at 27 cm. Several ash horizons can be seen, but their recognition was hindered by extensive bioturbation. An 8-cm-thick gray vitric ash can be seen in Sections 138-845A-5H-3, 111 cm (40.21 mbsf), -845B-4H-6, 70 cm (39.6 mbsf), and -845C-1H-1, 135 cm (40.35 mbsf). Immediately beneath this ash lies a set of laterally persistent *Zoophycos* burrows (Fig. 9, see “Trace Fossils” section, this chapter). Bioturbated ash horizons also occur near the base of the subunit, between 64 and 69 mbsf. Scattered dolomite nodules are present between 50 and 69 mbsf. Micritic carbonate also can be seen in quantities of up to 10% of the dominant lithology in the lowermost 10 m, with scattered, more micrite-rich pale pods or burrow fills.

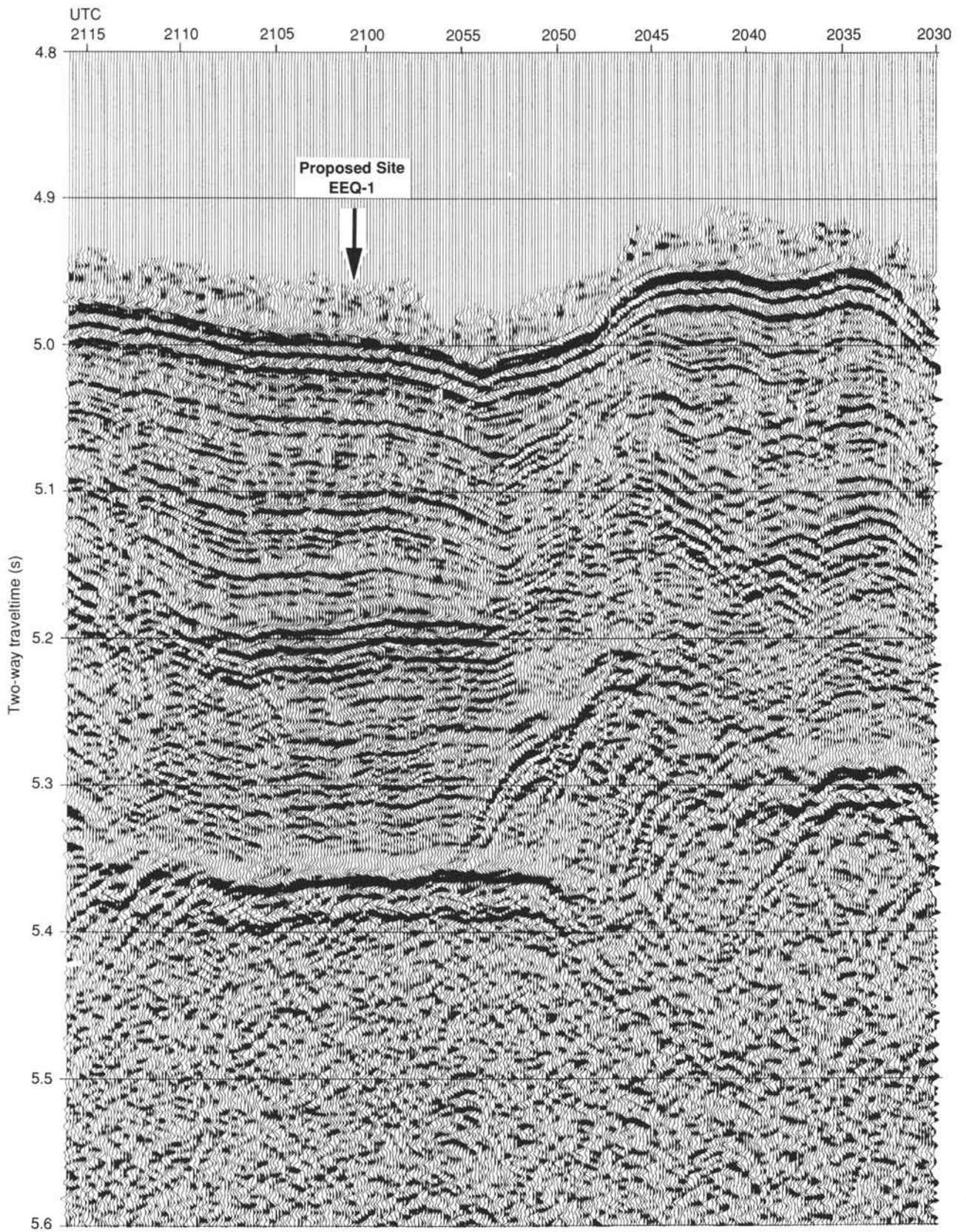


Figure 4. Seismic Line A, 80-in.³ water-gun record collected during the *Thomas Washington* cruise (Venture 1). Proposed Site EEQ-1 is shown.

Table 1. Summary of coring operations at Site 845.

Core no.	Date (May 1991)	Time (UTC)	Depth (mbsf)	Length cored (m)	Length recovered (m)	Recovery (%)
138A-845A1H	14	0915	0.0–7.6	7.6	7.62	100.0
2H	14	1000	7.6–17.1	9.5	9.61	101.0
3H	14	1050	17.1–26.6	9.5	9.89	104.0
4H	14	1140	26.6–36.1	9.5	9.89	104.0
5H	14	1235	36.1–45.6	9.5	9.99	105.0
6H	14	1325	45.6–55.1	9.5	10.04	105.7
7H	14	1425	55.1–64.6	9.5	9.81	103.0
8H	14	1515	64.6–74.1	9.5	9.95	105.0
9H	14	1605	74.1–83.6	9.5	9.97	105.0
10H	14	1720	83.6–93.1	9.5	10.01	105.3
11H	14	1815	93.1–102.6	9.5	10.11	106.4
12H	14	1905	102.6–112.1	9.5	9.76	103.0
13H	14	2000	112.1–121.6	9.5	10.03	105.6
14H	14	2055	121.6–131.1	9.5	10.07	106.0
15H	14	2150	131.1–140.6	9.5	10.03	105.6
16H	14	2305	140.6–150.1	9.5	10.02	105.5
17H	15	0000	150.1–159.6	9.5	9.85	103.0
18H	15	0100	159.6–169.1	9.5	10.09	106.2
19H	15	0155	169.1–178.6	9.5	10.06	105.9
20H	15	0255	178.6–188.1	9.5	10.13	106.6
21H	15	0355	188.1–197.6	9.5	10.03	105.6
22H	15	0505	197.6–207.1	9.5	9.99	105.0
23X	15	0610	207.1–216.8	9.7	9.50	97.9
24X	15	0715	216.8–226.5	9.7	1.45	14.9
25X	15	0805	226.5–236.1	9.6	9.59	99.9
26X	15	0905	236.1–245.8	9.7	9.42	97.1
27X	15	1005	245.8–255.0	9.2	9.73	106.0
28X	15	1100	255.0–264.6	9.6	9.56	99.6
29X	15	1155	264.6–274.2	9.6	9.75	101.0
30X	15	1245	274.2–283.9	9.7	9.67	99.7
31X	15	1420	283.9–291.6	9.7	7.01	91.0
Coring totals				291.6	292.63	100.4
138-845B-1H	16	1410	3.1–12.6	9.5	6.63	69.8
2H	16	1455	12.6–22.1	9.5	8.89	93.6
3H	16	1540	22.1–31.6	9.5	5.85	61.6
4H	16	1635	31.6–41.1	9.5	9.59	101.0
5H	16	1730	41.1–50.6	9.5	7.30	76.8
6H	16	1825	50.6–60.1	9.5	9.37	98.6
7H	16	1925	60.1–69.6	9.5	9.75	102.0
8H	16	2020	69.6–79.1	9.5	9.97	105.0
9H	16	2120	79.1–88.6	9.5	9.96	105.0
10H	16	2230	88.6–98.1	9.5	9.97	105.0
11H	16	2325	98.1–107.6	9.5	9.92	104.0
12H	17	0025	107.6–117.1	9.5	10.02	105.5
13H	17	0135	117.1–126.6	9.5	9.94	104.0
14H	17	0235	126.6–136.1	9.5	10.00	105.2
15H	17	0330	136.1–145.6	9.5	8.46	89.0
16H	17	0440	145.6–155.1	9.5	9.95	105.0
17H	17	0540	155.1–164.6	9.5	10.07	106.0
18H	17	0655	164.6–174.1	9.5	9.93	104.0
19H	17	0750	174.1–183.6	9.5	9.63	101.0
20H	17	0910	183.6–193.1	9.5	9.95	105.0
21H	17	1010	193.1–202.6	9.5	10.08	106.1
Coring totals				199.5	195.23	97.9
138-845C-1H	17	1305	20.0–29.5	9.5	9.84	103.0
2H	17	1400	29.5–39.0	9.5	10.02	105.5
3H	17	1455	39.0–48.5	9.5	8.63	90.8
Coring totals				28.5	28.49	100.0

The radiolarian clay at the top of the subunit is greenish-gray (5GY 5/2) with paler (10Y 5/2) and darker (10Y 3/1) mottling. At about 10 mbsf, a change is seen toward a darker, greenish-gray (5GY 5/2) with olive gray (5Y 5/2), more diatom-rich sediment. Extensive bioturbation causes color mottling of the greenish-gray (clay-rich) and olive-gray (diatom-rich) sediments. Throughout the upper 30- to 35-m, high-amplitude color variation (Fig. 8) results from burrowing and diagenetic dark bluish-black mottling. Dark bluish-black banding and lamination also are present. Most burrows contain paler, greenish-

gray (5G 6/1) material that generally is compositionally indistinguishable from the surrounding sediment; however, some burrows contain concentrates of foraminifers and nannofossils that probably represent the bioturbated remains of original layers. Beneath 35 mbsf, less pronounced variations in color can be seen (see "Color Reflectance Spectroscopy" section, this chapter), while dark greenish-gray (5G4/1) is the dominant color, and from 50 mbsf to the base of Subunit IA (68 mbsf), the sediment is a uniform gray (5Y 5/1), with little bioturbation or mottling visible.

Table 2. Summary of logging operations at Hole 845A.

Day (May 1991)	Time (L)	Hours	Depth (mbsf) (base of string)	Remarks
15	0820	0		Last core on deck.
15	1100	2.7		Start rig up.
15	1245	4.4		Geophys. tool rigged up (NGT/SDT/HLDT/DIT/TLT); RIH.
15	1407	5.8	110.0	Start downlog, no heave compensator.
15	1435	6.3	292.0	Stopped down-going log; at TD; heave compensator on.
15	1443	6.4	292.0	At TD, start main log up (NGT/SDT/HLDT/DIT/TLT).
15	1522	7.0	100.0	Stop up-going log, go back for repeat section.
15	1528	7.1	170.4	Start repeat section.
15	1543	7.4	99.1	End repeat section; close calipers and POOH.
15	1700	8.7		Geophys. tool string at wellhead.
15	1830	10.2		RIH w/Geochem String (NGT/ACT/GST/TLT).
15	1957	11.6	292.9	At TD; start calibrating and moving up at 300 ft/hr.
15	2118	13.0	137.5	Had trouble calibrating; tool now calibrated; going down to TD.
15	2125	13.1	291.6	Start main log w/geochem. string; no heave compensator.
15	2305	14.7	0	Stop main log; POOH.
16	0020	16.0		Geochem. string at rig floor, post-calibration.
16	0155	17.6		RIH w/FMS string (NGT/GPIT/FMS/TLT).
16	0319	19.0	291.3	At TD, start FMS repeat log; heave compensator on.
16	0342	19.4	155.1	Stop repeat log; drop back to TD for main log.
16	0352	19.5	291.5	Start main FMS log at TD.
16	0418	20.0	69.8	Stop main FMS log.
16	0427	20.1		POOH FMS string.
16	0630	22.2		Rigged down from logging.

The lower boundary of Subunit IA was taken at the base of a distinct pale burrowed horizon in Sections 138-845A-8H-3, 135 cm, and -845B-7H-6, 110 cm.

Subunit IB

Intervals:

Hole 845A, Sections 138-845A-8H-3, 135 cm, through -13H-2, 115 cm
 Hole 845B, Sections 138-845B-7H-6, 110 cm, through -12H-5, 80 cm
 Age: Pliocene to late Miocene
 Depth: 68.95–114.75 mbsf, Hole 845A; 68.7–114.4 mbsf, Hole 845B

The sediments of lithologic Subunit IB comprise mixtures of radiolarians, diatoms, and clays, with variable carbonate (mainly nannofossil) content that increases with depth. Lithologies described include radiolarian diatom clay, diatom radiolarian clay, and radiolarian clay, with subordinate amounts of clayey nannofossil radiolarian ooze and clayey radiolarian nannofossil ooze and, rarely, nannofossil clay. From 69 to about 80 mbsf, the sediment is mainly a radiolarian diatom clay with 20% to 25% diatoms. Below this, to the base of the subunit at 114 mbsf, diatoms are subordinate to radiolarians and rarely make up more than 10% of the lithology (Fig. 6). From 80 to 100 mbsf, the sediment is mainly a radiolarian clay with a few paler, bioturbated, nannofossil-rich horizons. From 103 to 114 mbsf, clayey radiolarian nannofossil ooze is the dominant lithology (30%–70% nannofossils), with meter-scale alternation of paler (more nannofossil-rich) with darker horizons. As in Subunit IA, the clay-rich units are dominated by smectite, plagioclase, and quartz, along with significant amounts of barite. Significant quantities of pyrite also are seen (up to about 7%), particularly in nannofossil-rich horizons. Throughout this subunit, paler thin bands and solid burrow fills are commonly more microfossil-rich (particularly in nannofossils and/or diatoms) than the surrounding sediments. Pale olive, dolomite nodules, between 2 and 5 cm in diameter, are seen throughout the subunit and are particularly common from 80 to 105 mbsf (Fig. 10).

The upper part of the subunit is a dark greenish-gray (5GY 4/1) to gray (5Y 5/1) color (with the more clay-rich horizons being darker), with some paler (5Y 5/2), more nannofossil-rich layers. From 100 to 114 mbsf, the sediments range from a dark gray, clayey radiolarian nannofossil ooze (5Y 4/1) to a paler, greenish-gray nannofossil ooze. Burrows and thin bands of more nannofossil-rich sediments are

typically a paler, olive gray (5Y 5/2). Dark bluish bands and lamination are present, though are not abundant. This dark bluish color also is present in rings or halos around some burrows. A distinct, dark bluish, laminated band in Sections 138-845A-8H-6 at 25 to 47 cm and -8H-1 at 53 to 68 cm correlates well among holes (Fig. 11).

The base of Subunit IB is marked by the first occurrence of paler burrowed horizons and a change downcore to a uniform, very dark gray (5GY 4/1).

Subunit IC

Intervals:

Hole 845A, Sections 138-845A-13H-2, 115 cm, through -15H-4, 103 cm
 Hole 845B, Sections 138-845A-12H-5, 80 cm, through -14H-7, 61 cm
 Age: late Miocene
 Depth: 114.75–135.63 mbsf, Hole 845A; 114.4–136.23 mbsf, Hole 845B

Subunit IC comprises radiolarian-rich sediments having varying proportions of clay and diatoms. From 112 to 125 mbsf, the sediment is mainly a clayey radiolarian ooze (radiolarians, 50%–60%; diatoms, 2%–10%), with minor, more clay-rich horizons near the top. Between 125 and 135 mbsf, the sediment is mainly a diatom radiolarian clay (clay, 40%–60%). From about 122 mbsf to the base of the subunit, frequent burrow fills and scattered bioturbated, 1- to 2-cm-thick bands of a pure, pale diatom ooze can be seen (Fig. 12). The floras comprise well-preserved, nearly monospecific concentrations of *Thalassiothrix longissima*. Abundances of these burrows and bands of diatom ooze increase down toward the base of Unit I at 136 mbsf. A single dolomite nodule is seen toward the base of the unit at Section 138-845A-14H-5, 63–73 cm, and significant (>5%) quantities of dolomite occur in a diatom ooze horizon 35 cm from the base.

Most of the subunit is a uniform dark greenish-gray (5GY 4/1) with minimal variation in reflectance (Fig. 8). A gradational change is seen over 50 cm in Sections 138-845A-14H-6, 90 cm, (130 mbsf) and -845B-14H-2, 0 cm (128.1 mbsf) to a yellowish to dark yellowish-brown (10YR 5/4 to 10YR 4/4). This interval is about 1.5 m thick, and below it, color grades back over 50 cm to dusky yellow-green (5GY 5/2) that is mottled with darker grayish-olive green (5GY 3/2) patches and thin bands. A further, more abrupt color change to yellowish brown is seen 30 cm above the base of the subunit at Sections 138-845A-15H-4, 82 cm (136.4 mbsf) and -845B-14H-7,

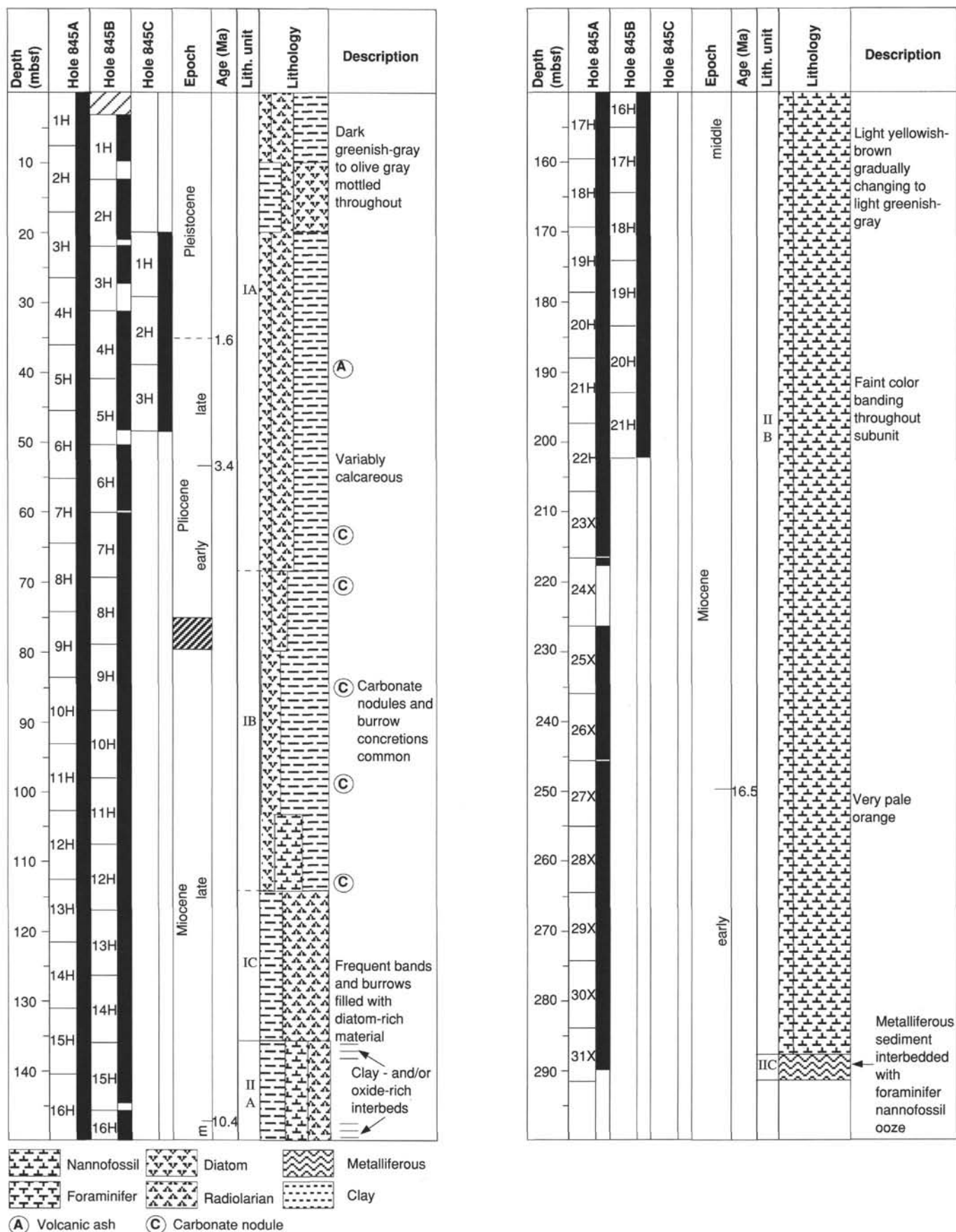


Figure 5. Lithostratigraphic summary of Site 845.

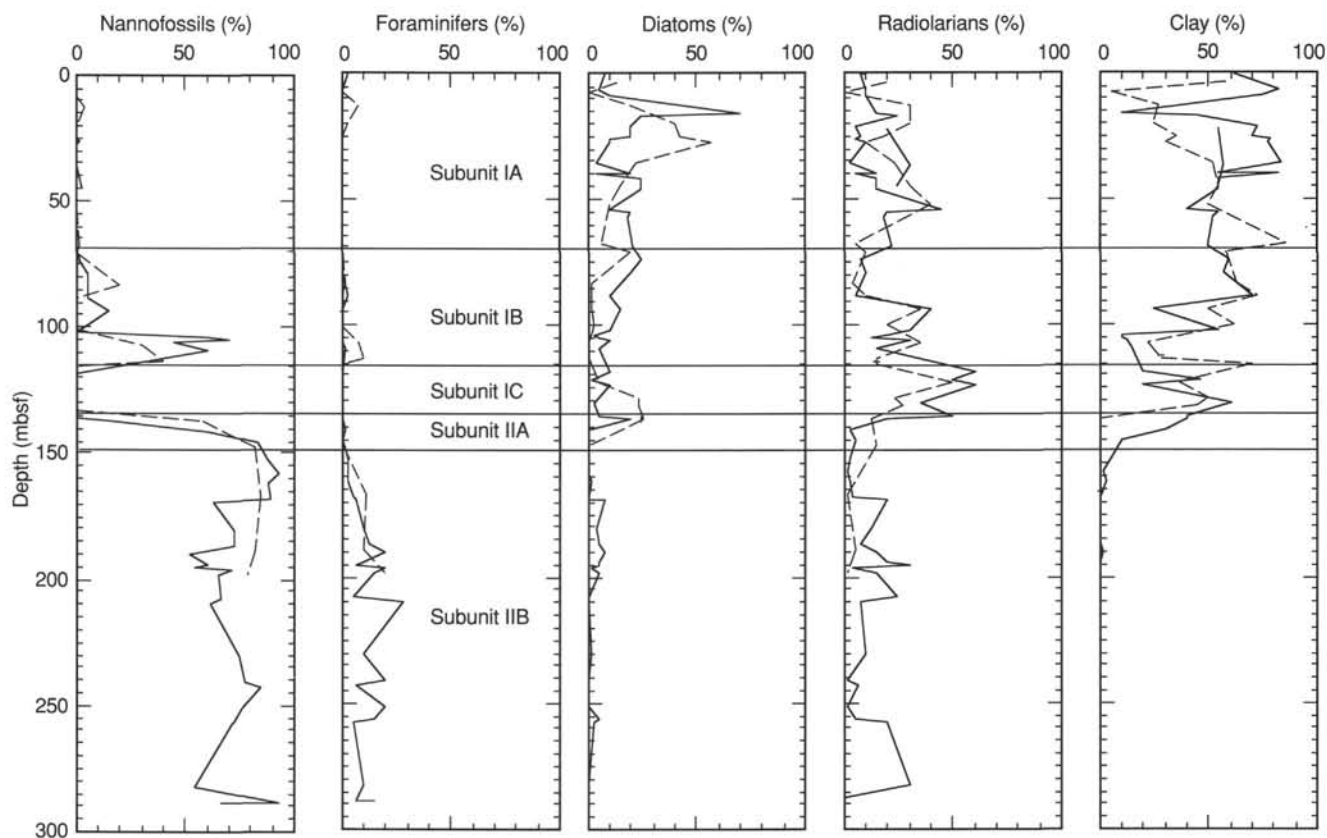


Figure 6. Summary of major-component smear slide data from dominant lithologies at Site 845. Solid line = Hole 845A; dashed line = Hole 845B. Lithologic units shown for reference.

35 cm. Neither of these color changes is associated with any compositional change identified from smear slide analysis.

The base of Subunit IC and Unit I is marked by the top of a bed of very dark brown, oxide-rich, radiolarian clay at Sections 138-845A-15H-4, 103 cm, and -845B-14H-7, 61 cm.

Unit II

Intervals:

Hole 845A, Sections 138-845A-15H-4, 103 cm, through 138-845A-31X-CC

Hole 845B, Sections 138-845B-14H-7, 61 cm, through -21H

Age: middle Miocene to late Miocene

Depth: 135.63–291.4 mbsf, Hole 845A; 136.23–202.6 mbsf, Hole 845B

Unit II comprises mainly nannofossil ooze, but has a distinctive transitional siliceous/carbonate interval that includes clay- and oxide-rich horizons at the top (Subunit IIA) and a thin sequence of metalliferous sediments (Subunit IIC) immediately above basaltic basement.

Subunit IIA

Intervals:

Hole 845A, Sections 138-845A-15H-4, 103 cm, through -17H-1, 0 cm

Hole 845B, Sections 138-845B-14H-7, 61 cm, through -16H-3, 8 cm

Age: middle Miocene to late Miocene

Depth: 135.63–150.1 mbsf, Hole 845A; 136.23–149.4 mbsf, Hole 845B

The sediments of Subunit IIA represent a 14-m-thick transitional sequence between the siliceous microfossil- and clay-rich sediments

of Unit I and the nannofossil oozes of Subunit IIB. Nannofossil content increases, and radiolarian content decreases downward. The subunit is further distinguished by distinctive color variations and the presence throughout of a series of beds rich in micronodules of Mn/Fe oxides. In the top part, an alternation is seen between relatively thin (<15 cm) beds of very dark brown (10YR 2/2), oxide-rich (10%–15%) clay with thicker beds of dark yellowish-brown diatom radiolarian clay containing nannofossils and yellowish-brown to very pale grayish-orange (10YR 7/2) radiolarian nannofossil ooze (Fig. 13). The nannofossil content increases downward, and the proportion of clay and siliceous microfossils decreases. The oxide-rich beds are grouped in the upper and lower 5 m, with an intervening 4 m of radiolarian nannofossil ooze. Pale burrow fills and thin bands of diatom ooze occur from about 142 mbsf and increase in frequency and thickness toward the top (Fig. 14) and continuing into Subunit IC above. The contents of these diatom oozes closely resemble those found at the base of Subunit IC. Near the base of the subunit, very hard, pale olive rhodochrosite nodules can be seen at Sample 138-845B-16H-1, 50–52 cm, and in the top of Subunit IIB at Section 138-845A-17H-2 at 52 cm.

The base of the subunit is the base of a thin, very dark brown (10YR 2/2) layer of oxide-rich nannofossil ooze in Core 138-845B-16H-3, 8 cm (150 mbsf).

Subunit IIA has a distinctive signature in the downhole geochemical borehole logs (Fig. 15). The oxide-rich beds are seen as peaks in the natural gamma-ray trace. Clay-rich oxide beds also are seen as peaks in the neutron activation aluminium log; however, the oxide-rich nannofossil ooze at the base is distinguished as a peak in the gamma-ray log, but not in the aluminium record.

Subunit IIB

Intervals:

Hole 845A, Sections 138-845-17H-1, 0 cm, through -31X-3, 125 cm

Hole 845B, Sections 138-845B-16H-3, 8 cm, through -21H

Age: early to middle Miocene

Depth: 150.1–288.2 mbsf, Hole 845A; 149.4–202.6 mbsf, Hole 845B

Subunit IIB comprises 135 m of foraminifer nannofossil ooze with a variable radiolarian content. Little systematic variation seems to occur down the core in the calcareous fraction, with abundances of foraminifers generally between 10% and 20%. The radiolarian content is more variable and ranges from 0% to 30%. The subunit is characterized by meter-scale alternation of the dominant lithology of foraminifer nannofossil ooze with thinner (10–30 cm), slightly darker beds of radiolarian nannofossil ooze that may contain trace quantities of pyrite (Fig. 16). This cyclicity is well demonstrated in the continuous GRAPE, susceptibility, and color records. Other very pale brownish bands result from a concentration of diatomaceous burrow fills. A few carbonate nodules occur between 150 and 153 mbsf. Greater amounts of iron oxides are seen as clusters of dark grains about 0.5 mm in diameter down the core from about 255 mbsf. In the basal few meters of the subunit, the nannofossil ooze has primary laminations, probably the result of redeposition (Fig. 17).

A color transition is seen over 4 m at the top of the subunit from a light yellowish-brown (10YR 6/4) radiolarian nannofossil ooze downward to a light gray (10YR 7/2) foraminifer nannofossil ooze. To about 165 mbsf, color changes from a pale yellowish-gray to gray (10 YR 6/2 to 2.5Y 7/2) to a uniform light greenish-gray (5GY 7/1 to 5G 7/1) down the core. The slightly darker beds of radiolarian nannofossil ooze are greenish-gray (5BG 6/1). A very sharp color change is seen at 247.5 mbsf from light greenish gray to very pale orange (10YR 8/2) with mottling and bands of grayish orange (10YR 7/4). From this level to the base of the subunit, the darker radiolarian nannofossil ooze beds are grayish-orange (10YR 7/4).

A distinct boundary was recorded in the downhole geophysical borehole logs at about 210 mbsf by a sharp increase in density and sonic velocity. An increase in GRAPE density is less obvious. This boundary probably was caused by lithification and does not appear to relate directly to any change in sediment composition. The only apparent change in lithology evident from smear slide analyses is a slight reduction in the proportion of diatoms within the sediment (Fig. 6).

The base of Subunit IIB was taken at the top of the first bed of red metalliferous sediment at Section 138-845A-31X-3, 125 cm (288 mbsf).

Subunit IIC

Interval:

Hole 845A, Sections 138-845A-31X-3, 125 cm, through -31X-CC, 25 cm

Age: early Miocene

Depth: 288.2–291.4 mbsf, Hole 845A

Subunit IIC is a thin, 2.5-m interval of metalliferous sediment with an interbed of nannofossil ooze overlying basaltic basement. Colors range from green to red (5YR 5/8 and 10 YR 3/4 to 5Y 4/2). Two graded microconglomerate layers can be seen between Section 138-845A-31X-3, 125–133 cm (Fig. 17). Below these lies 1 m of very firm, fine-grained, bright orange (10R 4/8) sediment that contains a few soft, very dark red (5R 2/6), angular lithic clasts that have been altered to grunerite (a disordered lizardite serpentine/disordered talc–mixed layer clay) and also contains some calcite. The sediment is cut by a few thin (<2 mm) veins of calcite (Section 138-845A-31X-4, 12–20 cm, Fig. 18). Between Sections 138-845A-31X-4, 105 cm, and -31X-5, 20 cm, the sediment contains a mixture of variously colored, white, purple, and olive gray, 2- to 8-cm-thick clasts of basalt (Fig. 19) and softer material composed of calcite, kerolite (disordered

talc), lizardite, hematite, and grunerite. Some clasts exhibit zoning. The matrix sediment shows only plagioclase (sodic intermediate anorthite), calcite, and quartz peaks in X-ray diffraction scans. No Fe or Mn oxide peaks can be seen in the matrix sediment, although the Fe/Al ratio is greater than 7.

The sediment in the core-catcher sample consists of 22 cm of soft, orange (10R 5/8) calcite- and plagioclase-rich material above basalt basement. This sediment exhibits little structure, and the two hours we took to drill the basalt may have disturbed and homogenized the material recovered in the core catcher.

Trace Fossils

Trace fossils are abundant in the top 35 m of Subunit IA. Solid burrows and *Planolites* are the most common. Ring burrows with dark bluish haloes also occur, but one striking feature is multiple stacks of *Zoophycos* burrows. A remarkable correspondence was observed between almost identical stacks of *Zoophycos* burrows in Sections 138-845A-5H-3, 120–145 cm (40.5 mbsf) and -845B-4H-6, 77–102 cm (40 mbsf; Fig. 9). With horizontal offset of at least 10 m between Holes 845A and 845B, this correlation implies considerable lateral persistence of burrowing. Although mainly sub-horizontal, scattered high-angle *Zoophycos*(?) burrows can be seen (Fig. 20). Little bioturbation is visible below 50 mbsf, other than prominent calcified burrows in Sections 138-845B-6H-1.

In Subunit IB, trace fossils are common to abundant, with solid burrows and *Planolites* most frequently observed. *Zoophycos* is relatively rare, except between 100 and 114 mbsf, where *Skolithos* also is seen, often amid complex cross-cutting burrow networks (Fig. 21). *Chondrites* was observed only in a pale diatom nannofossil clay from 74 to 77 mbsf. Trace fossils were observed less frequently in clay-rich intervals (e.g., 85–90 mbsf).

We observed only a faint irregular mottling in most of Subunit IC. No discernible trace fossils were observed, other than irregular solid burrows with diatom-rich fill that occur with increasing frequency down the core from 122 mbsf. Some *Planolites* burrows were seen below 130 mbsf, and isolated *Skolithos* burrows are present in Section 138-845B-14H-6 at 85 cm.

Moderate to strong bioturbation throughout Subunit IIA was made more obvious by the strong variations in bedding color. Solid burrows and *Planolites* are most common, with scattered *Zoophycos* and *Skolithos* and *Chondrites* occurring within *Planolites* burrows in the middle radiolarian nannofossil ooze section (140–145 mbsf; Fig. 22).

Bioturbation is light to moderate in Subunit IIB, with solid burrows and *Planolites* most common (Figs. 23) and *Chondrites* commonly observed. Rind burrows and burrows with halos are also locally developed. *Skolithos* is less common, while very rare *Zoophycos* was recorded between 150 and 175 mbsf. No trace fossils were observed in Subunit IIC.

Ichnofacies Summary

Two distinct ichnofacies were identified. Trace fossils typical of Subunits IA and IB are solid burrows, rind burrows, *Planolites*, and *Zoophycos*. *Zoophycos* is particularly abundant in Subunit IA. *Chondrites* is very rare and was observed only in the carbonate-rich sections of Subunit IB. Carbonate-rich lithologies of Unit II are characterized by the presence of common *Chondrites* that cut *Skolithos*, solid burrows, rind burrows, and *Planolites*.

Color Reflectance Spectroscopy

Color reflectance data at Site 845 were distinctive in each lithologic unit (Fig. 8). In Unit I, the sediments were dark, generally greenish-gray to dark greenish-gray, and had low reflectance that

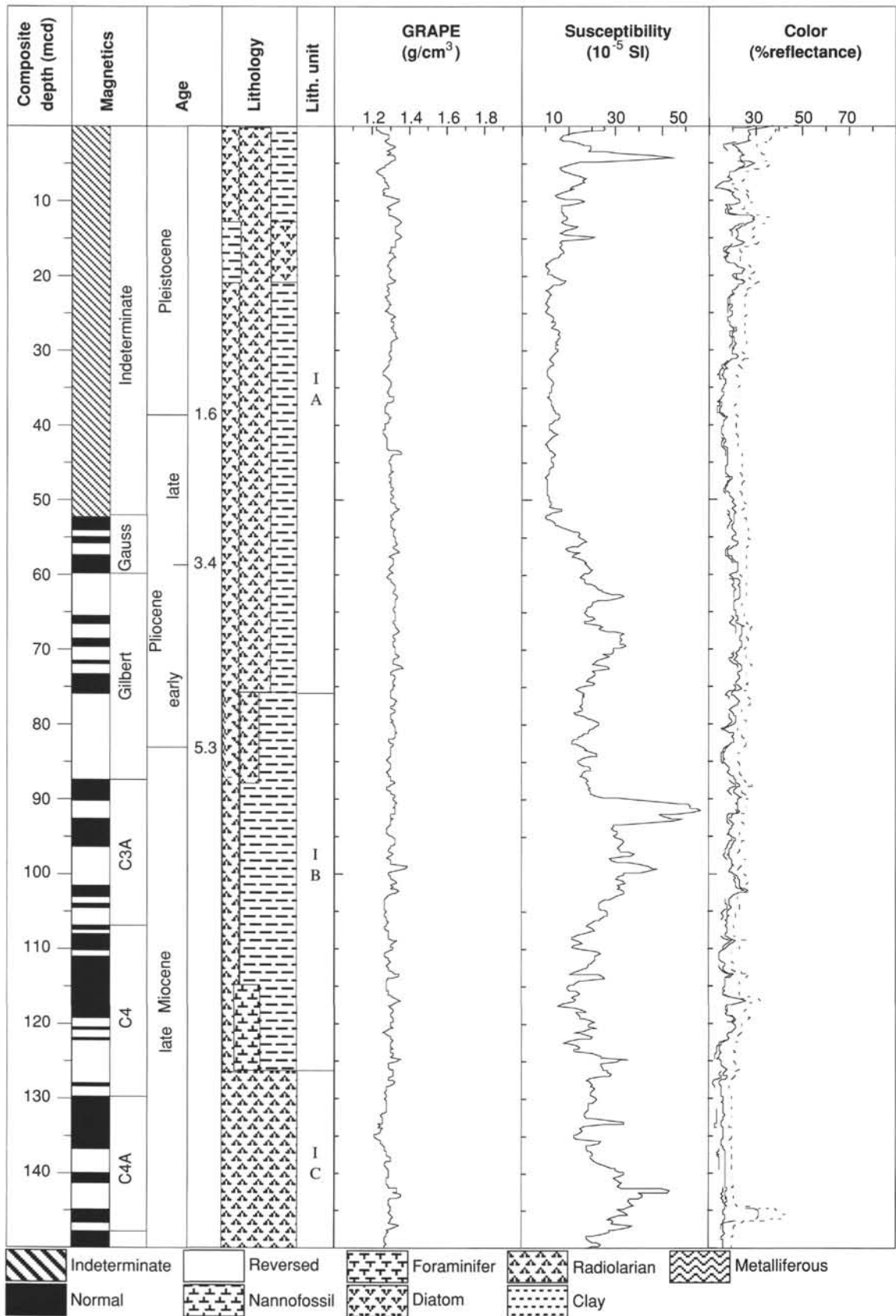


Figure 7. Composite summary of magnetics, age, graphic lithology, GRAPE, magnetic susceptibilities, and color reflectance for Site 845. The composite data consist of sections spliced together from multiple holes drilled at the site. These data are shown plotted vs. meters composite depth (mcd), the new depth scale used for creating composite sections. The GRAPE, susceptibility, and color data have been smoothed using a 20-point Gaussian filter.

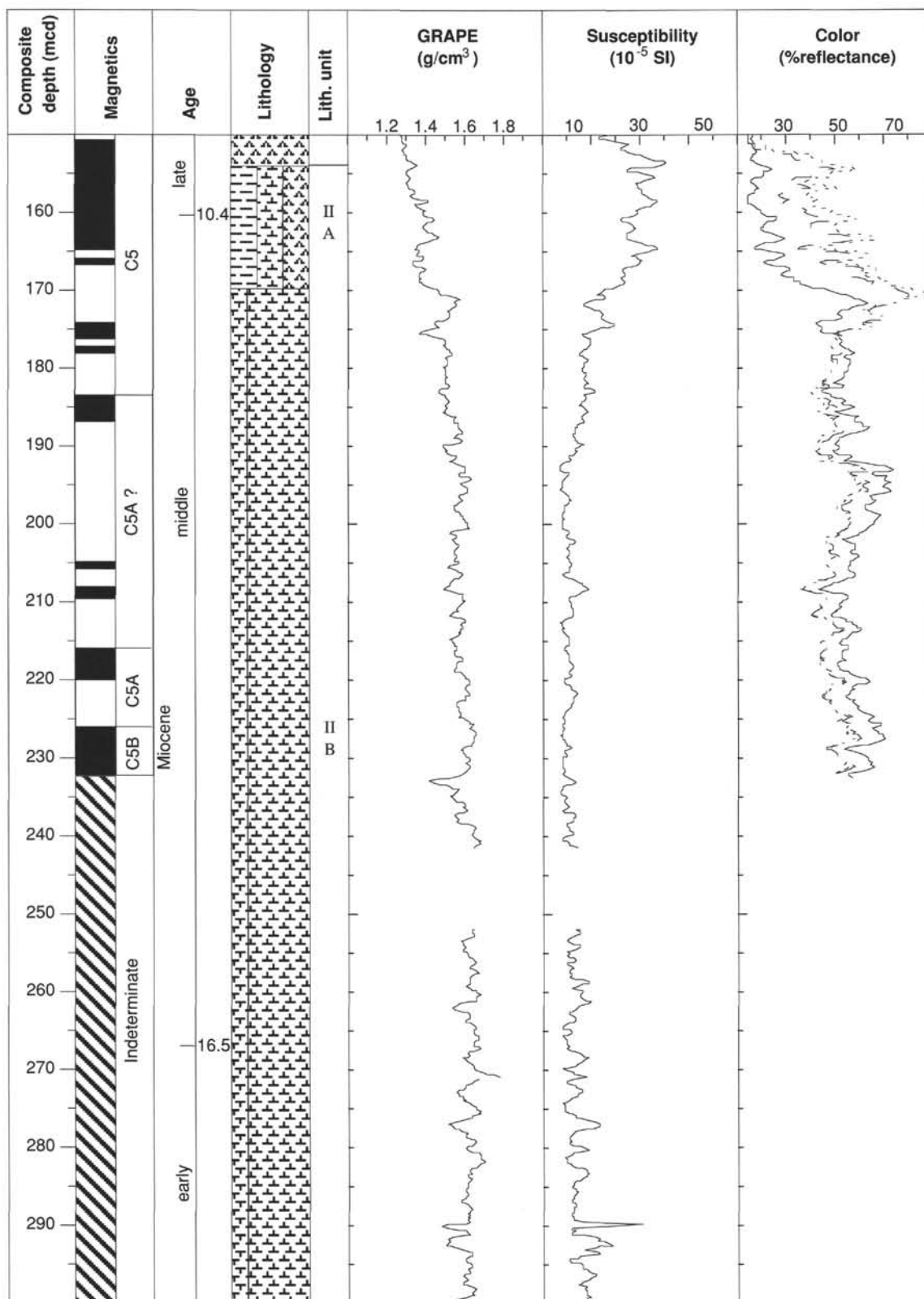


Figure 7 (continued).

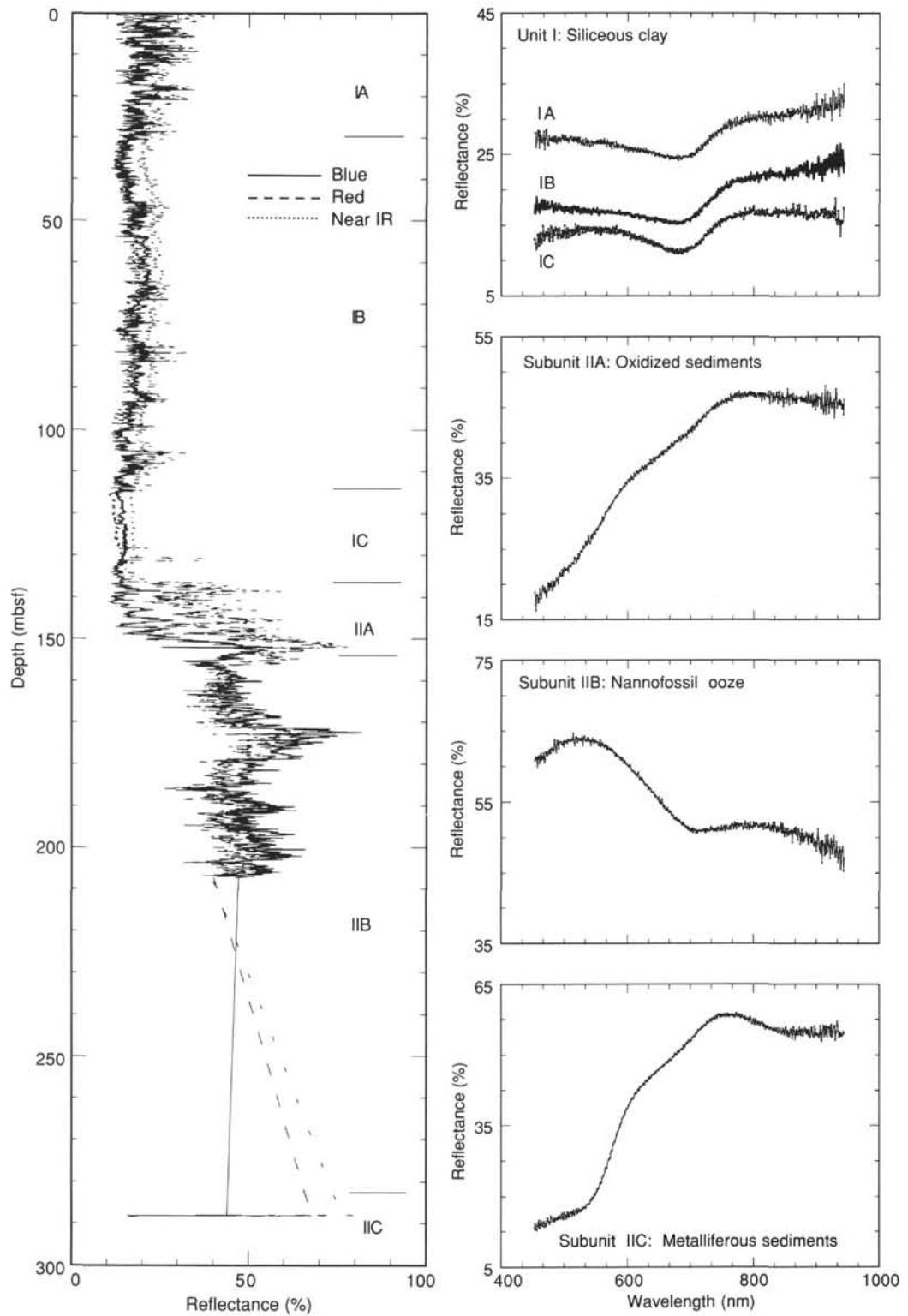


Figure 8. Summary of variations in color reflectance at Site 845, showing spectra characteristic of the major lithologic divisions.

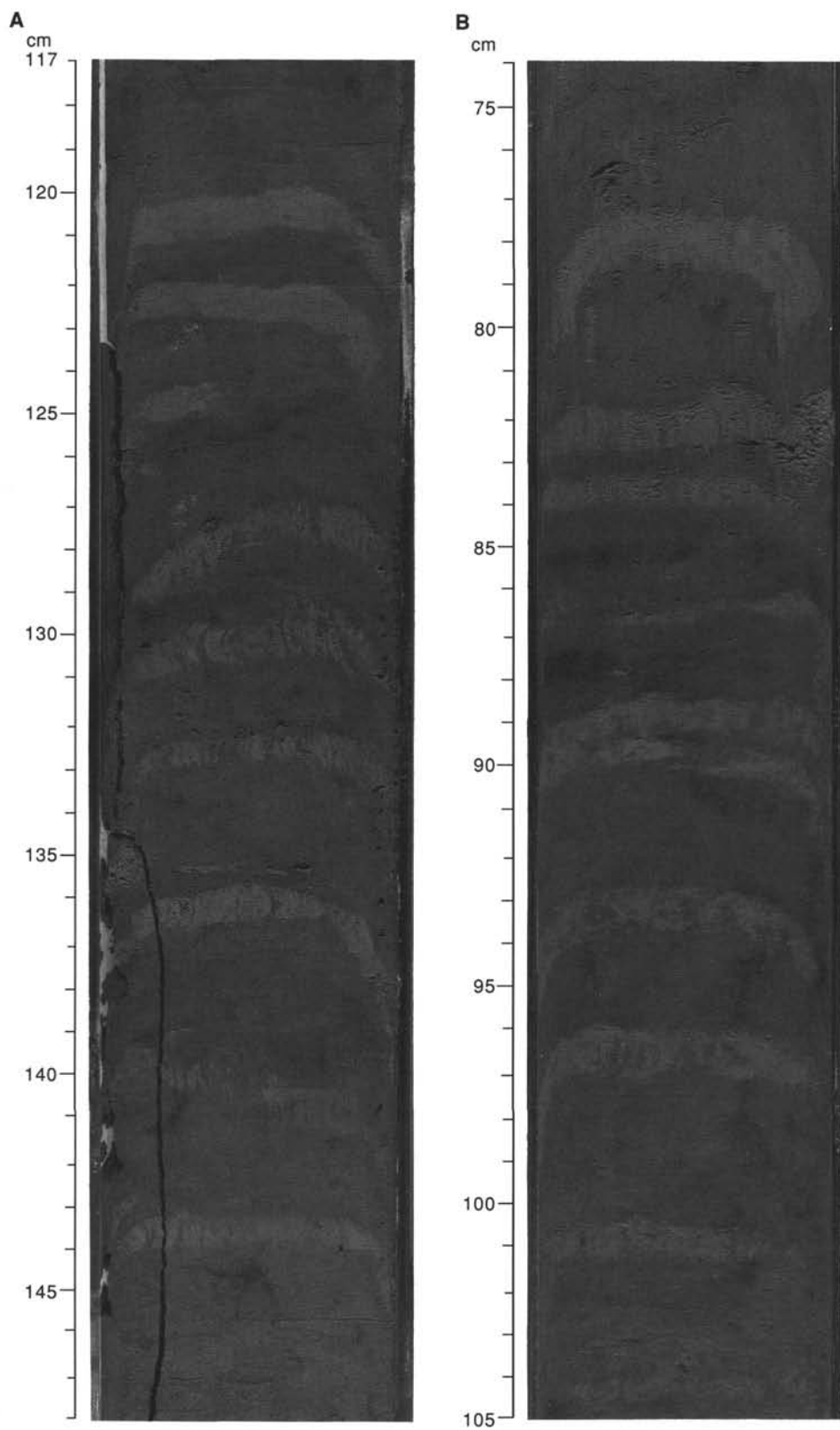


Figure 9. A. *Zoophycos* burrows in Subunit IA (interval 138-845A-5H-3 at 117–148 cm). These correlate with an almost identical stack of burrows at the same horizon in Hole 845B in the interval at 138-845B-4H-6, 74–105 cm (B).

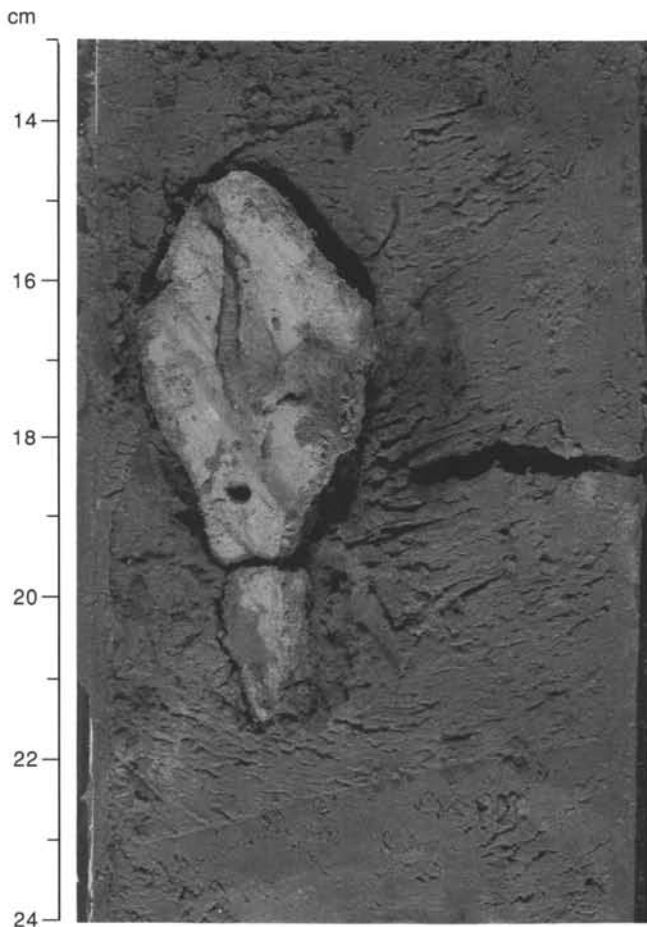


Figure 10. Dolomite nodule in sediments of Subunit IB at Section 138-845B-8H-1, 13–24 cm.

ranged from 10% to 40% in all bands. Although the average reflectance varied within this range, all spectra in the three subunits of Unit I had similar shapes, with highest reflectance in the near-infrared (700 nm), lower reflectance in the visible (<700), and a minimum reflectance in the red (650–700 nm) bands. This spectral shape was seen consistently in the siliceous clay sediments at this site.

Unit II contains several different spectral signatures. Subunit IIA is reddish-brown, oxidized sediment and has a spectrum high in the near-infrared and red bands (650 nm), with reflectance of 35% to 45% in these bands, and low reflectance (<20%) on the blue end of the spectrum (<500 nm). This oxidized interval spanned both siliceous and carbonate lithologies and demonstrated strong variability, with reflectance values that ranged from 10% to 90%.

Subunit IIB, composed of nanofossil ooze, was identified by a different reflectance spectral pattern, high in the visible bands, especially in the range of 500–650 nm (green to orange), and low in the infrared band. A local minimum sometimes occurred in the red band (650–700 nm). Average reflectance values were generally high, but variable in this subunit and ranged from 40% to 90%.

The portion of Subunit IIB recovered with the XCB was not measured for color reflectance at Site 845. An exception to this was the basal metalliferous sediments, which were analyzed because of their unique character. These dark red sediments yielded a reflectance spectrum similar to, but more extreme than, the oxidized sediments of Subunit IC. Reflectance was extremely low (10%–15%) in the blue

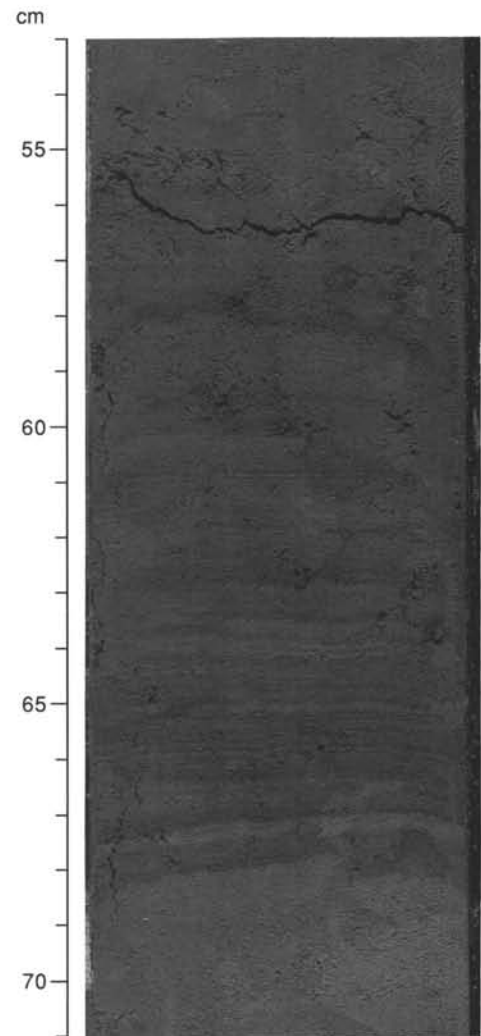


Figure 11. A distinctive early diagenetic laminated band that is laterally persistent among holes (Section 138-845B-8H-1 at 53–71 cm).

and green bands (wavelengths <550 nm), but rose rapidly to 40% to 45% in the red (650–700 nm) band. Reflectance was even higher (55%–60%) in the near-infrared band, with a maximum at 700 to 800 nm.

Color Banding and Lamination

The color banding observed was caused mainly by compositional variation, other than the red/green banding in Subunits IC and IIA (described above) and dark bluish-black, early diagenetic banding common in Subunits IA and IB. We did not observe compositional lamination.

Early Diagenetic Lamination and Banding

Dark bluish-black banding and lamination are common in Subunits IA and IB. Burrows are cut by common dark purplish lamination (Fig. 24), indicating that this type of lamination must have formed beneath the zone of bioturbation. Although this type of banding clearly is not depositional, the lateral persistence of bands of lamination that can be correlated among holes (e.g., a distinct, dark bluish laminated band in Sections 138-845B-8H-6 at 25–47 cm, and -8H-1 at 53–68 cm; Fig. 11) suggests original compositional control on its development.

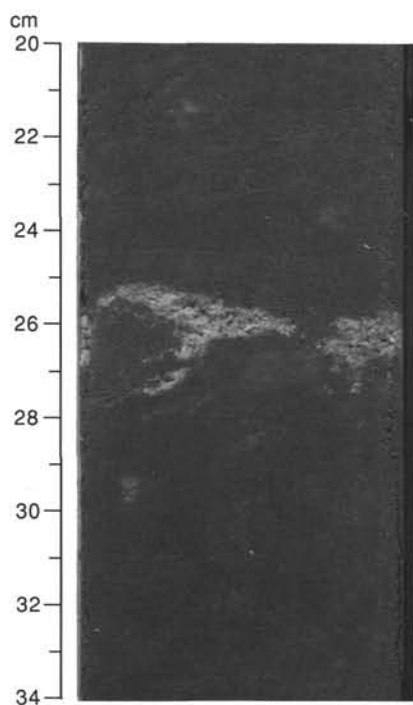


Figure 12. Bioturbated band of pale diatom ooze that contains strongly monospecific floras of *T. longissima* (Section 138-845B-14H-7 at 20–34 cm).

Compositional Banding

Compositional banding can be seen in Subunits IIA and IIB. In Subunit IIA, this banding results from an alternation of very dark brown mainly clay and oxide-rich beds with intervening beds of yellowish-brown radiolarian clay and pale yellow nannofossil ooze. This alternation is regular over the top and bottom 5 m of Subunit IIA, but has been disrupted by bioturbation.

The nannofossil ooze of Subunit IIB is characterized by a regular alternation of the dominant lithology of foraminifer nannofossil ooze with thinner (10–30 cm) darker beds of radiolarian nannofossil ooze that contain trace quantities of pyrite (Figs. 16 and 23). This alternation is visible throughout the nannofossil ooze and was also recorded in the color reflectance, GRAPE, and magnetic susceptibility data. Given our initial age models, the alternation appears to have a periodicity of tens of thousands of years.

Diagenetic Features

Mineralogical evidence of diagenesis is abundant in the sediments of Site 845. Pyrite is common in the upper 130 m (Subunits IA and IB) and reaches abundances of about 3%. It does not occur in Subunit IIA and was observed to be rare in the upper part of Subunit IIB within the darker radiolarian nannofossil ooze beds. Pyrite occurs in a wide variety of sizes, from microframboids as little as 3 μm in diameter, commonly seen to fill individual diatom aureoli, to larger polyframboids up to 0.5 mm wide. Pale olive carbonate (mainly dolomitic) nodules from 2 to 5 cm wide are seen toward the base of Subunit IA and are common in Subunit IB. This combination of pyrite and dolomitic concretions suggests diagenesis within an anoxic sulphidic environment.

Structural Features

The only structural features observed at Site 845, other than the veins within basalt, were a series of four faults, localized between 138

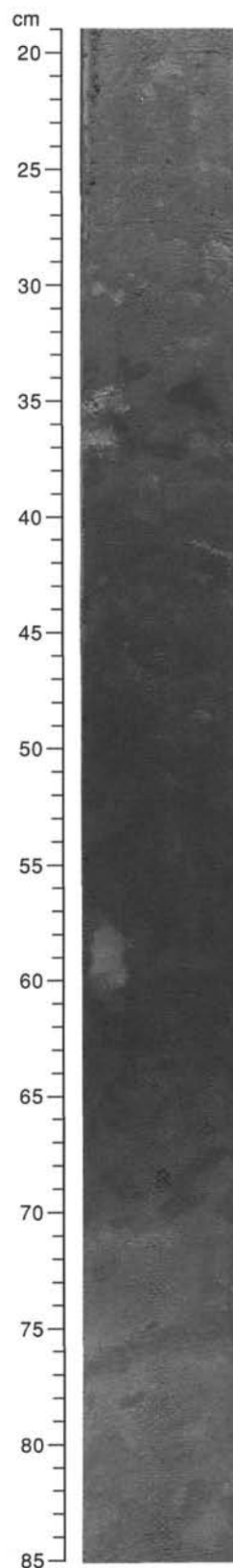


Figure 13. Darker bed of oxide-rich, carbonate-free radiolarian clay between paler beds of radiolarian diatom nannofossil ooze (Section 138-845B-15H-1 at 19–85 cm).

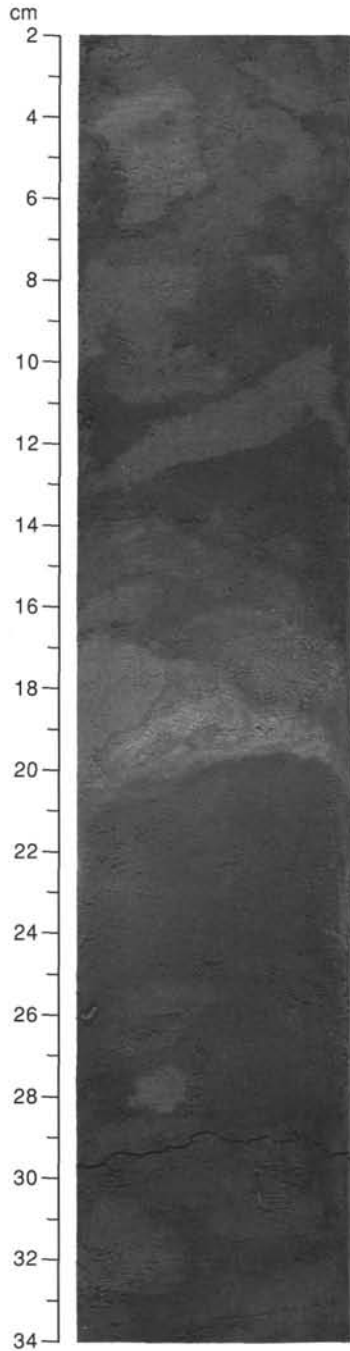


Figure 14. Very pale, bioturbated band of diatom ooze near the top of Subunit IIA (Section 138-845B-15H-3 at 2–34 cm).

and 141 mbsf, within Subunit IIA (Fig. 25). The orientation of these faults was obtained palaeomagnetically; it indicates that they trend about 10° west of north, with consistent downthrow to the east, which suggests relative downward motion to the east of the site. Displacements were small (about 3–5 cm), and most fault planes cut the edges of the core. The formation of faults at this horizon may have been promoted by the ductility contrast of the oxide-rich clays with the interbedded biogenic oozes.

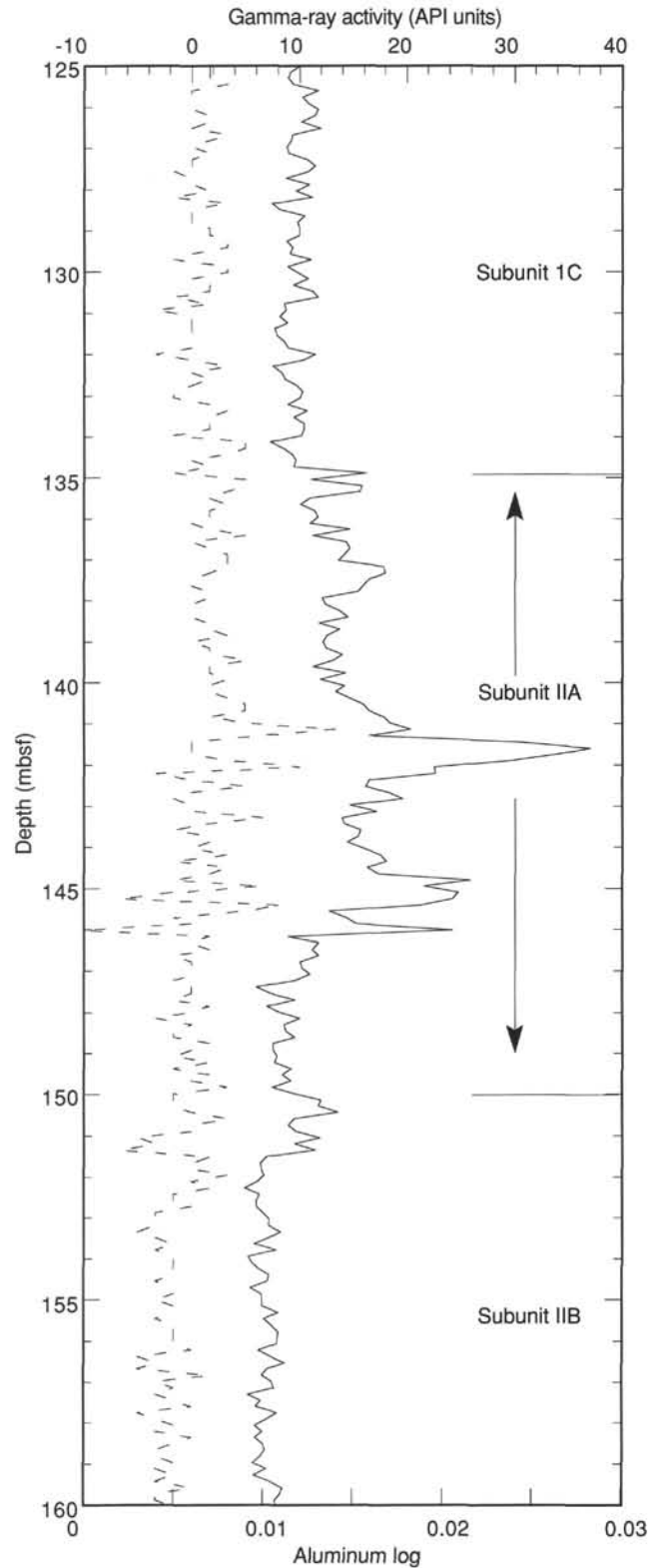


Figure 15. Borehole logs in Subunit IIA. The oxide-rich beds show up as peaks in the natural gamma-ray activity profile (solid line). Clay-rich oxide beds also show up as peaks in the aluminium log (dashed line), but the oxide-rich nannofossil ooze at the base is distinguished as a peak on the gamma-ray profile, but not in the aluminium record.

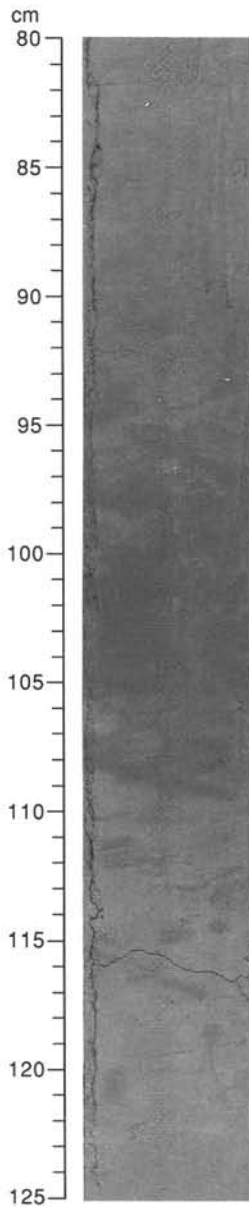


Figure 16. Alternation of foraminifer- and darker radiolarian-rich nannofossil ooze in Subunit IIB (Section 138-845B-17H-5 at 80–125 cm).

Summary of Depositional History at Site 845

The Neogene sequences recovered from Site 845 encompass two distinct sedimentary regimes. The first, from early to latest middle Miocene (Unit II), records persistent carbonate deposition having little variation from the dominant sediment type of foraminifer nannofossil ooze. The only variation from this regime is a regular, meter-scale interbedding of the dominant foraminifer nannofossil ooze, with darker, pyrite-bearing, radiolarian nannofossil ooze on a time scale of tens of thousands of years. This rhythm is more or less apparent throughout Subunit IIB. Early Miocene sedimentation rates (see “Sedimentation Rates” section, this chapter) were high (about 40 m/m.y.). Sedimentation rates decreased (to about 20 m/m.y.) in the early middle Miocene and increased to more than 30 m/m.y. near the CN4/ CN5A boundary. The change to higher sedimentation rates at the CN4/CN5A boundary is associated with an increase in the abun-

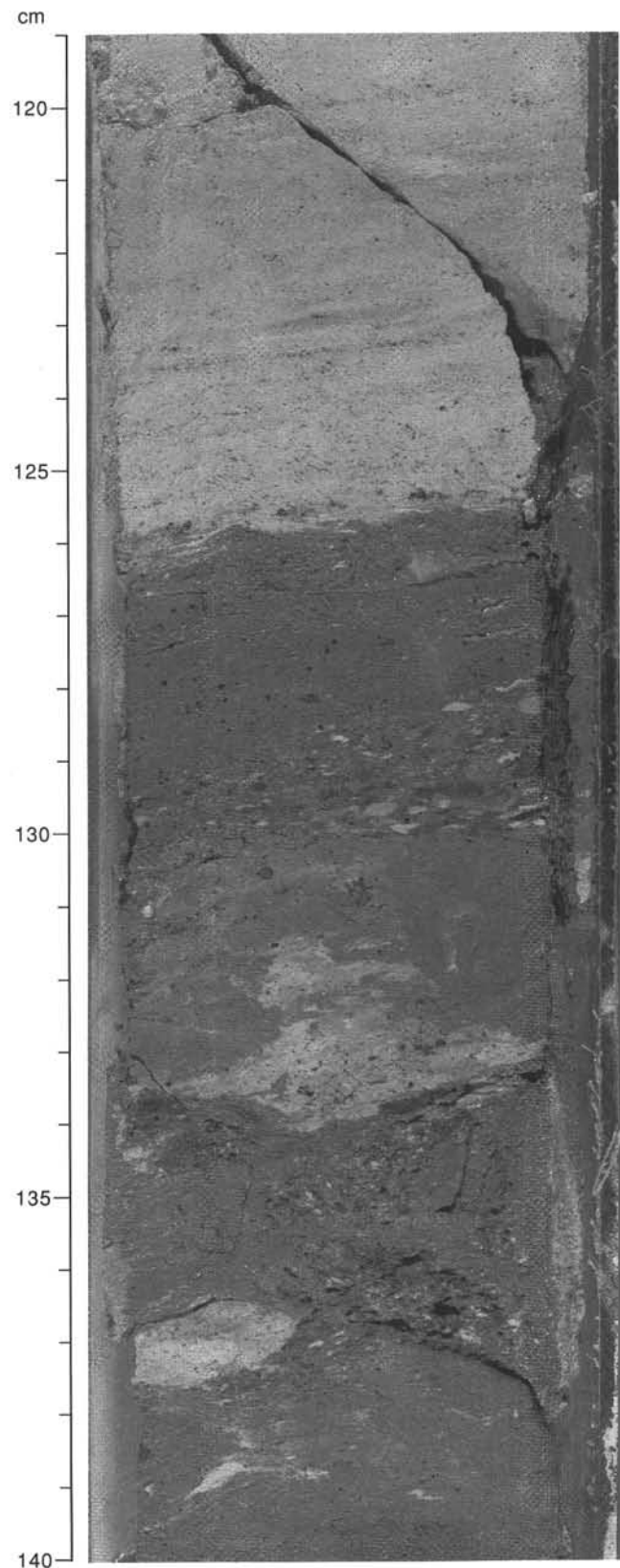


Figure 17. Microconglomerates and parallel laminations exhibiting evidence of redeposition near the base of lithologic Unit II (Section 138-845A-31X-3 at 119–140 cm).

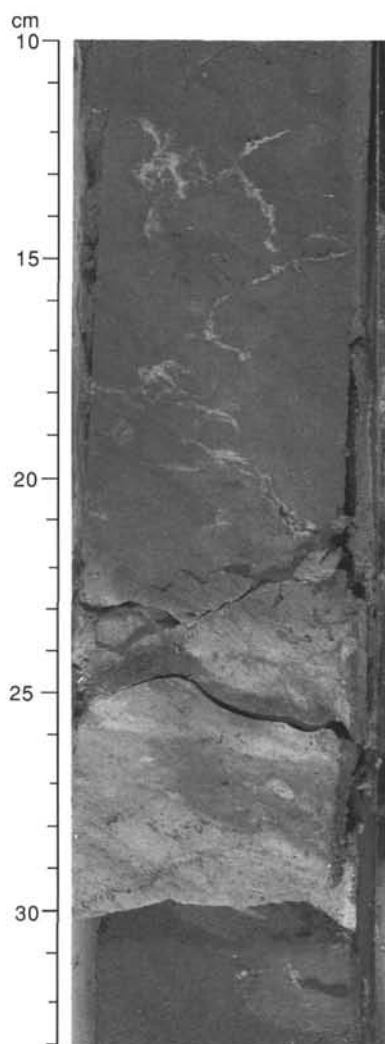


Figure 18. Calcite veining in Subunit IIC (Section 138-845A-31X-4 at 10–33 cm).

dance of radiolarians, with a contemporaneous decrease in abundance of foraminifers. Periods of deposition of diatom ooze occurred regularly during middle Miocene (CN5) time, as evidenced by diatom-rich burrow fills.

A sharp reduction occurred in the amount of carbonate deposition, starting from the latest middle Miocene (at about 11 Ma, NN7/8 boundary). This was associated with a reduction in sedimentation rates. A distinctive transitional unit (Subunit IIB) having clay and oxide-rich beds was deposited at low rates (about 12 m/m.y.), while carbonate deposition had ceased before 9 Ma (C4A/C5 boundary) and was replaced by deposition of clayey radiolarian ooze at higher (about 20 m/m.y.) sedimentation rates. The loss of microfossils up the core within this transitional unit shows evidence for progressively increasing carbonate dissolution, with first foraminifers, then coccoliths, and finally discoasters disappearing. Throughout this period of transition and otherwise slow deposition (from about 10.5–9.5 my), frequent thin beds of almost monospecific diatom ooze occurred (see “Biostratigraphy” section, this chapter). The proportion of carbonate increased again from around 8 Ma, with deposition of varying amounts of nanofossil rich sediment interbedded with siliceous clays in which radiolarians are the dominant microfossil component during the late Miocene. The proportion of nanofossils in the sediment decreases gradually through the late Miocene to a low near the Miocene/Plio-

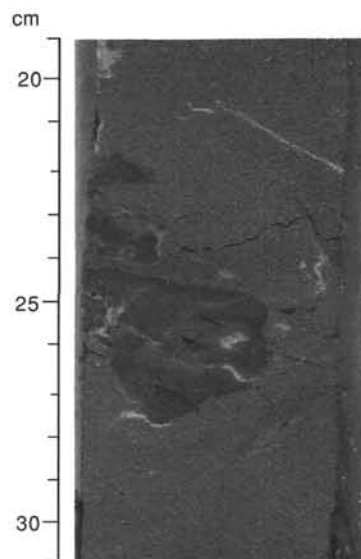


Figure 19. A basalt clast in a fine-grained matrix in Subunit IIC (Section 138-845A-31X-5 at 19–31 cm).

cene boundary. This is followed by a period of slower, clay-rich deposition at around 2 Ma before a rapid increase in sedimentation rates with deposition of more diatom-rich sediment during the Pleistocene.

BIOSTRATIGRAPHY

Sediments recovered from the three holes cored at Site 845 provide a continuous sedimentary record for the upper Pleistocene through the upper—lower Miocene. Calcareous nanofossils, radiolarians, and diatoms are generally present throughout the section providing a well-constrained stratigraphy for the sequence recovered (Tables 3 through 5, Fig. 26). The preservation of siliceous microfossils was generally good throughout the section; however, intervals of poor preservation were found in the upper Miocene and in the middle Miocene (Fig. 26). Sediments of the middle Miocene in particular (Cores 845B-22H through -27X) show evidence of solution and reprecipitation of the biogenic silica. Reworked, older radiolarians were found in Cores 845B-6H through -9H and 845B-14H through -16H.

With few exceptions, planktonic foraminifers are rare or absent in the upper half of the hole (down to Core 845A-17H), and in the lower part of the section the assemblage is dominated by robust and dissolution-resistant species. The calcareous nanofossils are dissolved in the Pleistocene-Pliocene part of the section, and only regain a good state of preservation in the upper to middle Miocene. The following discussion focuses on results from Holes 845A and 845B as only three cores were recovered from Holes 845C (equivalent to Subzones CN14b-CN12d).

Epoch boundaries are placed at the following stratigraphic positions:

Boundary	Hole	Depth (mbsf)	Depth (mcd)	Event
Pleistocene/Pliocene	845A	~35.0	37.2	T <i>Pterocanium prismatium</i>
late/early Pliocene	845B	53.15	59.88	Gauss (O)
Pliocene/Miocene	845A	79.50	87.51	Gilbert (O)
late/middle Miocene	845A	147.20	164.93	C5N (O)
early/middle Miocene	845A	~251.5	~276.7	T <i>Helicosphaera ampliaptera</i>

T = top occurrence; O = onset.

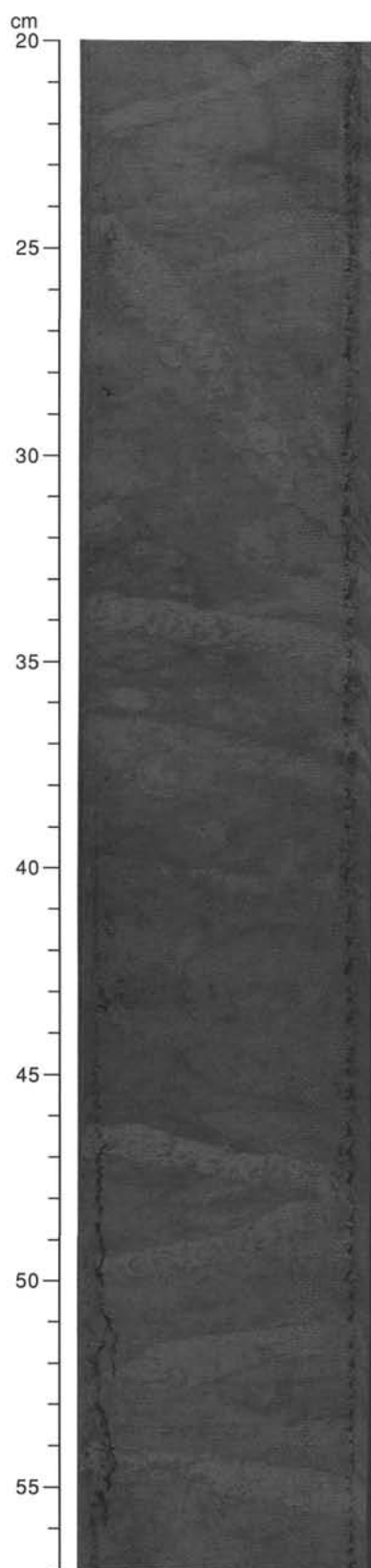


Figure 20. *Zoophycos* burrows in Subunit IA (Section 138-845C-3H-5 at 20–57 cm), showing one burrow with an unusually high (50°) angle of climb.

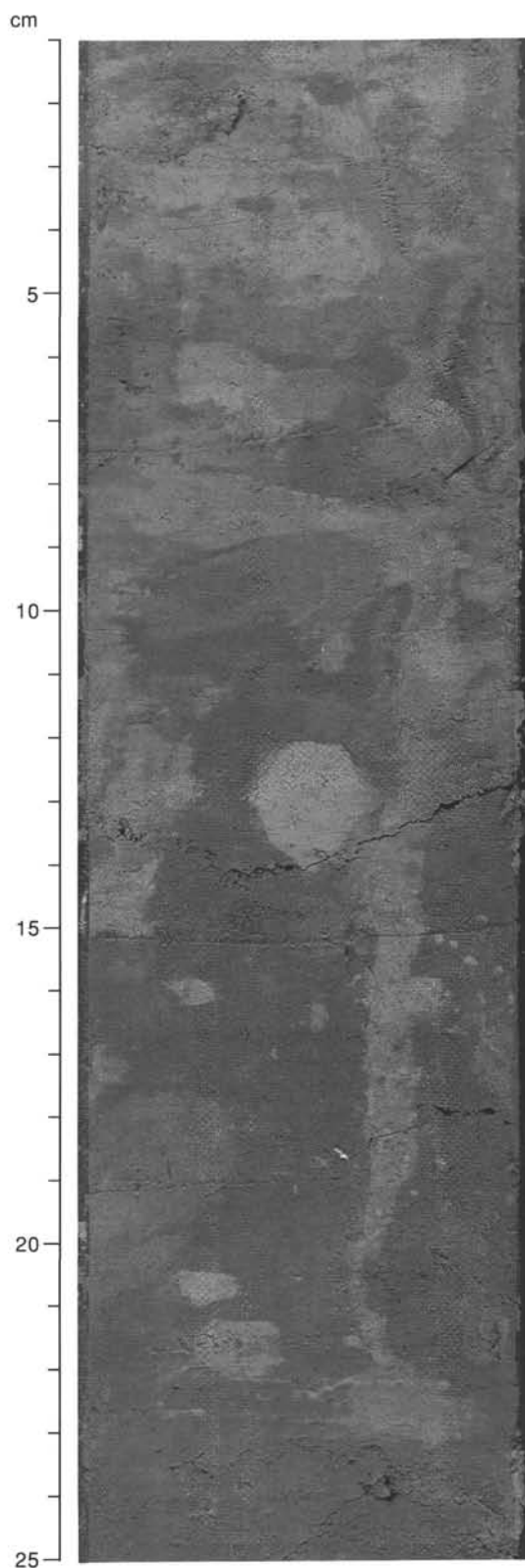


Figure 21. Complex burrowing in Subunit IB (Section 138-845A-9H-6 at 0–25 cm), showing *Chondrites* that cut *Skolithos*(?) in a background of solid burrows and *Planolites*.

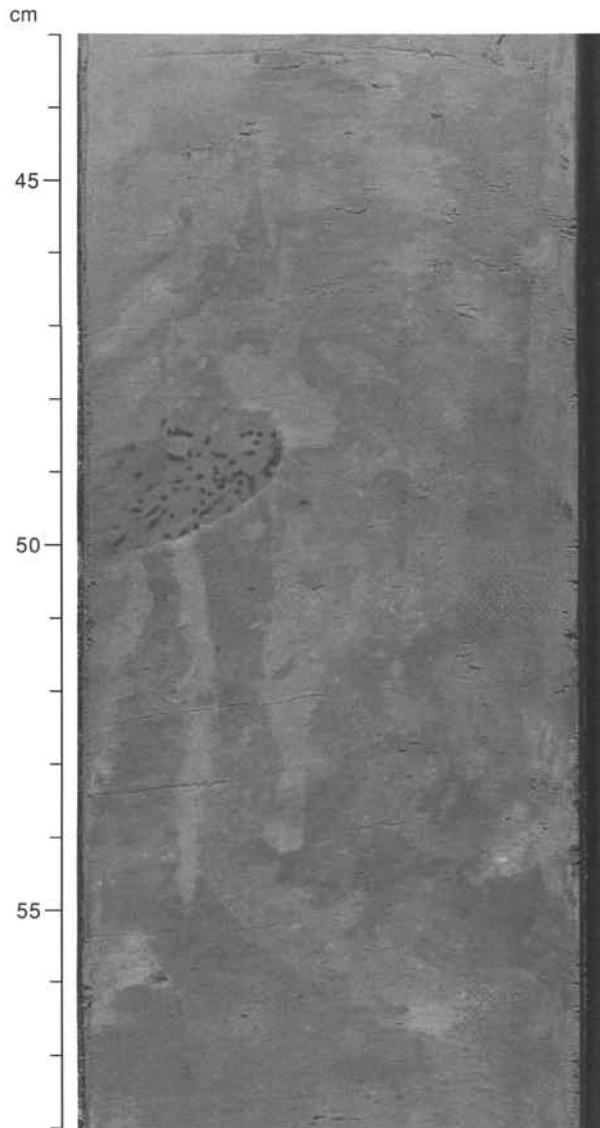


Figure 22. *Chondrites* that cut *Planolites* against a background of solid burrows, *Skolithos*, and an earlier generation of *Planolites* (Section 138-845B-15H-5 at 43–58).

Calcareous Nannofossils

Calcareous nannofossils recovered at Site 845 represent a stratigraphic succession from the upper Pleistocene (Zones CN14b of Okada and Bukry, 1980, and NN20 of Martini, 1971) through the lower Miocene (Zones NN3/NN4). Their relative abundance and preservation vary throughout the recovered sequence. In the Pleistocene–Pliocene interval (Cores 138-845A-1H through -7H, -845B-1H through -5H, and -845C-1H through -3H), calcareous nannofossils are generally rare and have moderate preservation. In some intervals (e.g., within Cores 138-845A-5H and -845B-6H) these are absent and in others, the assemblages are represented almost completely by discoasterids, together with a few other partially dissolved coccoliths. However, the presence of some diagnostic species in a few samples allowed us to assign a biostratigraphic zone in the upper sequence.

In most of the upper Miocene interval (80–145 mbsf), calcareous nannofossils are rare and exhibit dissolution. They are absent in Cores

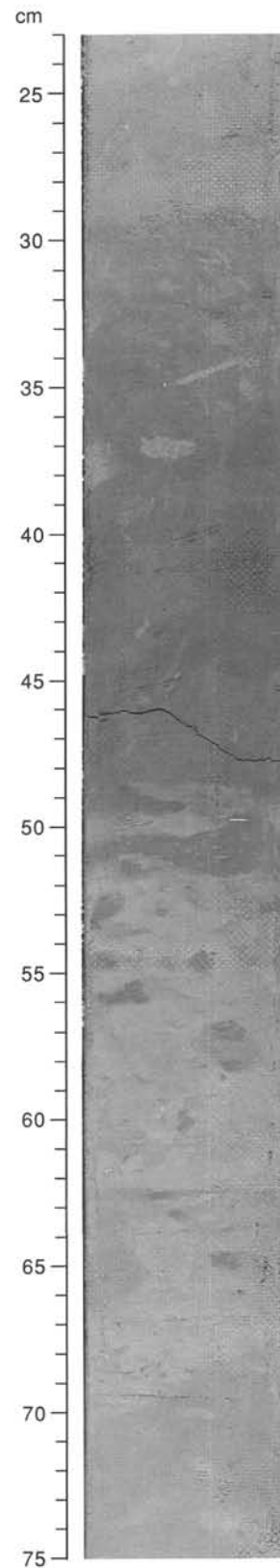


Figure 23. A burrowed, darker bed of radiolarian nannofossil ooze within paler foraminifer nannofossil ooze near the top of Subunit IIB (Section 138-845B-17H-6 at 23–75 cm).

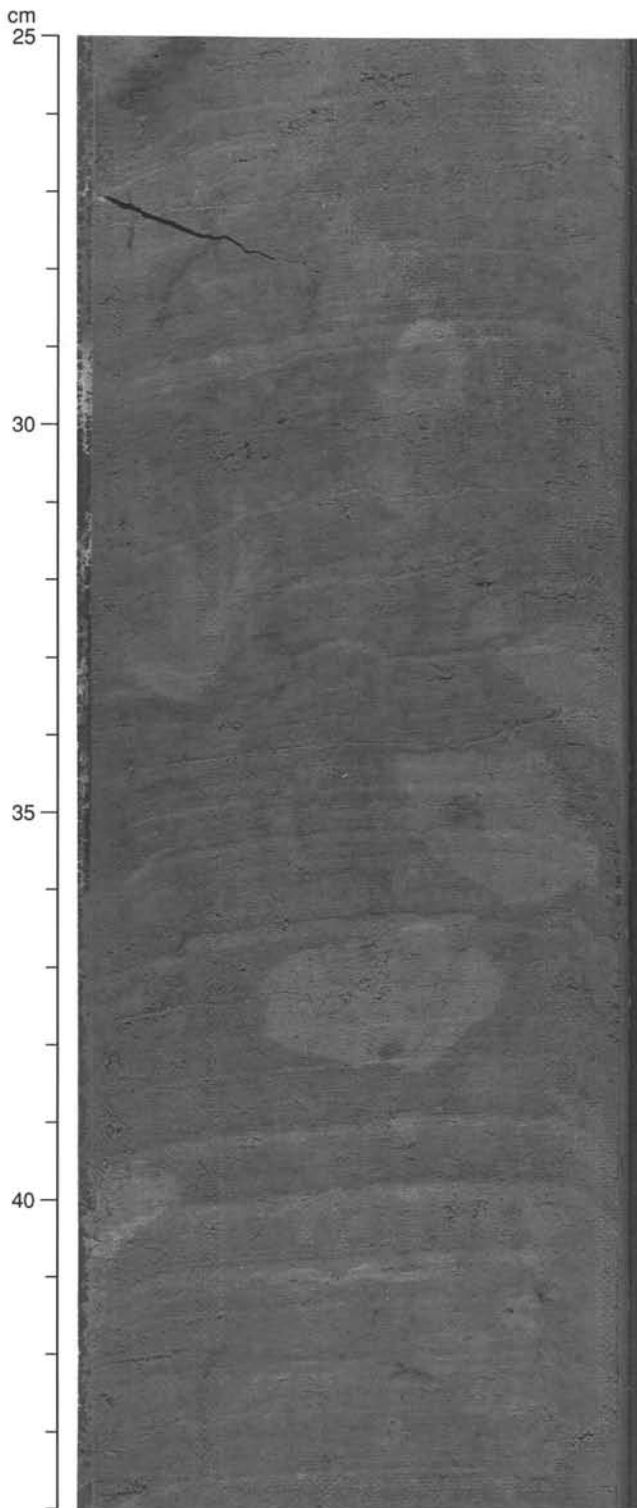


Figure 24. Fine, dark bluish, early diagenetic color lamination that cuts a *Planolites* burrow in Subunit IB (Section 138-845A-8H-3 at 25–44 cm).

138-845A-13H, -14H, and most of -15H. In the middle Miocene down to the upper–lower Miocene interval (145 mbsf to the bottom of Hole 845A), the nanofossil assemblage generally is abundant and diverse and exhibits moderate to good preservation. This part of the section is characterized by discoasterids (which show moderate overgrowth), helicoliths, sphenoliths and placoliths (mainly *Reticulofenestra* spp. and *Coccolithus* spp).

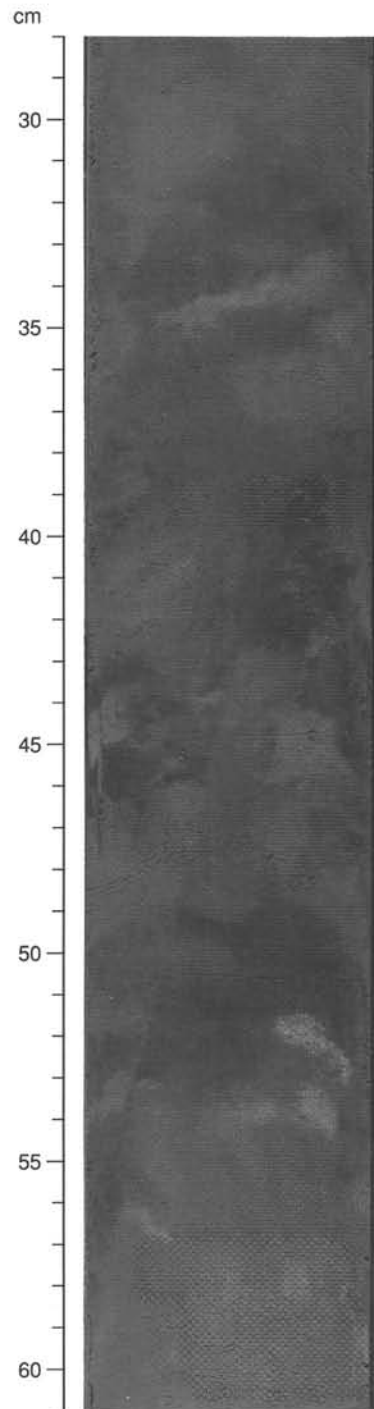


Figure 25. Small-scale faulting in Subunit IIA (Section 138-845B-15H-2 at 28–61 cm).

The calcareous nanofossils events recognized at Site 845 are presented in Table 3. The presence of *Gephyrocapsa oceanica* s.l. and the absence of *Pseudoemiliania lacunosa* (in Samples 138-845A-1H-CC to -3H-2, 42 cm, and -845B-1H-CC) allowed us to place these samples into the Pleistocene Zone CN14. The occurrence of *P. lacunosa* together with *G. oceanica* s.l. in Samples 138-845A-3H-3, 62 cm, -845B-2H-CC, and 845C-1H-CC, indicates Subzone CN14b or Zone CN13.

The Pliocene section is represented in Sample 138-845C-3H-CC, where Zone CN12d (NN18) was identified by the presence of *Discoaster brouweri*, and in Samples 138-845A-5H-3, 150 cm, to -7H-

CC and -845B-4H-CC to -7H-CC, where the presence of *Discoaster brouweri*, *D. pentaradiatus*, and *D. surculus* indicates Zone CN12 (NN17–NN16).

The upper Miocene discoasterids *Discoaster berggredi* and *D. quinqueramus* can be found continuously from Samples 138-845A-8H-7, 42 cm, to -12H-CC and Sample 138-845B-8H-CC to -12H-4, 145 cm, which were placed in Zone CN9 (NN11). In Hole 845A, we were able to recognize Subzone CN9b (Samples 138-845A-8H-7, 42 cm, to -11H-4, 32 cm) by the presence of *Amaurolithus primus* and *A. delicatus*. The occurrence of *Minylitha convallis* in Samples 138-845A-11H-5, 42 cm, to -13H-1, 45 cm, allowed us to assign these samples to Subzone CN9a.

As stated above, the samples examined in the interval from Samples 138-845A-13H-CC to -15H-4, 39 cm, have a dissolved nannofossil assemblage or no nannofossils. In the corresponding interval of Hole 845B, Samples 138-845B-12H-CC, -13H-CC, and -14H-CC are barren.

In the middle Miocene interval, the nannoflora are always abundant and well preserved. Slight overgrowth of discoasterid specimens in some samples prevented identification. *Discoaster hamatus* together with *Catinaster coalitus* and *C. calyculus* were found in Samples 138-845A-15H-CC and 845B-15H-2, 60 cm, which allowed us to place these samples in Subzone CN7b (NN9). *Catinaster coalitus*, whose first occurrence represents the base of Zone CN6 (NN8), is recorded in Samples 138-845A-16H-4, 32 cm, and -845B-15H-CC. The last occurrence of *Coccolithus miopelagicus* is found within this zone in Holes 845A and 845B (Samples 138-845A-16H-2, 42 cm, and 138-845B-15H-4, 60 cm).

The intervals from Samples 138-845A-16H-5, 40 cm, to -23X-5, 120 cm, and Samples 138-845B-16H-2, 42 cm, to -21H-CC correspond to Zone CN5 (NN7–NN6). The first occurrence of *Discoaster kugleri* defines the boundary between Subzones CN5b and CN5a and Zones NN7 and NN6, but generally, this form was not continuously present, and it was difficult for us to recognize where the discoasterid assemblage was overgrown. Questionable specimens of *D. kugleri* were found in Samples 138-845A-17-CC and -19-1H, 42 cm, and -845B-16H-CC, but these were not used to define the boundary between Subzones CN5b/CN5a and Zones NN7/NN6. Within the interval corresponding to Zone CN5, the following events were recognized: the last occurrence of *Coronocyclus nitescens* (between Samples 138-845A-19H-1, 42 cm, and -19H-2, 42 cm, and between

Samples 138-845B-18H-4, 112 cm, and -18H-CC), the first occurrence of *Triquetrorhabdulus rugosus* (Sample 138-845A-20H-1, 42 cm), the last occurrence of *Cyclargolithus floridanus* (between Samples 138-845A-22H-3, 42 cm, and -22H-4, 42 cm), and the first occurrence of *Reticulofenestra pseudumbilicus* (>7 µm) between Samples 138-845A-22H-4, 42 cm, and -22H-5, 42 cm.

Zone CN4 was defined by the last occurrence of *Sphenolithus heteromorphus* and the last occurrence of *Helicosphaera ampliaperta*. The first event occurs in Sample 138-845A-23X-4, 120 cm, and the second event occurs in Sample 138-845A-27X-5, 42 cm, which places the interval between these two levels in Zone CN4. The occurrence of *H. ampliaperta* throughout the lower part of the Hole 845A sequence (from Samples 138-845A-27X-5, 42 cm, to -31X-CC) places this interval in Zone CN4 (NN4). The lowermost fossiliferous samples from the core-catcher sample of Core 138-845A-31X showed an acme in abundance of *Sphenolithus heteromorphus*.

Planktonic Foraminifers

Planktonic foraminifers are rare and poorly preserved to absent in the upper part of Hole 845A (Pleistocene through upper Miocene) from Cores 138-845A-1H through -17H. Abundance and preservation vary from sample to sample in the lower part of the hole (middle and lower Miocene) from Cores 138-845A-18H through -31X. These species are common to abundant and moderately well-preserved in core-catcher Samples 138-845A-19H, -22H through -24X, and -28X through -30X. They are rare and poorly preserved in core-catcher Samples 138-845A-18H, -20H, -21H, -25X through -27X, -29X, and -31X.

Coarse fraction residues, whose amount is small in the interval from Samples 138-845A-7H-CC through -16H-CC, contain abundant to common radiolarians throughout the sedimentary sequence. Radiolarians constitute the main component of the residues above Core 138-845A-17H-CC. Sponge spicules and fish teeth are rare to few throughout the sequence. Echinoid spines are rare in the interval from Samples 138-845A-16H-CC through -31X-CC. Iron oxide micronodules are common from Samples 138-845A-27X-CC through -31X-CC.

Because of the rarity of the fauna and the absence of diagnostic species, we were unable to establish a zonation in the upper half of the hole from Samples 138-845A-1H-CC through -17H-CC,

Table 3. Sample and depth constraints of calcareous nannofossil events for Site 845.

Event	Hole 845A			Hole 845B		
	Interval (cm)	Depth (mbsf)	Depth (mcd)	Interval (cm)	Depth (mbsf)	Depth (mcd)
T <i>Pseudoemiliana lacunosa</i>	3H-2, 42–3H-3, 42	19.02–20.52	19.88–21.38	1H-CC–2H-CC	9.73–21.49	12.9–25.02
T <i>Discoaster brouweri</i>	5H-2, 42–5H-4, 42	38.02–41.02	41.53–44.53	3H-CC–4H-CC	27.95–41.19	32.25–45.07
T <i>Discoaster quinqueramus</i>	8H-5, 42–8H-7, 42	71.02–74.02	77.32–80.32	7H-CC–8H-CC	69.85–79.57	76.46–87.95
B <i>Amaurolithus primus</i>	11H-4, 32–11H-5, 42	97.92–99.52	107.68–109.28			
B <i>Discoaster berggredi</i>	12H-CC–13H-1, 45	112.36–112.55	123.69–125.16	12H-4, 145–12H-5, 145	113.55–115.05	126.53–128.03
B <i>Discoaster hamatus</i>	15H-CC–16H-1, 42	141.13–141.02	156.99–158.75	15H-2, 60–15H-3, 60	138.20–139.70	156.50–158.00
T <i>Coccolithus miopelagicus</i>	16H-1, 42–16H-2, 42	141.02–142.52	158.75–160.25	15H-2, 60–15H-4, 60	138.20–141.20	156.50–159.50
B <i>Catinaster coalitus</i>	16H-4, 32–16H-5, 40	145.42–147.00	163.15–164.73	15H-CC–16H-1, 42	144.56–146.02	162.86–165.72
T <i>Coronocyclus nitescens</i>	19H-1, 42–19H-2, 42	169.52–171.10	190.18–191.66	18H-4, 112–18H-CC	170.22–174.53	190.52–194.83
B <i>Triquetrorhabdulus rugosus</i>	20H-1, 42–20H-2, 42	179.02–180.52	201.35–202.85			
T <i>Cyclargolithus floridanus</i>	22H-3, 42–22H-4, 42	201.02–202.52	226.25–227.75			
B <i>Reticulofenestra pseudumbilicus</i>	22H-4, 42–22H-5, 42	202.52–204.02	227.75–229.25			
T <i>Sphenolithus heteromorphus</i>	23X-3, 120–23X-4, 120	211.30–222.80	236.53–238.03			
T <i>Helicosphaera ampliaperta</i>	27X-4, 42–27X-5, 42	250.72–252.22	275.95–277.45			

T = top occurrence; B = bottom occurrence.

Table 4. Sample and depth constraints of radiolarian events for Site 845.

Event	Hole 845A (section)	Hole 845A depth (mbsf)	Hole 845A depth (mcd)	Hole 845B (section)	Hole 845B depth (mbsf)	Hole 845B depth (mcd)
T <i>Stylatractus universonis</i>	1H-CC-2H-3	7.60-10.10	7.60-10.98	1H-CC-2H-CC	9.73-21.49	12.09-25.02
B <i>Collosphaera tuberosa</i>	3H-3-3H-5	21.20-24.20	22.06-25.06			
T <i>Lamprocyrtis neoheteroporos</i>	3H-3-3H-5	21.20-24.20	22.06-25.06			
T <i>Anthocyrtidium angulare</i>	3H-5-3H-CC	24.20-26.99	25.06-27.85			
T <i>Theocorythium vetulum</i>	3H-5-3H-CC	24.20-26.99	25.06-27.85			
B <i>Lamprocyrtis nigrinae</i>	3H-CC-4H-3	26.99-30.70	27.85-30.84			
B <i>Theocorythium trachelium</i>	4H-3-4H-5	30.70-33.70	32.83-35.83			
B <i>Pterocorys minythorax</i>	3H-CC-4H-3	26.99-30.70	27.85-32.83			
B <i>Anthocyrtidium angulare</i>	4H-5-4H-CC	33.70-36.49	35.83-38.62			
T <i>Pterocanium prismatium</i>	4H-5-4H-CC	33.70-36.49	35.83-38.62			
T <i>Lamprocyrtis heteroporos</i>	4H-3-4H-5	30.70-33.70	32.83-35.83			
T <i>Anthocyrtidium jenghisi</i>	4H-CC-5H-5	36.49-43.20	38.62-46.71			
B <i>Theocalypta davisiana</i>	5H-CC-6H-3	46.09-48.70	49.60-52.78			
T <i>Stichocorys peregrina</i>	5H-CC-6H-3	46.09-48.70	49.60-52.78			
T <i>Anthocyrtidium pliocenica</i>	6H-5-6H-CC	52.70-55.64	56.78-59.72			
B <i>Lamprocyrtis neoheteroporos</i>	6H-3-6H-5	49.70-52.70	53.78-56.78			
B <i>Lamprocyrtis heteroporos</i>	6H-3-6H-5	49.70-52.70	53.78-56.78			
T <i>Phormostichoartus fistula</i>	6H-5-6H-CC	52.70-55.64	56.78-59.72			
T <i>Lychnodictyum audax</i>	6H-CC-7H-3	55.64-59.10	59.72-63.96			
T <i>Phormostichoartus doliolum</i>	6H-CC-7H-3	55.64-59.10	59.72-63.96			
B <i>Amphirhopalum ypsilon</i>	6H-CC-7H-3	55.64-59.10	59.72-63.96			
B <i>Spongaster tetras</i>	6H-CC-7H-3	55.64-59.10	59.72-63.96			
T <i>Didymocyrtis penultima</i>	7H-3-7H-5	59.20-62.20	64.06-67.06	5H-CC-6H-CC	48.40-59.97	53.80-66.70
B <i>Pterocanium prismatium</i>	7H-CC-8H-3	64.91-68.70	69.77-75.00			
T <i>Solenosphaera omnitubus</i>	8H-3-8H-5	68.70-71.70	75.00-78.00	7H-CC-8H-CC	69.85-79.57	76.46-87.95
T <i>Siphostichartus corona</i>	11H-CC-12H-3	103.21-106.70	112.97-117.03			
T <i>Acrobotrys tritubus</i>	10H-CC-11H-3	93.61-97.20	102.09-106.96			
T <i>Stichocorys johnsoni</i>	9H-CC-10H-3	84.07-87.70	92.08-96.18			
<i>Stichocorys delmontensis</i> > <i>S. peregrina</i>	10H-5-10H-CC	90.70-93.61	99.18-102.09			
T <i>Calocycletta caepa</i>	10H-CC-11H-3	93.61-97.20	102.09-106.96			
B <i>Solenosphaera omnitubus</i>	10H-CC-11H-3	93.61-97.20	102.09-106.96			
T <i>Diartus hughesi</i>	11H-5-11H-CC	100.20-103.21	109.96-112.97			
B <i>Acrobotrys tritubus</i>	11H-5-11H-CC	100.20-103.21	109.96-112.97			
T <i>Stichocorys wolffii</i>	13H-5-13H-CC	119.20-122.13	131.81-134.74			
T <i>Botryostrobus miralestensis</i>	12H-3-12H-5	106.70-109.70	118.03-121.03	11H-CC-12H-CC	108.02-117.62	120.13-130.60
T <i>Diartus pettersoni</i>	12H-5-12H-CC	109.70-112.36	121.03-123.69			
B <i>Lithopera bacca</i>	15H-5-15H-CC	138.20-141.13	154.06-156.99			
<i>Diartus pettersoni</i> > <i>D. hughesi</i>	13H-3-13H-5	116.20-119.20	128.81-131.81	11H-CC-12H-CC	108.02-117.62	120.13-130.60
B <i>Diartus hughesi</i>	13H-CC-14H-3	122.13-125.70	134.74-139.68			
T <i>Cyrtocapsella japonica</i>	15H-5-15H-CC	138.20-141.13	154.06-156.99			
T <i>Lithopera thornburgi</i>	16H-CC-17H-3	150.62-154.20	168.35-173.01			
T <i>Carpocanium cristata</i>	15H-CC-16H-3	141.13-144.70	156.99-162.13			
T <i>Lithopera renzae</i>	17H-CC-18H-3	159.95-163.70	178.76-182.98			
T <i>Cyrtocapsella cornuta</i>	17H-3-17H-5	154.20-157.20	173.01-176.01	16H-CC-17H-CC	155.55-165.17	175.25-184.97
B <i>Diartus pettersoni</i>	18H-3-18H-5	163.70-166.70	182.98-185.98	16H-CC-17H-CC	155.55-165.17	175.25-184.97
T <i>Dorcadospyrus alata</i>	18H-3-18H-5	163.70-166.70	182.98-185.98	16H-CC-17H-CC	155.55-165.17	175.25-184.97
B <i>Cyrtocapsella japonica</i>	19H-CC-20H-3	179.16-182.70	199.82-205.03	18H-CC-19H-CC	174.53-183.73	194.83-204.23
B <i>Calocycletta caepa</i> s.s.	21H-CC-22H-3	198.13-201.70	221.36-226.93			
B <i>Lithopera thornburgi</i>	22H-CC-23X-3	207.10-211.20	232.82-236.43			
T <i>Stichocorys armata</i>	22H-CC-23X-3	207.10-211.20	232.82-236.43			
T <i>Liriospyris parkerae</i>	24X-CC-25X-3	226.50-230.60	243.48-255.73			
T <i>Acrocubus octopyle</i>	24X-CC-25X-3	218.25-230.60	243.48-255.83			
T <i>Carpocanium bramlettei</i>	24X-CC-25X-3	218.25-230.60	243.48-255.83			
T <i>Calocycletta costata</i>	25X-5-25X-CC	233.60-236.09	258.83-261.32			
<i>Dorcadospyrus dentata</i> > <i>Dorcadospyrus alata</i>	27X-2-27X-6	248.40-254.40	273.63-279.63			
T <i>Liriospyris stauropora</i>	27X-6-27X-CC	254.40-255.00	279.63-280.76			
B <i>Liriospyris parkerae</i>	27X-6-27X-CC	254.40-255.00	279.63-280.76			
T <i>Stichocorys diaphenes</i>	28X-3-28X-5	259.10-262.10	284.33-287.33			
B <i>Carpocanium bramlettei</i>	28X-5-28X-CC	262.10-264.60	287.33-289.79			
B <i>Acrocubus octopyle</i>	30X-5-30X-CC	306.50-309.10	281.27-283.90			
T <i>Carpocanium cingulata</i>	30X-3-30X-5	303.50-306.50	278.27-281.27			
T <i>Didymocyrtis prismatica</i>	30X-5-30X-CC	306.50-309.10	281.27-283.90			
B <i>Calocycletta costata</i>						

T = top occurrence; B = bottom occurrence. An ">" denotes an evolutionary transition.

except for Sample 138-845A-12H-CC, which could be assigned to the upper Miocene Zone N17 on the basis of the occurrence of *Globorotalia plesiotumida*. In the upper interval of the hole, from Samples 138-845A-1H-CC through -5H-CC, the assemblages yielded rare *Globorotalia menardii*, *G. tumida* (from Samples 138-845A-1H-CC through -3H-CC), *Neogloboquadrina dutertrei*, *Globigeri-*

noides sacculifer, and *G. ruber*, and very rare *Pulleniatina obliquiloculata* (right-coiling in Sample 138-845A-1H-CC and left-coiling in Sample 138-845A-4H-CC). In the interval from Samples 138-845A-6H-CC through -17H-CC the fauna include a few specimens of *G. menardii*, *Globigerinoides obliquus*, *G. sacculifer*, *Neogloboquadrina humerosa* (Sample 845A-11H-CC), and *G. plesiotumida* (Sample 138-845A-

Table 4 (continued).

Event	Hole 845C (section)	Hole 845C depth (mbsf)	Hole 845C depth (mcd)
T <i>Stylatractus universon</i>			
B <i>Collosphaera tuberosa</i>			
T <i>Lamprocyrtis neoheteroporos</i>			
T <i>Anthocyrtidium angulare</i>			
T <i>Theocorythium vetulum</i>			
B <i>Lamprocyrtis nigrinae</i>	1H-CC-1H-CC	20.00-29.84	21.00-30.84
T <i>Theocorythium trachelium</i>			
B <i>Pterocorys minythorax</i>	1H-CC-1H-CC	20.00-29.84	21.00-30.84
B <i>Anthocyrtidium angulare</i>			
T <i>Pterocanium prismatium</i>			
T <i>Lamprocyrtis heteroporos</i>			
T <i>Anthocyrtidium jenghisi</i>	1H-CC-2H-CC	29.84-39.52	30.84-41.40
B <i>Theocalyptra davisiana</i>	3H-CC	48.63	51.93
T <i>Stichocorys peregrina</i>	3H-CC	48.63	51.93
T <i>Anthocyrtidium pliocenica</i>			
B <i>Lamprocyrtis neoheteroporos</i>			
B <i>Lamprocyrtis heteroporos</i>			
T <i>Phormostichoartus fistula</i>			
T <i>Lychnodictyum audax</i>			
T <i>Phormostichoartus doliolum</i>			
B <i>Amphirhopalum ypsilon</i>			
B <i>Spongaster tetras</i>			
T <i>Didymocyrtis penultima</i>			
B <i>Pterocanium prismatium</i>			
T <i>Solenosphaera omnitubus</i>			
T <i>Siphostichartus corona</i>			
T <i>Acrobotrys tritubus</i>			
T <i>Stichocorys johnsoni</i>			
<i>Stichocorys delmontensis</i>			
> <i>S. peregrina</i>			
T <i>Calocyclus caepa</i>			
B <i>Solenosphaera omnitubus</i>			
T <i>Diartus hughesi</i>			
B <i>Acrobotrys tritubus</i>			
T <i>Stichocorys wolffii</i>			
T <i>Botryostrobos miralestensis</i>			
T <i>Diartus pettersoni</i>			
B <i>Lithopera bacca</i>			
<i>Diartus pettersoni</i> > <i>D. hughesi</i>			
B <i>Diartus hughesi</i>			
T <i>Cyrtocapsella japonica</i>			
T <i>Lithopera thornburgi</i>			
T <i>Carpocanium cristata</i>			
T <i>Lithopera renzae</i>			
T <i>Cyrtocapsella cornuta</i>			
B <i>Diartus pettersoni</i>			
T <i>Dorcadospyrus alata</i>			
B <i>Cyrtocapsella japonica</i>			
B <i>Calocyclus caepa</i> , s.s.			
B <i>Lithopera thornburgi</i>			
T <i>Stichocorys armata</i>			
T <i>Liriospyris parkerae</i>			
T <i>Acrocubus octopyle</i>			
T <i>Carpocanium bramlettei</i>			
T <i>Calocyclus costata</i>			
<i>Dorcadospyrus dentata</i>			
> <i>Dorcadospyrus alata</i>			
T <i>Liriospyris stauropora</i>			
B <i>Liriospyris parkerae</i>			
T <i>Stichocorys diaphenes</i>			
B <i>Carpocanium bramlettei</i>			
B <i>Acrocubus octopyle</i>			
T <i>Carpocanium cingulata</i>			
T <i>Didymocyrtis prismatica</i>			
B <i>Calocyclus costata</i>			

12H-CC). Samples 138-845A-13H-CC through -16H-CC are barren of planktonic foraminifers.

In the lower part of the sequence, the middle and lower Miocene assemblages have been dominated by robust species resistant to dissolution, mainly *Globoquadrina venezuelana* and *Globorotalia mayeri*. Less common species, whose abundance varies from sample to sample, include *Globoquadrina dehiscens*, *Dentoglobigerina al-*

tispira, *Shaeroidinellopsis disjuncta*, *Globigerinoides sacculifer*, *G. obliquus*, and *G. subquadratus*. A detailed zonation could not be established on the basis of these nondiagnostic species, and because of the poor preservation, the first and last occurrences of diagnostic species cannot be taken as reliable stratigraphic datums. For this reason, a table of stratigraphic datums for foraminifers is not presented here. However, some zonal intervals were identified on the basis of the presence of a few diagnostic species. Samples 138-845A-18H-CC and -19H-CC were assigned to Zone N12, based on the co-occurrence of *Globorotalia foehsi lobata* and *G. foehsi foehsi*. Samples 138-845A-20H-CC and -21H-CC, which contain *G. foehsi* s.l., but without *G. foehsi lobata*, were assigned to the undifferentiated interval N11-N12. Samples 138-845A-22H-CC and -23X-CC were assigned to the undifferentiated interval N10-N12, based on the occurrence of *Globorotalia praemenardii*. Samples 138-845A-24X-CC and -25X-CC, which contain *Orbulina suturalis* and *Praeorbulina circularis*, were assigned to Zone N9. Samples 138-845A-26X-CC and -27X-CC, rich in radiolarians, yielded a poor planktonic foraminiferal fauna that could not be assigned to a distinct zonal interval. Sample 138-845A-28X-CC was assigned to Zone N8, based on the presence of *Praeorbulina sicana*. Samples 138-845A-29X-CC through -31X-CC are not older than N8 on the basis of the absence of *Catapsydrax dissimilis*. However, the nominate taxon of N8, *P. sicana*, was not found in this interval, possibly as a result of dissolution.

Radiolarians

Radiolarians sampled at Site 845 ranged in age from the Quaternary (*Collosphaera tuberosa* Zone) to the latest part of the early Miocene (*Calocyclus costata* Zone). The most recent radiolarian zone (*Buccinosphaera invaginata*) was not identified in any of the holes. The oldest material recovered is nearly identical with that found in Site 844, with the last occurrence of *Didymocyrtis prismatica* found in Samples 138-845A-30X-CC and -844B-31X-5, 110-111 cm.

The Pleistocene-Pliocene section is expanded and well-preserved at this site. Nearly all the radiolarian zones were identified, and most of the datums from this interval were well constrained (Table 4). *Spongaster pentas* was not identified, and *S. berminghamsi* was not found consistently. We also noted that *Theocorythium trachelium* was sparse and somewhat erratic in its occurrence, while its predecessor, *T. vetulum*, was common and consistently present in its normal range. Reworked older microfossils from the middle to upper Miocene were common in the lower Pliocene and uppermost Miocene parts of the section—particularly in the *Solenosphaera omnitubus* and upper part of the *Didymocyrtis penultima* zones. Traces of reworked older radiolarians were scattered throughout the Pleistocene-Pliocene part of the section.

Radiolarians were common to abundant throughout the Miocene part of the section, except in the section just above the basement (Core 138-845A-30X is barren of radiolarians below section 1). Preservation in the rest of the Miocene section generally was moderate to good, with some intervals of poor preservation within the *Dorcadospyrus alata* Zone. Dissolution and reprecipitation of silica within the sediment aggregated it into clumps that remained after initial acid treatment and sieving.

All major radiolarian zones of the upper and middle Miocene were identified, as were most of the datums commonly noted in previous studies of the tropical oceans (Table 4). One datum is of particular interest. Just below the base of the *Diartus pettersoni* Zone, the apparent final appearance of *Dorcadospyrus alata* occurs. The legs of the specimens in these samples are more robust than usual, and the spines on the legs are barely discernable. Below this level, a short interval was seen where specimens of *D. alata* were not found; deeper, the more typical form of *D. alata* does appear. *D. alata* is the last known species in a long evolutionary lineage; however, the apparent final appearance of the robust form of *D. alata* is somewhat younger

Table 5. Sample and depth constraints of diatom events for Site 845.

Event	Hole 845A			Hole 845B		
	Interval	Depth (mbsf)	Depth (mcd)	Interval	Depth (mbsf)	Depth (mcd)
T <i>Nitzschia reinholdii</i>	2H-CC-3H-CC	17.21-26.99	18.09-27.85	1H-CC-2H-CC	9.73-21.49	12.09-25.02
B <i>Pseudoeunotia doliolus</i>	4H-CC-5H-CC	36.49-46.09	38.62-49.60	3H-CC-4H-CC	27.95-41.19	32.25-45.07
T <i>Nitzschia jouseae</i>	5H-CC-6H-2	46.09-49.10	49.60-52.61	4H-CC-5H-CC	41.49-48.49	45.07-53.80
B <i>Rhizosolenia praebergonii</i>	5H-CC-6H-2	46.09-49.10	49.60-52.61	5H-CC-6H-CC	49.49-59.97	53.87-66.70
T <i>Nitzschia jouseae</i>	7H-CC-8H-CC	64.91-74.55	69.77-80.85	6H-CC-7H-CC	59.97-69.85	66.70-76.46
T <i>Thalassiosira miocenica</i>	8H-CC-9H-CC	74.55-84.07	80.85-92.08			
T <i>Nitzschia miocenica</i>	8H-CC-9H-CC	74.55-84.07	80.85-92.08			
B <i>Thalassiosira miocenica</i>	9H-CC-10H-CC	84.07-93.61	92.08-102.09			
B <i>Thalassiosira convexa</i>	9H-CC-10H-CC	84.07-93.61	92.08-102.09			
B <i>Nitzschia miocenica</i>	10H-CC-11H-CC	93.61-103.21	102.09-112.97			
T <i>Thalassiosira yabei</i>	11H-CC-12H-CC	103.21-112.36	112.97-123.69			
T <i>Denticulopsis hustedtii</i>	13H-CC-14H-CC	122.13-131.67	134.74-145.65			
T <i>Actinocyclus ingens</i>	18H-CC-19H-CC	169.69-179.16	188.97-199.82			
T <i>Coscinodiscus lewisianus</i>	20H-3-20H-7	182.11-187.90	205.15-210.20			
T <i>Cestodiscus peplum</i>	24X-CC-26X-CC	218.25-236.09	243.48-270.75			
B <i>Cestodiscus peplum</i>	29X-CC-30X-CC	274.35-283.87	299.58-309.10			

T = top occurrence; B = bottom occurrence.

than the last appearance datum (LAD) for *D. alata* indicated in previous studies. We are unclear at present whether previous studies noted only the final appearance of the more typical *D. alata*.

Diatoms

Diatoms recovered at Site 845 represent a continuous stratigraphic interval from the upper Quaternary *Pseudoeunotia doliolus* Zone through subzone B of the lower Miocene *Crucidentacula nicobarica* Zone of Barron (1985). Diatoms observed exhibit good preservation in the Pleistocene and Pliocene intervals and poor to moderate preservation in the Miocene interval. Abundances of diatoms vary from sample to sample, but generally, few to common diatoms can be seen through the recovered sequence. The one exception is Sample 138-845A-31X-CC, which is barren of diatoms.

Characteristic species of the diatom flora at Site 845 include *Actinocyclus ingens*, *Azpeitia nodulifer*, *Cestodiscus pulchellus*, *Coscinodiscus marginatus*, *Craspedodiscus coscinodiscus*, *Crucidentacula nicobarica*, *Denticulopsis hustedtii*, *Hemidiscus cuneiformis*, *Nitzschia cylindrica*, *Nitzschia jouseae*, *Nitzschia marina*, *Nitzschia reinholdii*, *Pseudoeunotia doliolus*, *Rossiella paleacea*, *Thalassionema nitzschoides*, *Thalassiosira convexa*, *Thalassiosira oestrupii*, *Thalassiosira yabei*, and *Thalassiothrix longissima*. The diatom flora allowed us to recognize the previously defined diatom zones of Barron (1985). However, accurate placement of secondary events, in the lower and middle Miocene interval, was often difficult as a result of variation in the preservational state of the diatom assemblage.

Cores 138-845A-1H and -2H and -845B-1H correspond to the Quaternary *P. doliolus* Zone on the basis of the occurrence of *P. doliolus* without *N. reinholdii*. Samples 138-845A-3H-2, 60 cm, through -4H-CC and Samples 138-845B-2H-CC and -3H-CC were assigned to the Quaternary *N. reinholdii* Zone, based on the co-occurrence of *N. reinholdii* and *P. doliolus*. Diatoms are generally well-preserved and common throughout this interval.

Samples 138-845A-4H-CC and -5H-CC and Sample 138-845B-5H-CC were assigned to the *Rhizosolenia praebergonii* Zone. The occurrence of *R. praebergonii* without *T. convexa* in Sample 138-845B-4H-CC allowed us to place these samples into Subzone C of the *R. praebergonii* Zone. The occurrence of *R. praebergonii* and *T. convexa* in Sample 138-845A-5H-CC without *N. jouseae* allowed us to place this sample in Subzone B of the *Rhizosolenia praebergonii* Zone. Sample 138-845B-5H-CC was placed into Subzone A of the *R. praebergonii* Zone, based on the occurrence of *R. praebergonii*, *T. convexa*, and *N. jouseae*.

Samples 138-845A-6H-2, 120 cm, through -7H-CC and Samples 138-845B-6H-CC and -7H-CC contain rare-to-common specimens of *N. jouseae* and were placed in the *Nitzschia jouseae* Zone. This zonal placement was supported by the co-occurrence of *T. convexa* and *Thalassiosira oestrupii* without *R. praebergonii* in the samples.

The interval from the first occurrence of *N. jouseae* (Sample 138-845A-7H-CC/845B-7H-CC) through the first occurrence of *T. convexa* (Sample 138-845A-9H-CC/845B-8H-CC) was assigned to the *Thalassiosira convexa* Zone. The occurrence of *Thalassiosira miocenica* and *Nitzschia miocenica* without *Thalassiosira praeconvexa* suggests that these samples are equivalent to Subzone B of this zone. The base of the *T. convexa* Zone could not be identified because of the absence of age-diagnostic species in Samples 138-845B-9H-CC and -10H-CC.

Samples 138-845A-10H-CC and -11H-CC were assigned to the *N. miocenica* and *N. porteri* zones, respectively. Sample 138-845B-11H-CC contains rare, moderately well-preserved diatoms. The occurrence of *Thalassiosira burkiana* in this sample without *Thalassiosira yabei* suggests placement of this sample into the lower portion of the *N. porteri* Zone.

T. yabei is last found in Samples 138-845A-12H-CC and -845B-13H-CC, suggesting that these samples are approximately equivalent and mark the top of the *T. yabei* Zone. The base of the *T. yabei* Zone could not be recognized as a result of the rare occurrence and poor preservation of diatoms from Cores 845A-15H-CC through 17H-CC and 845B-15H-CC. The occurrence of *Craspedodiscus coscinodiscus*, *Coscinodiscus gigas* var. *diorama*, *T. yabei*, *Cestodiscus pulchellus*, and *Denticulopsis hustedtii* indicate that Samples 138-845A-18H-CC and -845B-16H-CC are equivalent to the lower portion of the middle Miocene *Craspedodiscus coscinodiscus* Zone. Samples 138-845A-19H-CC and -20H-3, 120-121 cm and Sample 138-845B-18H-CC tentatively were assigned to the *Coscinodiscus gigas* var. *diorama* Zone, based on the occurrence of *Actinocyclus ingens*, *Denticulopsis hustedtii*, and *C. nicobarica*. The marker species for the *C. gigas* var. *diorama*/*Craspedodiscus coscinodiscus* zonal boundary was not observed.

Coscinodiscus lewisianus, which marks the top of the *C. lewisianus* Zone, is last found in Samples 138-845A-20H-CC and -845B-20H-CC. *Cestodiscus peplum* is last found in Sample 138-845A-26X-CC, which allowed us to place this sample in the *C. peplum* Zone. Unfortunately, Sample 138-845A-25X-CC contains rare nonage-diagnostic specimens preventing a more precise placement of this zonal boundary. Samples 138-845A-26X-CC through -29X-CC were assigned to the *C. peplum* Zone on the basis of the occurrence of *C.*

peplum. The occurrence of *Crucidentacula nicobarica* and *Crucidentacula kanayae* in Samples 138-845A-30X and -31X-2, 1 cm, indicates that these samples are equivalent to the *C. nicobarica* Zone. We did not observe diatoms in Sample 138-845A-31X-CC.

PALEOMAGNETISM

Procedures

The paleomagnetic procedures followed at Site 845 are outlined in the "Explanatory Notes" chapter (this volume), including (1) the measurement and demagnetization of split archive sections in the pass-through magnetometer, (2) the measurement and alternating-field (AF) demagnetization of discrete samples, and (3) susceptibility measurements. We measured all archive-half sections recovered at Site 845 with the pass-through magnetometer as follows:

Section	Treatment
138-845A-1H-1 through -4H-2 4H-3 through 10H-1 (-4H-4, 6H-4, -7H-7, 8H-4, 9H-4 also AFD 15 mT)	NRM and AFD, 15 mT NRM and AFD, 10 mT
10H-2 through 22H-7 -23X and -25X	NRM and AFD, 15 mT NRM and AFD, 15 mT
138-845B-1H-1 through -21H-7	NRM and AFD, 15 mT
138-845C-1H-1 through -3H-6	Only AFD, 15 mT

Hole 845C comprises three cores recovered from about 20 to 50 mbsf that were obtained to overlap missed zones at Holes 845A and 845B. Because previous measurements at Holes 845A and 845B indicated that the NRM data were highly overprinted, we did not measure the NRM at Hole 845C and demagnetized the sections directly at AF of 15 mT.

Results

The NRM at Site 845 clearly defined a dominant secondary remanence component having a consistent steep upward direction. Similar NRM directions were reported at Site 844 and during other ODP legs and have been linked to the APC coring barrels. Although the steep upward overprint was present in all cores at Site 845, much of it usually could be removed with 15 mT AF demagnetization. The NRM results of the pass-through magnetometer consistently showed inclinations steeper than 60°, while the 15-mT AF demagnetized data had significantly shallower inclinations. Results from demagnetization measurements of discrete samples (Table 6) compare well with data from the pass-through magnetometer, suggesting that a demagnetization of 15 mT of whole sections in the pass-through magnetometer is usually sufficient to isolate at least the polarity of the remanence. AF demagnetization of discrete samples often is successful at isolating the characteristic remanence (Fig. 27).

At Site 845, the upper 40 to 50 m of the sedimentary section showed weak, unstable remanence, from which no magnetostratigraphic interpretations were possible, at least from the ship pass-through magnetometer data. This result is in contrast with Site 844, where we obtained shipboard magnetostratigraphic interpretations only from the top 60 to 70 m. At Site 845, a sharp, four- to six-fold increase in magnetization intensity occurs near 50 mbsf, accompanied also by a two- to three-fold increase in susceptibility (Fig. 28). Below 50 mbsf, remanence is also more stable, which permitted consistent magnetostratigraphic interpretations for Holes 845A and 845B (Fig. 29 to 32). We note that the concentration of organic carbon in the top 50 m is 1% to 2%; below this level, an abrupt decrease in the organic carbon indicates scattered values to about 0.5%. Further studies might

Table 6. Analysis of principal components of discrete samples from Hole 845A.

Sample, interval (cm)	N	MAD	Declination (degrees)	Inclination (degrees)
1H-3, 128-130	6	1.9	16.8	15.5
1H-5, 45-47	4	2.7	10.3	20.6
4H-4, 87-89	3	9.3	250.3	-33.0
11H-5, 126-128	3	2.7	314.1	16.2
12H-3, 83-85	3	1.8	47.3	12.1
8H-4, 50-52	3	.9	44.8	12.5
7H-4, 90-92	7	3.3	105.2	-5.1
9H-4, 90-92	2	6.2	239.4	-13.9
10H-4, 80-82	4	.9	277.1	1.8
21H-6, 24-26	4	7.5	314.8	-19.2
22H-2, 24-26	3	3.4	12.1	-22.3
27X-1, 137-139	4	3.2	358.6	-8.7
23X-3, 71-73	3	1.9	324.7	-57.6
23X-6, 65-67	6	5.2	332.6	-38.7
11H-1, 136-138	4	2.4	296.7	1.3

N = No. of demagnetization points used in the principal component analysis; MAD = mean angular deviation. Principal component fits are in all cases anchored to the origin. Declinations are measured with respect to the double fiducial lines on the core liner (work halves).

determine whether this enrichment in organic carbon in the upper 50 m is sufficient to cause dissolution of magnetic minerals and to account for the lower magnetization intensity.

Declination, which embodies most of the angular change of reversals at low latitudes, was the primary parameter for identifying magnetic polarity boundaries. Because of the relatively shallow dipole inclination expected at the Site 845 latitude ($I \sim 18^\circ$) and because the drilling overprint often is not entirely removed by 15-mT AF demagnetization with the pass-through magnetometer, the inclination record was secondary when selecting polarity boundaries. When multishot orientation was absent or suspect in Hole 845B (Table 7), we determined polarity by correlation with the Hole 845A results or by reference to the inclination record, where this proved clear. Good correspondence of magnetic polarity exists between Holes 845A and 845B when they are placed in a composite depth section (Fig. 33).

The polarity zonation so obtained can be readily correlated with the magnetic polarity time scale (Table 8) in a manner consistent with biostratigraphic constraints (see "Biostratigraphy" section, this chapter). The youngest reversal boundary identified was at about 50 mcd in Hole 845A, and, considering the biostratigraphic results, this boundary correlates with the termination of the Kaena reverse subchron in the Gauss at 2.92 Ma. Magnetostratigraphic interpretation is generally straightforward below this, through the APC-cored portion of the section. The only significant gap in the record occurs in Hole 845B between 165 and 197 mcd, where, because of low-quality pass-through results, we did not interpret a polarity record for Core 138-845B-18H and parts of Cores 138-845B-16H and -17H. This gap in the record leads to some difficulty when correlating the recovered polarity zones to Chron C5A; however, these problems should be more easily resolved after further shore-based study of this interval.

In summary, consistent magnetostratigraphy was obtained at Site 845 below 50 mbsf down to about 200 mbsf, spanning about 10 m.y. from the middle Miocene (13.4 Ma) to the middle Pliocene (~2.7 Ma). This site may provide a high-resolution polarity record for the middle Miocene and exhibits three short, normal polarity features of the late Miocene (in Chrons C3A, C4, and C4A) that were not recognized by currently accepted magnetic polarity timescales.

SEDIMENTATION RATES

A sedimentary section almost 300 m thick that covers the time interval from the late Pleistocene to the early Miocene was recovered at Site 845. Biostratigraphic age control was provided by all four of

Table 7. Orientation corrections for Site 845 cores.

Core	Azimuthal orientation (0°–360°)	Deviation from direction (0°–360°)	Vertical drift (°)
^a 138-845A-1H			
^a 2H			
^a 3H			
4H	234	010	0.9
5H	053	016	0.9
6H	076	004	1.2
7H	019	024	0.8
8H	283	037	1.0
9H	287	038	1.1
10H	279	036	1.1
11H	046	027	0.5
12H	304	047	1.0
13H	044	046	0.8
14H	358	042	1.0
15H	145	024	0.2
16H	210	027	1.0
17H	190	010	1.0
18H	300	037	1.1
19H	260	056	1.2
20H	335	076	0.8
21H	015	068	1.0
22H	125	038	1.0
^a 138-845B-1H			
^a 2H			
^a 3H			
4H	065	148	4.3
5H	352	149	4.5
6H	255	148	4.0
7H	288	145	4.1
8H	(195)	150	3.5
^a 8H	130		
9H	015	147	3.9
10H	(344)	150	3.4
^a 10H	120		
11H	007	147	3.3
12H	(300)	150	2.9
^a 12H	220		
13H	309	142	3.0
14H	(87)	152	3.0
^a 14H	30		
15H	345	145	2.9
16H	320	143	2.6
17H	(335)	152	2.5
^a 17H	220		
18H	017	147	2.7
19H	287	147	2.5
20H	233	151	2.5
21H	357	140	2.7
^a 138-845C-1H			
2H	043	181	1.0
3H	302	324	0.2

^aSecondary orientation (SOR) angle is the value used to adjust average measured declination to 0° or 180° for normal and reversed chronozones, respectively, when multishot orientation is not available or inconsistent. Multishot azimuth values in parentheses are considered to be erroneous, and in our interpretation we used the SOR value in the following line.

For multishot orientation, the measured declination was corrected by adding to it the multishot azimuthal orientation and the local geomagnetic deviation (6.4°).

the chief planktonic microfossil groups. In addition, an excellent continuous paleomagnetic record was obtained from the early Pliocene to the middle Miocene. We were able to develop a complete composite of the 207-m section that was recovered with the APC by making use of GRAPE, magnetic susceptibility, and color scanner records.

The composite depth section for Site 845 is presented in Table 9. This composite was formed by comparing shipboard measurements of GRAPE, magnetic susceptibility, and percentage of reflectance at adjacent holes. These comparisons then were integrated to form a

single composite-depth section for that site (a detailed discussion about the construction of composite sections during Leg 138 is presented in Hagelberg et al., this volume).

For the holes and cores listed in Column 1 of Table 9, Column 2 presents the ODP sub-bottom depth of the interval (in mbsf). Note that the depth in Column 2 gives the depth to the bottom of the recovered cores. This depth is necessary for placing the core-catcher samples in their correct position in the composite depth section and is not the same as the standard ODP core-catcher depth. Column 3 shows the length of core recovered. Column 4 gives the composite depth of the interval (in mcd). Column 5 indicates the amount of offset between the ODP depth and the composite depth. For each core, conversion from ODP sub-bottom depth (mbsf) of any sample to composite depth (mcd) was performed by adding the offset listed in Column 5 for that core.

Magnetic susceptibility, GRAPE density, and percentage of reflectance data all produced high-amplitude records through Holes 845A, 845B, and 845C. The formation of the composite section made use of all three records (which are displayed in back-pocket Fig. 34). Although magnetic susceptibility was the primary guide for hole-to-hole correlation over the first 25 m of the composite depth section, a satisfactory composite section was achieved only after integrating all three records. The final composite displays satisfactory agreements among all three variables.

Analysis of the composite depth section shows that from the cored intervals in Holes 845A, 845B, and 845C, we recovered a continuous section down to 224 mcd. Although Core 138-845B-3H does not correlate well with the equivalent part of Hole 845A (this core may have been disturbed), the offset Cores 138-845C-1H and -2H combine to give a continuous record through this interval (Fig. 34). Cores from Holes 845A and 845B in the remainder of the section continue to overlap one another. The composite depths of the magnetic reversal boundaries (see "Paleomagnetism" section, this chapter) in Holes 845A and 845B appear to be consistent in most cases. The few apparent inconsistencies will be investigated during shore-based studies. In particular, we had difficulty reconciling the magnetic record of Core 138-845B-18H with those of -845A-18H and -19H (see "Paleomagnetism" section, this chapter); however, the composite section indicates good overlapping intervals.

To obtain good estimates of sedimentation rate, we used the paleomagnetic record for age control, except in the upper part, where radiolarian datums were used, and in the lower part, where both a radiolarian and a nannofossil datum were used. All control points are listed in Table 10. In the upper part of the APC section, where no paleomagnetic record was recovered and where calcareous nannofossils of poor preservation were found, the extinction datums of *Stylactis univertus* and *Pterocanium prismatium* provide control points at 0.41 and 1.61 Ma (see "Biostratigraphy" section, this chapter). In the lower part, where XCB recovery did not provide suitable material for shipboard paleomagnetic stratigraphy, we used the extinction of *Helicosphaera ampliaperta* (16.0 Ma). In addition to this datum, which was located about 50 m above the base of the recovered section, we used diatom data from the bottom of the site. *Crucidentacula kanayaae* (FAD, 16.9 Ma) is present in Sample 138-845A-30X-CC, but *Cestodiscus peplum* (FAD, 16.4 Ma) first appears in Sample 138-845A-29X-CC. This diatom datum may be the most reliable means of obtaining a mean sedimentation rate for the lowest part of the section and for estimating the age of the base of the section because only 10 m of section separates the mean position of these two datums and the base of the recovered section. This method implies that the basement age is about 16.5 Ma.

Ambiguity in the interpretation of the shipboard magnetic record does occur between C5-n2 (o) at about 166 mcd and C5A-n1 at about 183 mcd. The simplest interpretations are either that (1) the transition at about 174 mcd marks C5-n3 (t) or (2) it represents C5A-n1 (t). The second interpretation would require that the lowest sedimentation rate recorded at Site 845 be about 8 m/m.y. between 10.5 and 11 Ma (the

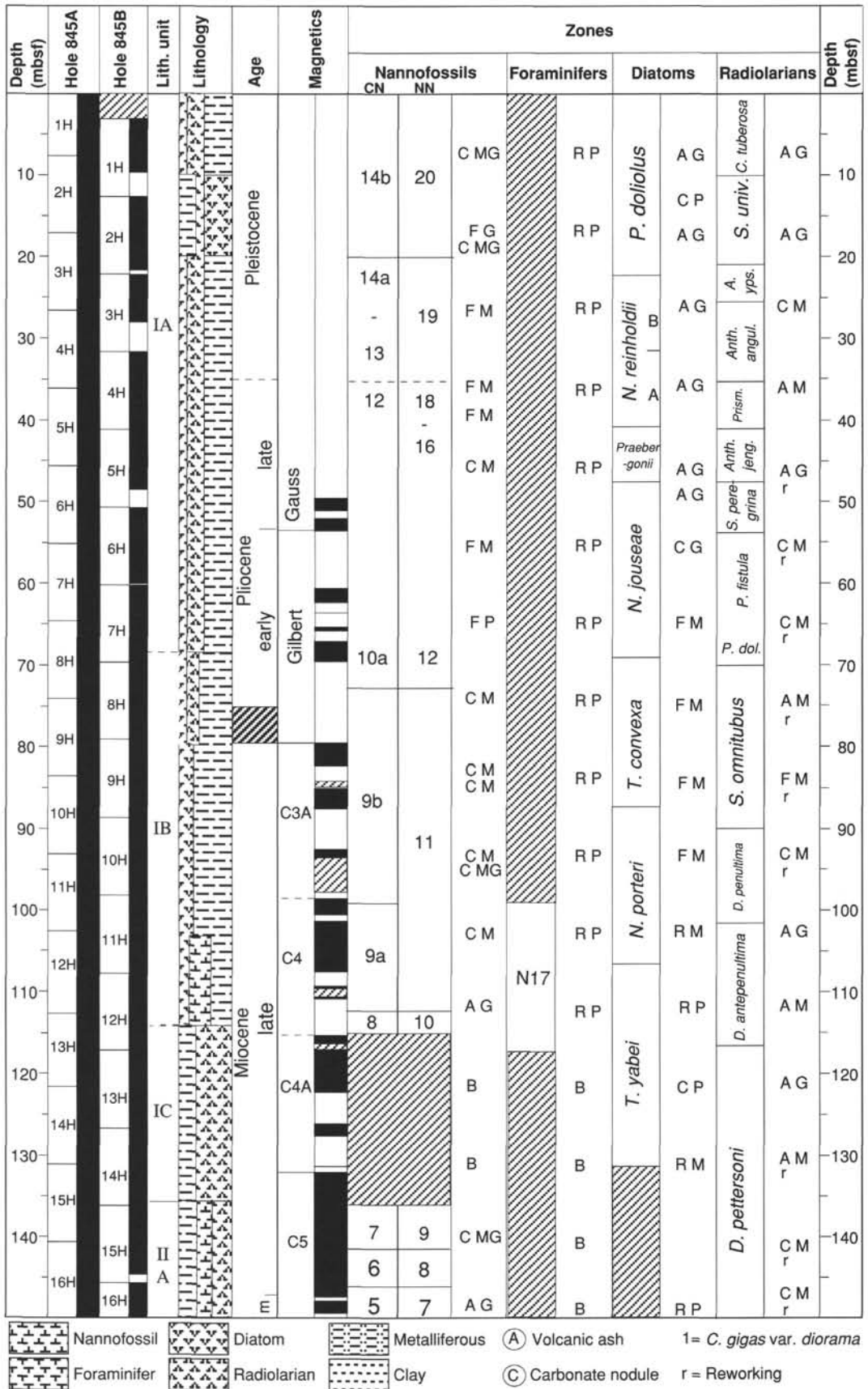


Figure 26. Stratigraphic summary for Site 845. Depth is in meters below seafloor (mbsf). Diatom Zone 1 = *Coscinodiscus gigas* var. *diorama*. Microfossil abundance is recorded as A = abundant; C = Common; F = few; R = rare; B = barren. Microfossil preservation is recorded as G = good; M = moderate; P = poor. An "r" indicates the presence of older, reworked microfossils. This is a general overview only of the stratigraphic results at Site 845. Placement of specific stratigraphic boundaries may differ slightly between Holes 845A and 845B. Data presented in this figure are based on results from Holes 845A and 845B.

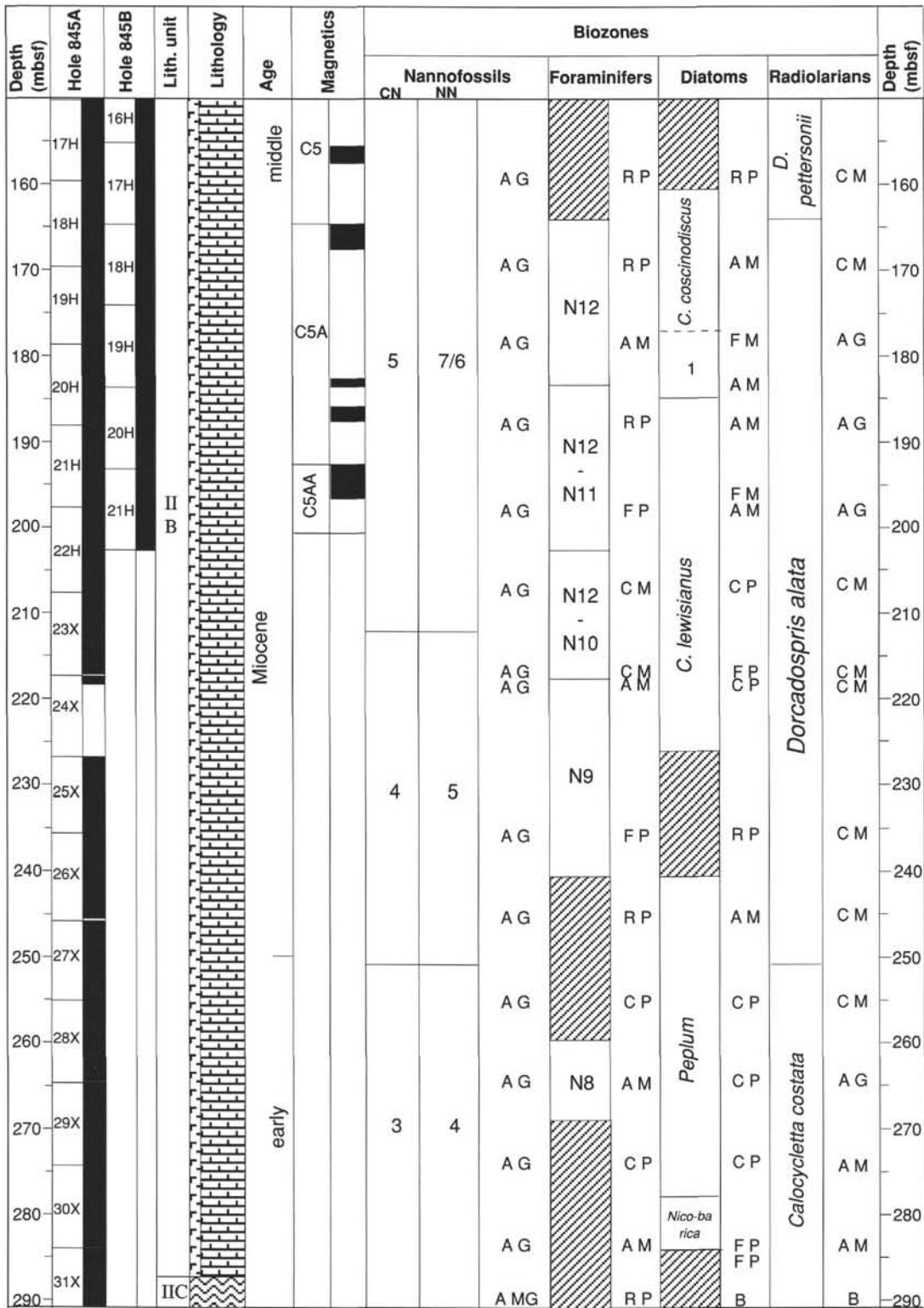


Figure 26 (continued).

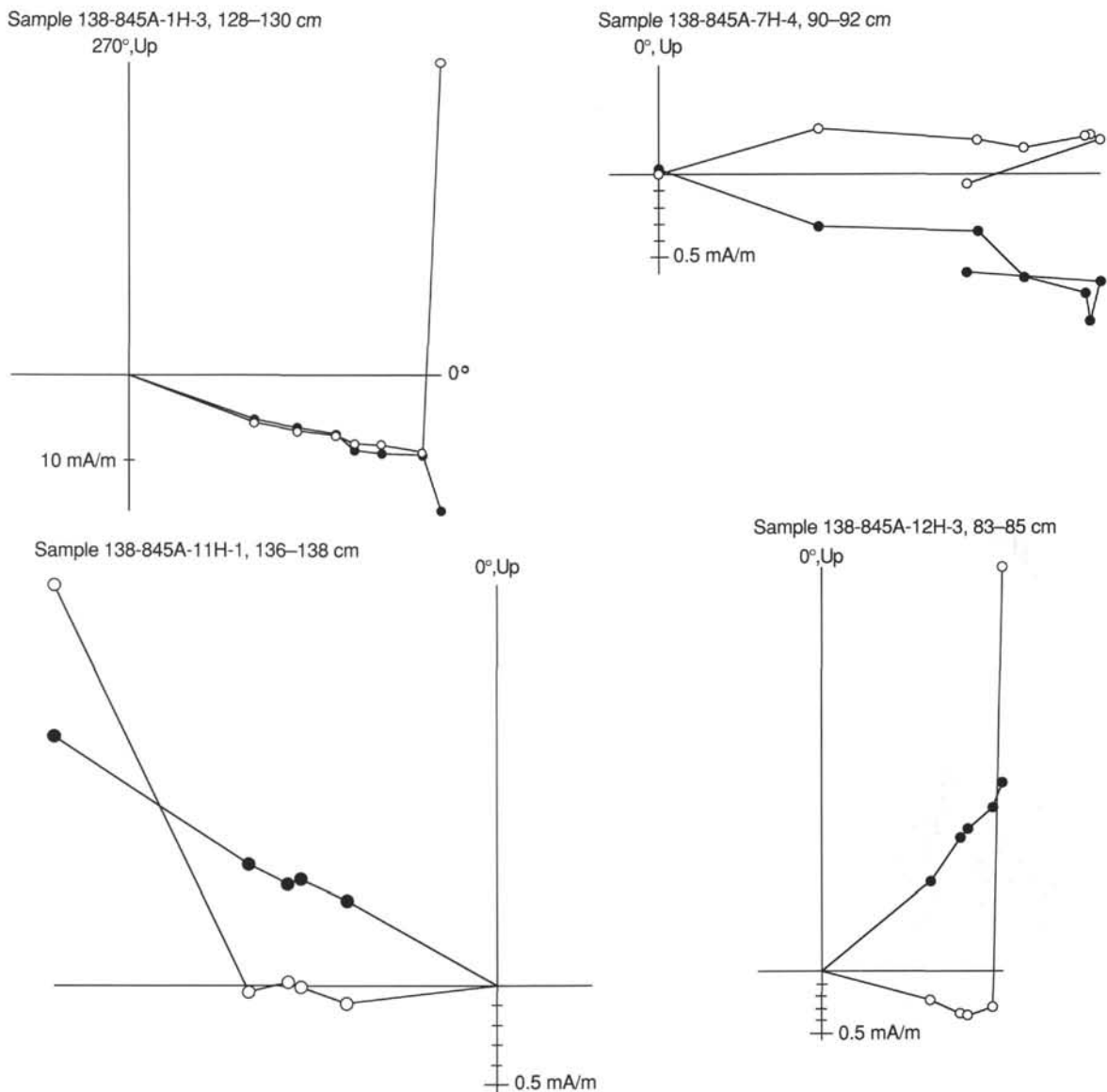


Figure 27. Vector projection demagnetization diagrams, showing the pervasive vertical upward overprint encountered in samples from Site 845. Open circles denote projection onto horizontal (vertical) plane. Azimuthal orientation is with respect to the double fiducial line.

section from 150 to 183 mcd). In contrast, the first interpretation (as depicted in Fig. 35) shows the sedimentation rate at its lowest during C5-n1 and increasing rapidly below that. We favor this interpretation because carbonate content is low in the sediments recording C5-n1 and increases rapidly below that level to reach about 60% by 170 mcd (see "Organic Geochemistry" section, this chapter).

Figure 35 shows an age-vs.-depth plot for Site 845. To avoid introducing noise into the plot of sedimentation rate, we selected the paleomagnetic datums to provide controls about 0.5 m.y. apart. We examined the complete array of datums to ensure that any reversal appearing to constrain the timing of a change in sedimentation rate was included. Figure 36 is a plot of sedimentation rate vs. age, and Figure 37 is a plot of sedimentation rate vs. depth in the section (mcd). Rates are about 30 m/m.y. in the upper/middle Pleistocene, decreasing to 20 m/m.y. in the lower Pleistocene and to about 12 m/m.y. in the Pliocene. During the late Miocene, sedimentation rates varied between 13 and 20 m/m.y., but reached another minimum over the interval 8.9 to 10.5 Ma. Below this point, the rate rose to a maximum of almost 30 m/m.y. at 12.5 Ma. In the lower part of the middle

Miocene (between 13.2 and 16 Ma), the rate was lower, although one must recognize that the time control is less reliable in the absence of paleomagnetic control below 226 m (13.2 Ma).

INORGANIC GEOCHEMISTRY

Fifteen interstitial-water samples were collected at Site 845: three from Hole 845C at depths ranging from 21.5 to 38.9 mbsf and 12 from Hole 845A at depths ranging from 51.6 mbsf to basement at 291.4 mbsf (Table 11). Here, results from these two holes are considered as constituting a single depth profile. The three interstitial-water samples from Hole 845C were taken from the variably calcareous Pleistocene/Pliocene sediment composing Subunit IA (see "Lithostratigraphy" section, this chapter). Sampling of interstitial water in Hole 845A began with a sample from this same subunit (Sample 138-845A-6H-4). The next two intervals, Samples 138-845A-9H-4 and -12H-4, were taken in Subunit IB, while Sample 138-845A-15H-4 was taken at the top of lithologic Subunit IIA, between two bands of clay and/or oxide-rich interbeds (see "Lithostratigraphy" section, this chapter).

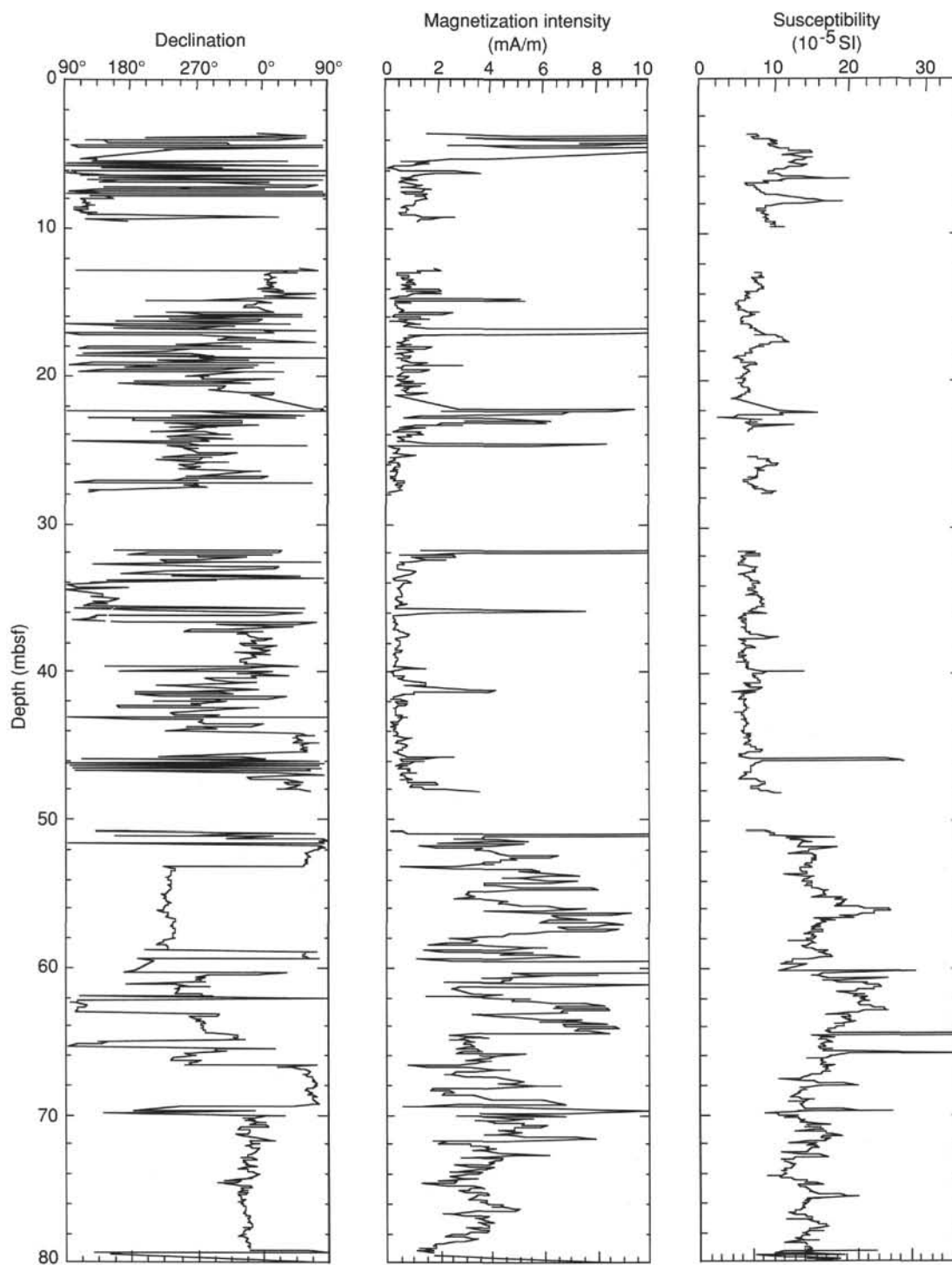


Figure 28. Profiles of declination, magnetization intensity, and magnetic susceptibility down the core for the upper 80 m in Hole 845B, showing the transition at 50 mbsf, below which intensity increases and directions become stable.

Sections 138-845A-18H-4 through -30X-2 were extracted from sediments of Subunit IIB and ranged in age from the middle to early Miocene (16.5 Ma). The deepest sample (138-845A-31X-5) was squeezed from the metalliferous sediments of Subunit IIC, lying immediately above basement rocks, chips of which were collected in the core-catcher sample of this core.

Chemical gradients at this site are subtle (Table 11) and are governed by the biogenic-rich, organic-carbon-poor character of the sediments and by the diffusive influence of basalt alteration

reactions at depth. Several indicators, however, would suggest that the interstitial waters at this site are somewhat more reducing than at Site 844.

Sodium (Fig. 38A), as calculated by charge balance, displays only small fluctuations with depth. No discernable trends are present in the distribution of interstitial sodium down the core, except for one sample minimum at 194.1 mbsf.

As with sodium, chloride at this site (Fig. 38B) does not vary (558 ± 3 mM) within our ability to measure it (0.4% error), especially if

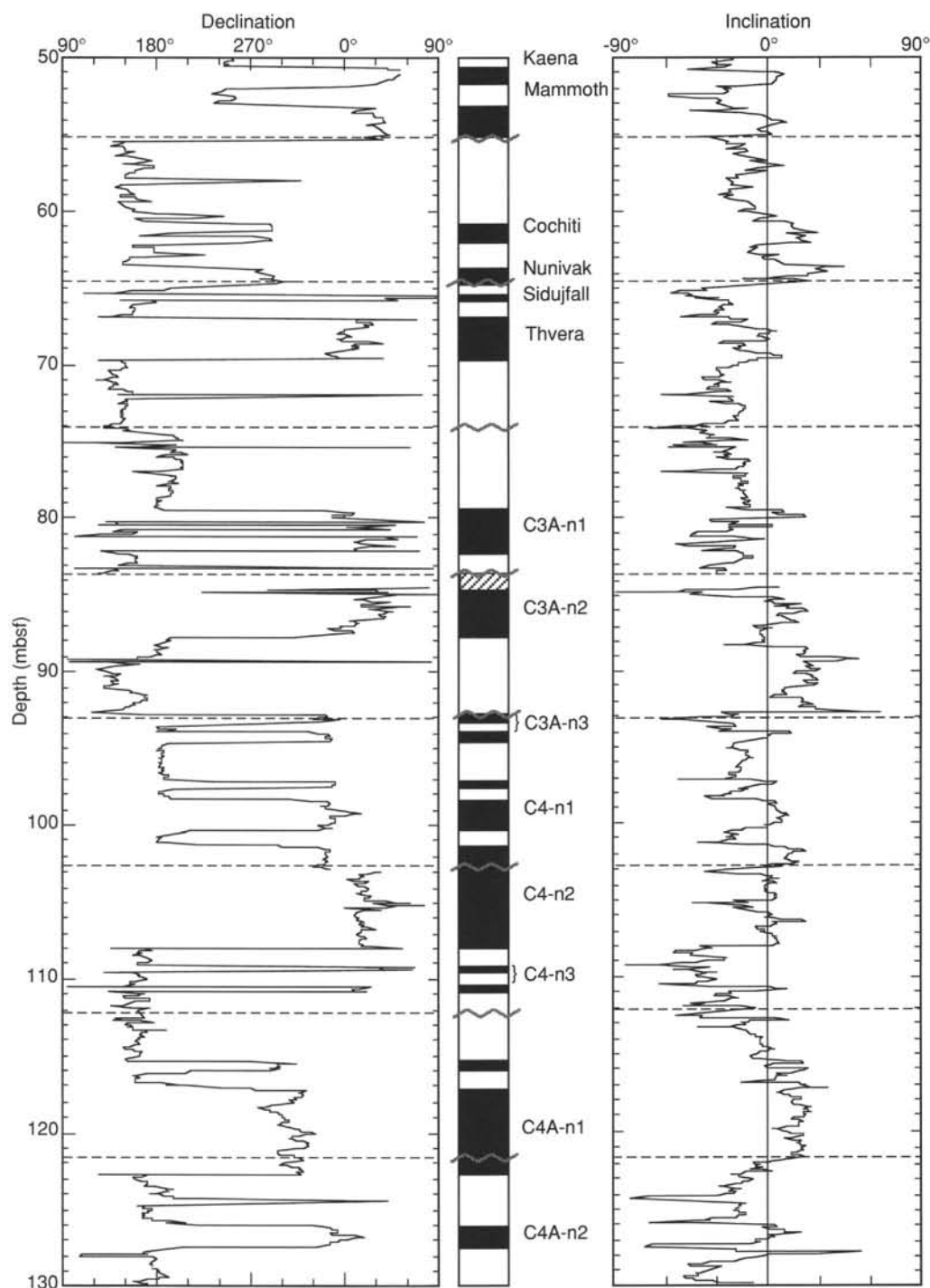


Figure 29. Declination and inclination profiles from the pass-through magnetometer, demagnetized at 15 mT, and identification of polarity chronozones found from 50 to 130 mbsf in Hole 845A. Black = normal, white = reverse, hatched = no data or no interpretation. Declinations have been rotated as described in Table 7. Dashed lines indicate location of core boundaries.

one ignores the one anomalously low sample from 194.1 mbsf (Sample 138-845A-21X-4). The low values of sodium and chloride at 194.1 mbsf (Table 11) coincide approximately with the depth of a dramatic change in sound velocity at 210 mbsf (see "Downhole Measurements" section, this chapter) that can be interpreted as the onset of lithification.

Alkalinity at this site (Fig. 38C) is significantly higher through most of the sediment column than standard seawater (2.45 mM) from Interna-

tional Association of Physical Sciences Organizations (IAPSO). These relatively high alkalinities suggest that the interstitial waters from this site are more reducing and corrosive than at Site 844. This inference is supported by lower pH values (Table 11) and is consistent with the generally higher organic carbon contents of these sediments (see "Organic Geochemistry" section, this chapter) when compared to those at Site 844. This is not to say that the interstitial waters from this site are reductive in the extreme. Alkalinities in truly reducing

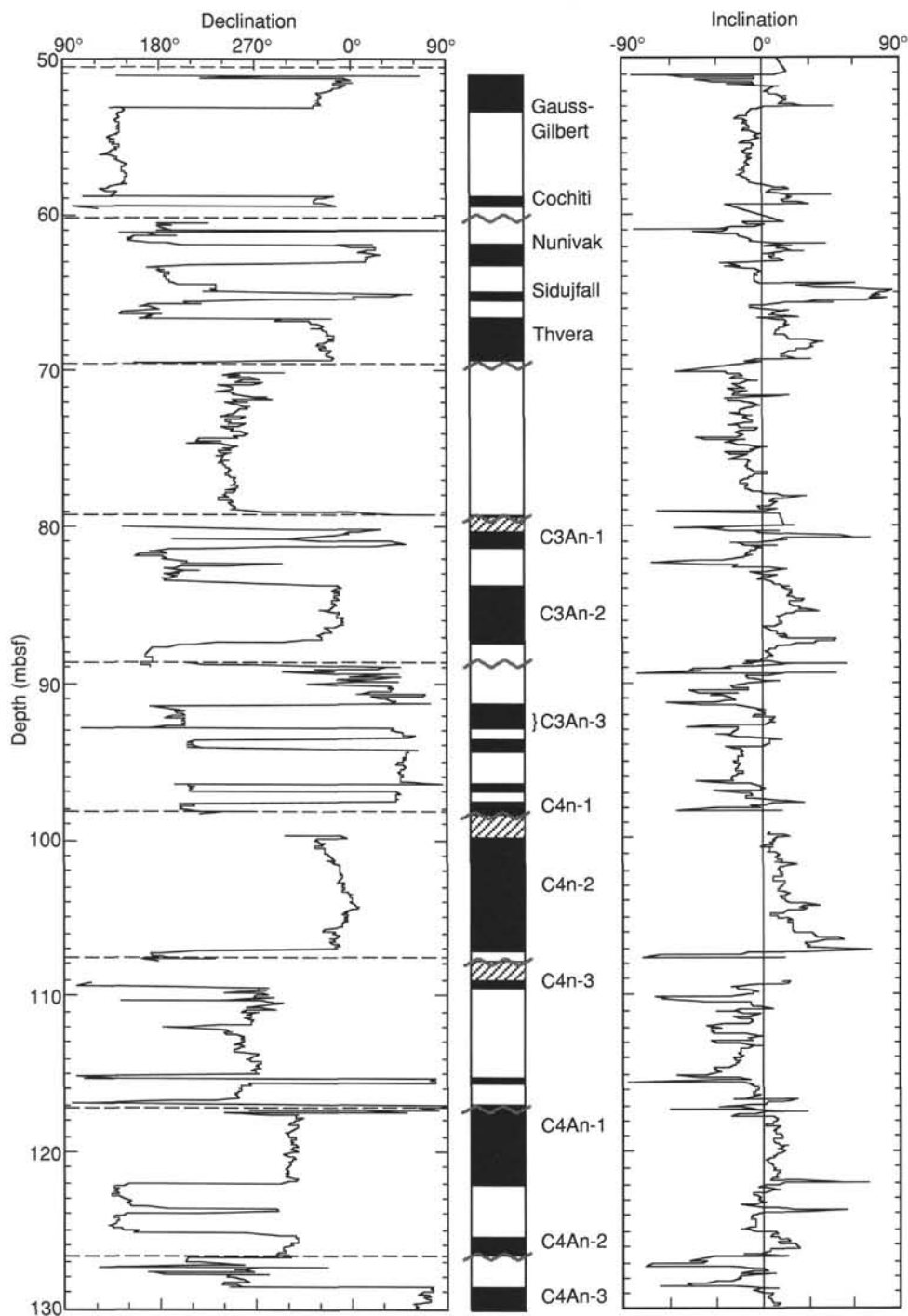


Figure 30. Declination and inclination profiles from the pass-through magnetometer, demagnetized at 15 mT, and identification of polarity chronozones found from 50 to 130 mbsf in Hole 845B. Black = normal, white = reverse, hatched = no data or no interpretation. Declinations have been rotated as described in Table 7. Dashed lines indicate location of core boundaries.

sediments (i.e., 0 sulfate), such as those sampled by Harrison et al. (1982) at Sites 496 and 497 on the Mid America Trench slope during DSDP Leg 67, can reach concentrations that are 20 times the levels found at this site.

The profile of sulfate with depth (Fig. 38D) is consistent with mild anoxia. Sulfate decreases steadily down to 250 mbsf at Site 844, with an absolute change of 5% over 300 m. The total change in sulfate at

this site (Fig. 38D) is approximately the same, but this decrease occurs abruptly between 24.5 and 38.9 mbsf. The position of this change suggests that recent depositional trends at Site 845 fostered mildly reducing conditions.

Ammonia data (Fig. 39C) also indicate that the interstitial waters here are more reducing than those at Site 844. Ammonia levels at Site 844 were below the detection limit (<10 mM). At this site, ammonia

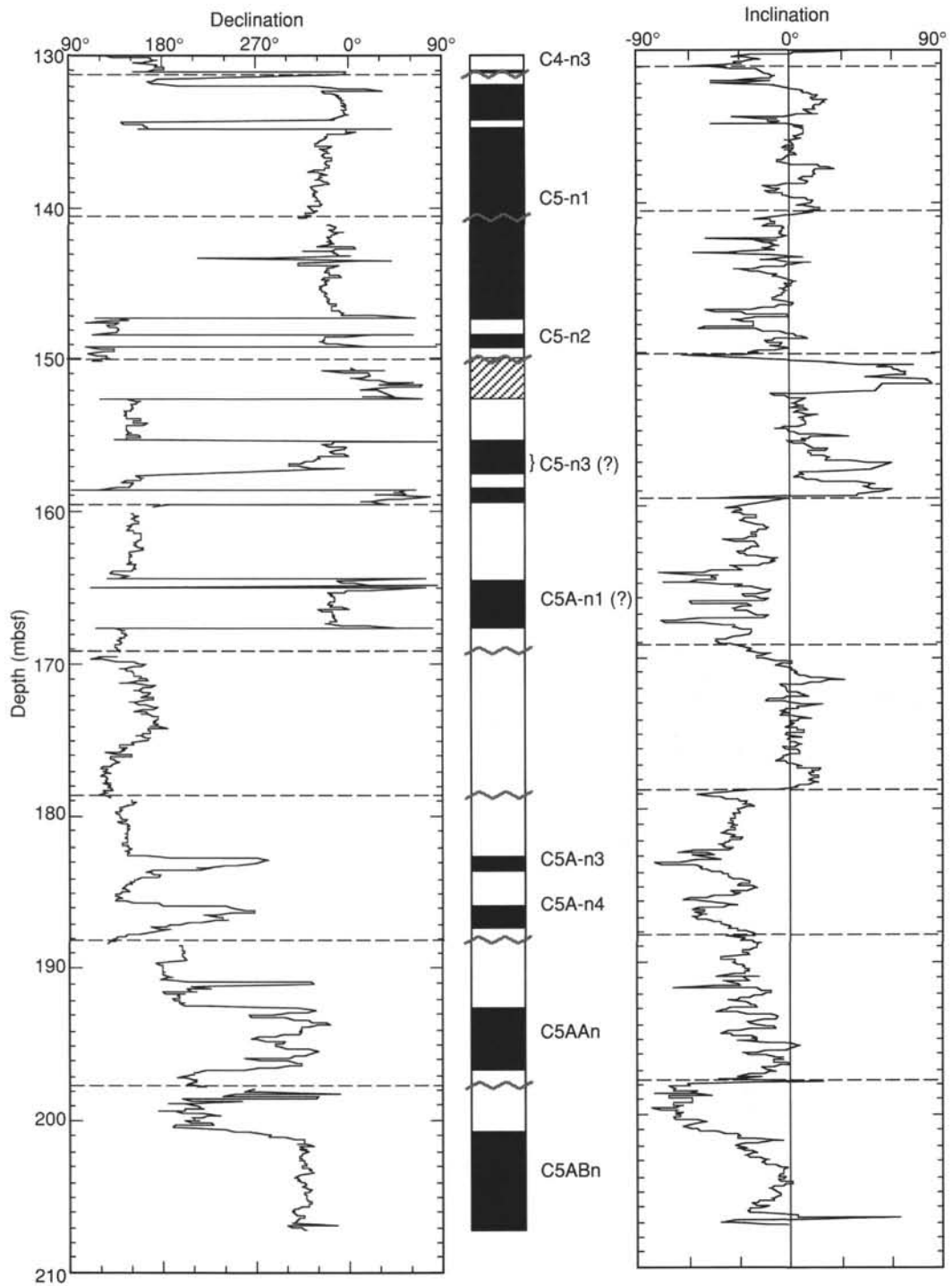


Figure 31. Declination and inclination profiles from the pass-through magnetometer, demagnetized at 15 mT, and identification of polarity chronozones found from 130 to 208 mbsf in Hole 845A. Black = normal, white = reverse, hatched = no data or no interpretation. Declinations have been rotated as described in Table 7. Dashed lines indicate location of core boundaries.

levels reach 150 mM (Table 11) and are highest in at the top sections, coinciding with the highest alkalinities and steepest gradient in sulfate.

A section of sediment centered at 50 mbsf is characterized by a minimum value of sulfate (Fig. 38D) and maximum value of ammonia (Fig. 39C), indicating a relatively high reductive intensity at this level. This horizon also is punctuated by a decrease in organic carbon (see “Organic Geochemistry” section, this chapter) and an abrupt, two-

fold increase in magnetic susceptibility (see “Paleomagnetism” section, this chapter).

The total range in interstitial magnesium concentrations downhole at this site (excluding the bottom sample) is about 4% (Table 11), which is eight-fold larger than the precision of the titration technique used to measure them (0.5%). Nevertheless, one has trouble identifying a discernable trend in this profile.

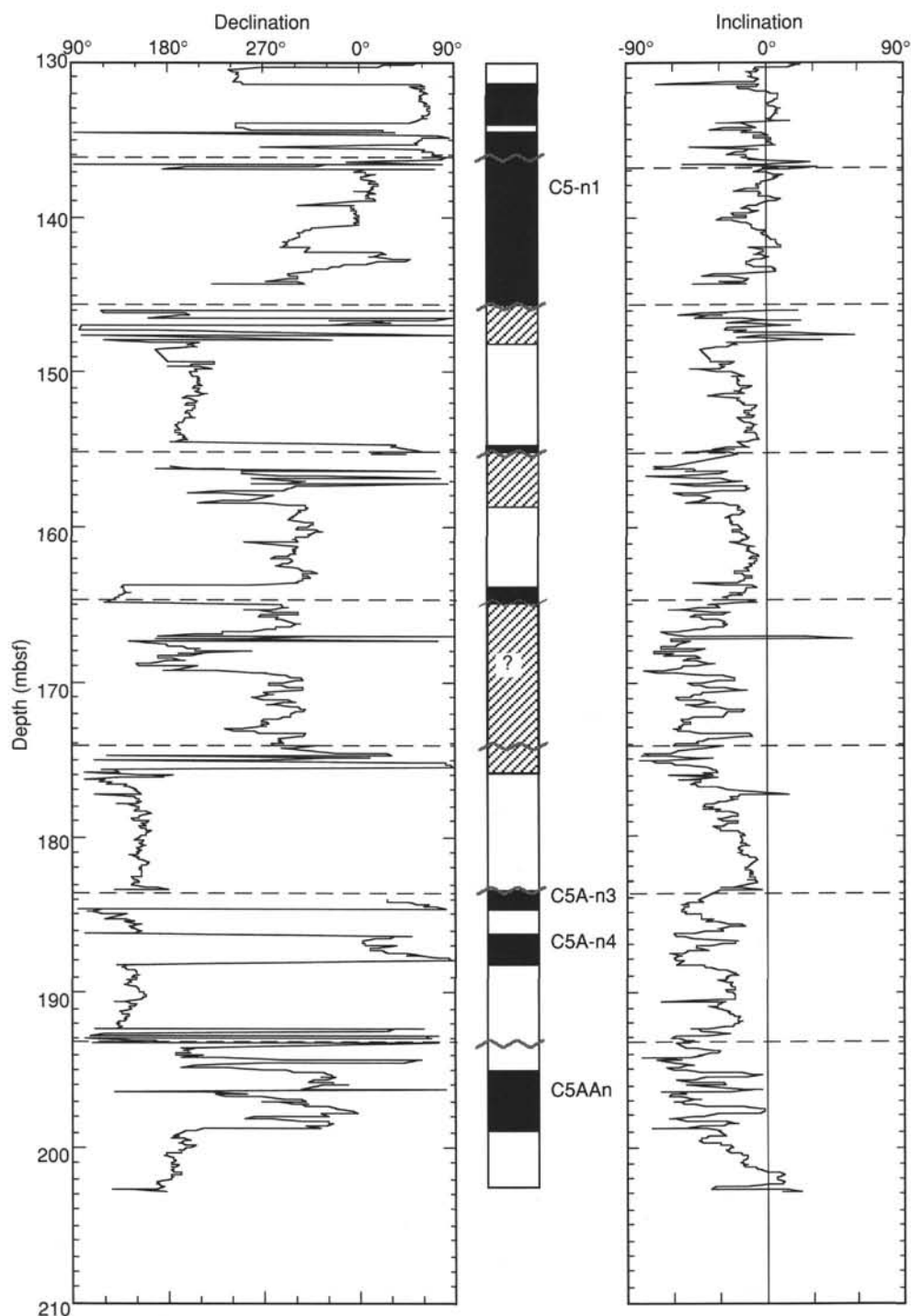


Figure 32. Declination and inclination profiles from the pass-through magnetometer, demagnetized at 15 mT, and identification of polarity chronozones found from 130 to 203 mbsf in Hole 845B. Black = normal, white = reverse, hatched = no data or no interpretation. Declinations have been rotated as described in Table 7. Dashed lines indicate location of core boundaries.

Much like the situation at Site 844, a small, but statistically significant, decrease in potassium can be seen (Fig. 40C) down the core. The total top-to-bottom variation in potassium amounts to a relative change of $\sim 14\%$, which is five-fold larger than the precision of the measurement.

Downhole changes in calcium at Site 845 (Fig. 40B) are extremely small. The difference between concentrations near the sediment/water

interface (10.60 mM) and those in Sample 138-845A-30X-2 from 277.2 mbsf is 0.42 mM, less than the change at Site 844. Still, a small increase in calcium below 80.1 mbsf does seem to be apparent (Sample 138-845A-9H-4). This observation is consistent with ongoing recrystallization. This interpretation is supported by both the silica (Fig. 40D) and strontium profiles (Fig. 39B), which exhibit broad maxima in the middle Miocene sections of the hole.

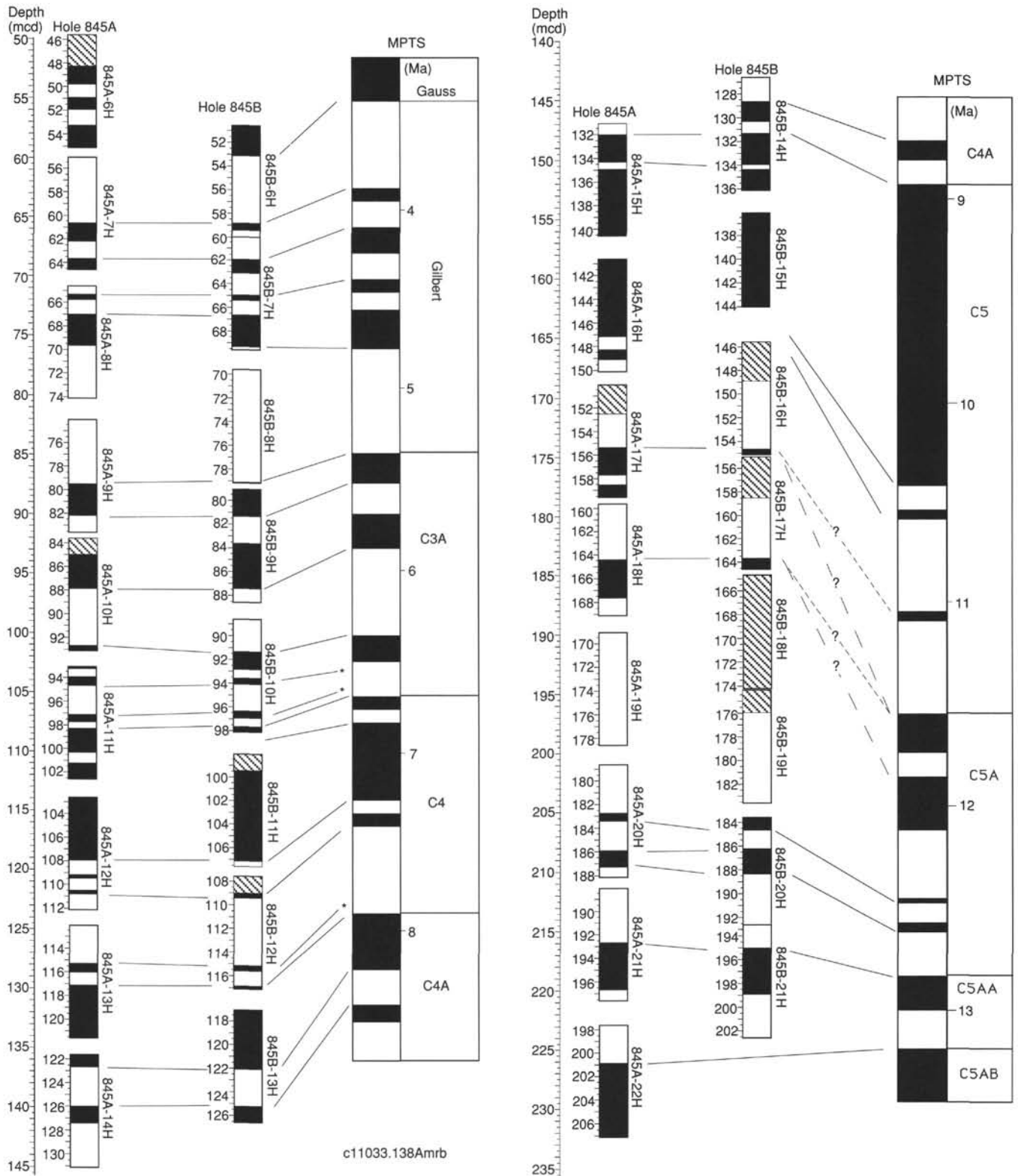


Figure 33. Magnetostratigraphic synthesis. Depth ticks for individual cores are in meters below sea floor (mbsf). Cores are located at appropriate meters composite depth (mcd). Black zones indicate normal polarity; white zones indicate reverse polarity; hatched lines are zones where no interpretation was made. Asterisk denotes correlation to short normal polarity subchrons not included in the time scale. Dashed lines reflect alternative interpretations for the correlation with Chron C5A.

Table 8. Reversal boundary depths from Site 845.

Interval (cm)	Depth (mbsf)	Depth (mcd)	Interpreted polarity boundary	Age (Ma)	Comments
138-845A-6H-3, 120	49.80	53.88	Kaena (t)	2.92	
6H-4, 80	50.90	54.98	Kaena (o)	2.99	
6H-5, 30	51.90	55.98	Mammoth (t)	3.08	
6H-6, 20	53.30	57.38	Mammoth (o)	3.18	
7H-4, 110	60.70	65.56	Cochiti (t)	3.88	
7H-5, 110	62.20	67.06	Cochiti (o)	3.97	
7H-6, 100	63.60	68.46	Nunivak (t)	4.10	
8H-1, 70	65.30	71.60	Sijdufjall (t)	4.40	
8H-1, 115	65.75	72.05	Sijdufjall (o)	4.47	
8H-2, 90	67.00	73.30	Thvera (t)	4.57	
8H-4, 60	69.70	76.00	Thvera (o)	4.77	
9H-4, 90	79.50	87.51	C3A-n1 (t)	5.35	
9H-6, 60	82.20	90.21	C3A-n1 (o)	5.53	
10H-1, 140	85.00	93.48	C3A-n2 (t)	5.68	
10H-3, 120	87.80	96.28	C3A-n2 (o)	5.89	
10H-7, 10	92.70	101.18	C3A-n3 (t)	6.37	
11H-1, 20	93.30	103.06	C3A-n3 (o)(?)	6.50	
11H-1, 85	93.95	103.71	N -> R		
11H-2, 10	94.70	104.46	C3A-n3 (o)(?)	6.50	
11H-3, 100	97.10	106.86	C4-n1 (t)(?)		
11H-4, 10	97.70	107.46	R -> N		
11H-4, 70	98.30	108.06	C4-n1 (t)(?)	6.70	
11H-5, 125	100.35	110.11	C4-n1 (o)	6.78	
11H-6, 65	101.25	111.01	C4-n2 (t)	6.85	
12H-4, 85	107.95	119.28	C4-n2 (o)	7.28	
12H-5, 60	109.20	120.53	C4-n3 (t)(?)	7.35	
12H-5, 90	109.50	120.83	C4-n3 (o)(?)	7.41	
12H-6, 40	110.50	121.83	C4-n3 (t)(?)	7.35	
12H-6, 70	110.80	122.13	C4-n3 (o)(?)	7.41	
13H-3, 25	115.35	127.96	C4A-n1 (t)(?)	7.90	
13H-3, 95	116.05	128.66	C4A-n1 (o)(?)	8.21	
13H-4, 50	117.10	129.71	C4A-n1 (t)(?)	7.90	
14H-1, 110	122.70	136.68	C4A-n1 (o) ?	8.21	
14H-3, 140	126.00	139.98	C4A-n2 (t)	8.41	
14H-4, 135	127.45	141.43	C4A-n2 (o)	8.50	
14H-7, 50	131.10	145.08	C4A-n3 (t)	8.71	
15H-1, 90	132.00	147.86	C5-n1 (t)	8.92	
15H-3, 25	134.35	150.21	R -> N		
15H-3, 80	134.90	150.76	N -> R		
16H-5, 60	147.20	164.93	C5-n1 (o)	10.42	
16H-6, 25	148.35	166.08	C5-n2 (t)	10.54	
16H-6, 100	149.10	166.83	C5-n2 (o)	10.59	
17H-4, 80	155.40	174.21	C5-n3 or C5A-n1 (t)	11.03, 11.55	
17H-6, 10	157.70	176.51	R -> N ?		Poorly defined
17H-6, 90	158.50	177.31	N -> R ?		Poorly defined
17H-7, 40	159.50	178.31	C5-n3 or C5A-n1 (o)(?)	11.09, 11.73	Very poorly defined
18H-4, 35	164.45	183.73	C5A-n1 or -n2 (t)(?)	11.55, 11.86	
18H-6, 55	167.65	186.93	C5A-n1 or -n2 (o)(?)	11.73, 12.12	
20H-3, 115	182.75	205.08	C5A-n3 (t)	12.46	
20H-4, 35	183.45	205.78	C5A-n3 (o)	12.49	Poorly defined
20H-5, 130	185.90	208.23	C5A-n4 (t)	12.58	
20H-6, 115	187.25	209.58	C5A-n4 (o)	12.62	Poorly defined
21H-4, 10	192.70	215.93	C5AA-n (t)	12.83	
21H-6, 105	196.65	219.88	C5AA-n (o)	13.01	
22H-3, 25	200.85	226.08	C5AB-n (t)	13.20	
138-845B-06H-2, 105	53.15	59.88	Gauss/Gilbert	3.40	
06H-6, 070	58.80	65.53	Cochiti (t)	3.88	
06H-6, 135	59.45	66.18	Cochiti (o)	3.97	
07H-2, 035	61.95	68.56	Nunivak (t)	4.10	
07H-3, 005	63.15	69.76	Nunivak (o)	4.24	
07H-4, 035	64.95	71.56	Sidufjall (t)	4.40	
07H-4, 085	65.45	72.06	Sidufjall (o)	4.47	
07H-5, 055	66.65	73.26	Thvera (t)	4.57	
07H-7, 025	69.35	75.96	Thvera (o)	4.77	
08H-7, 050	79.10	87.48	C3A-n1 (t)	5.35	
09H-2, 075	81.35	90.21	C3A-n1 (o)	5.53	
09H-4, 005	83.65	92.51	C3A-n2 (t)	5.68	
09H-6, 085	87.45	96.31	C3A-n2 (o)	5.89	
10H-2, 125	91.35	101.68	C3A-n3 (t)	6.37	
10H-3, 125	92.85	103.18	C3A-n3 (o)(?)	6.50	
10H-4, 050	93.60	103.93	N -> R		
10H-4, 105	94.15	104.48	C3A-n3 (o)(?)	6.50	
10H-6, 030	96.40	106.73	C4-n1 (t)	6.70	
10H-6, 085	96.95	107.28	C4-n1 (o)	6.78	
10H-7, 005	97.65	107.98	C4-n2 (t)	6.85	

Table 8 (continued).

Interval (cm)	Depth (mbsf)	Depth (mcd)	Interpreted polarity boundary	Age (Ma)	Comments
11H-7, 010	107.20	119.31	C4-n2 (o)	7.28	
12H-2, 035	109.45	121.56	C4-n3 (o)	7.41	
12H-6, 010	115.20	127.31	C4A-n1 (t)(?)	7.90	
12H-6, 050	115.60	127.71	R -> N		
12H-7, 020	116.80	128.91	C4A-n1 (t)(?)	7.90	
13H-4, 045	122.05	136.81	C4A-n1 (o)	8.21	
13H-6, 065	125.25	140.01	C4A-n2 (t)	8.41	
14H-2, 055	128.65	145.05	C4A-n3 (t)	8.71	
14H-3, 070	130.30	146.70	C4A-n3 (o)	8.80	
14H-4, 025	131.35	147.75	C5-n1 (t)	8.92	
14H-5, 135	133.95	150.35	R -> N		
14H-6, 030	134.40	150.80	N -> R		
16H-6, 150	154.60	174.30	C5-n3 or C5A-n1 (t)(?)	11.03, 11.55	Section break
17H-6, 110	163.70	183.50	C5A-n1 or -n2 (t)(?)	11.55, 11.86	
20H-1, 100	184.60	206.40	C5A-n3 (o)	12.49	Poorly defined
20H-2, 115	186.25	208.05	C5A-n4 (t)	12.58	
20H-4, 020	188.30	210.10	C5A-n4 (o)	12.62	Poorly defined
21H-2, 040	195.00	216.30	C5AA-n (t)	12.83	
21H-4, 130	198.90	220.20	C5AA-n (o)	13.01	

Because of end effects in measurement, the reversal boundaries marked as being at section breaks are probably not well located. t = termination; o = onset.

Elevated levels of interstitial silica sometimes are indicative of recrystallization (Gieskes, 1974). Interstitial silica at Site 845 (Fig. 40D) displays two broad maxima. The largest of these anomalies occurs between 200 and 250 mbsf. This depth range coincides with a zone of apparent recrystallization of siliceous nannofossils (see "Biostratigraphy" section, this chapter), which also overlaps with the onset of lithification at 210 mbsf, as implied from the record of sound velocity (see "Downhole Measurements" section, this chapter). The decreasing trend in silica below Sample 138-845A-25X-4 (232.5 mbsf) apparently has been influenced by uptake into basal sediment and basement rocks.

Concentrations of interstitial strontium are known to increase during alteration of volcanic material and during the recrystallization of calcite (Elderfield and Gieskes, 1982). Strontium (Fig. 39B) at this site displays a trend similar to that of silica that is consistent with recrystallization.

Lithium data (Fig. 39A) display a trend opposite to that for strontium. The negative correlation between lithium and strontium for the combined data sets from Sites 844 and 845 is -0.86 . As at the previous site, the lithium profile here indicates substantial removal within deeper sections of the sediment column, with a return toward a concentration of seawater in the bottom interval.

In summary, diagenesis, recrystallization, and alteration of basalt seem to have influenced the interstitial-water chemistry at Site 845. A mildly reducing environment in these sediments is indicated by profiles of alkalinity (Fig. 38C), sulfate (Fig. 38D), and ammonia (Fig. 39C). Calcium (Fig. 40B), silica (Fig. 40D), and strontium (Fig. 39B) profiles indicate that some recrystallization is going on at this site, at least in the Miocene sections. Alteration of basement rocks are influencing the profiles of magnesium, calcium, potassium, silica, lithium, and strontium in varying degrees.

ORGANIC GEOCHEMISTRY

Carbonate and Organic Carbon

Concentrations of inorganic carbon, total carbon, and total nitrogen were measured in samples from the two lithologic units recovered in Hole 845A. From these measurements, we calculated the weight percentages of calcium carbonate ($\%CaCO_3$) and organic carbon ($\%C_{org}$). Our analytical methods are outlined in the "Explanatory Notes" chapter (this volume). The mean analytical result for each chemical index in each sample is listed in Table 12 (CD ROM, back

pocket) with respect to both ODP depth (mbsf) and to composite depth (mcd; see "Composite Depth" section, this chapter). Duplicate analyses of aliquots from the same sample show that, on average, the percentage of $CaCO_3$ values are reproducible to within 0.4% (Table 13). The downhole profiles of percentages of $CaCO_3$ and C_{org} in Hole 845A vs. depth are shown in Figure 41, and the downhole profiles of these two components vs. composite depth and age (see "Sedimentation Rates" section, this chapter) are shown in Figure 42.

The sedimentary sequence recovered at Site 845 was subdivided into two lithologic units (see "Lithostratigraphy" section, this chapter). Unit I (Cores 138-845A-1H to -14H-4, 103 cm) is composed of clay- and siliceous-microfossil-rich sediments and has been subdivided into three subunits. The average percentage of $CaCO_3$ in Subunit IA (Cores 138-845A-1H to -8H-3, 135 cm) is 4.7%, and it ranges from 0.1% to 24.2%. Concentrations of organic carbon average 1% and range from 0.2% to 2.3%. This gradual increase in organic carbon during the late Pleistocene is clearly seen in Figure 41. In Subunit IB (Cores 138-845A-8H-3, 135 cm, to -13H-2, 115 cm), concentrations of calcium carbonate are higher and more variable, averaging 10.6% and ranging from 0.2% to 31.5%. The higher values of percentage of $CaCO_3$ coincide with the scattered nannofossil clays and diagenetic carbonate nodules in the dominantly siliceous sediment. Concentrations of organic carbon, on average, are one-half those of Subunit IA (0.5%) and range from 0.1% to 1.8%. Lithologic Subunit IC (138-845A-13H-2, 115 cm, to 15H-4, 103 cm) is a radiolarian-, clay-, and diatom-rich interval that is virtually free of carbonate (average 0.3%) and has a low average concentration of C_{org} (0.3%).

Lithologic Subunit IIA (Cores 138-845A-15H-4, 103 cm, to -17H-1, 0 cm) marks the transition of that part of the section dominated by clay and biogenic opal to older sediments high in carbonate. The percentage of $CaCO_3$ in this unit averages 34%, which is similar to the average value observed for the transitional unit at Site 844 (33% $CaCO_3$) and is highly variable, ranging from 1% to 68%. Concentrations of organic carbon averages 0.3% and range from 0.1% to 0.7%. Lithologic Subunit IIB (Cores 138-845A-17H-1, 0 cm, to -31X-3, 125 cm) is composed of nannofossil ooze with variable admixtures of clay and radiolarians. This subunit has uniformly high carbonate concentrations that average 78% and range from 55% to 90%. Concentrations of organic carbon average 0.2% and range from 0% to 0.6% in the intervals depleted in carbonate. In carbonate-rich intervals (i.e., $\%CaCO_3$ 80%), we could not measure organic carbon with accuracy, and these concentrations have been excluded from Table 12.

Table 9. Depths of top and bottom of each core in Site 845 in the composite depth section.

Core	ODP depth (mbsf)	Core length (m)	Composite depth (mcd)	Δ (m)
138-845A-1H,	0–7.62	7.62	0–7.62	0.00
2H,	7.60–17.21	9.61	8.48–18.09	0.88
3H,	17.10–26.99	9.89	17.96–27.85	0.86
4H,	26.60–36.49	9.89	28.73–38.62	2.13
5H,	36.10–46.09	9.99	39.61–49.60	3.51
6H,	45.60–55.64	10.04	49.68–59.72	4.08
7H,	55.10–64.91	9.81	59.96–69.77	4.86
8H,	64.60–74.55	9.95	70.90–80.85	6.30
9H,	74.10–84.07	9.97	82.11–92.08	8.01
10H,	83.60–93.61	10.01	92.08–102.09	8.48
11H,	93.10–103.21	10.11	102.86–112.97	9.76
12H,	102.60–112.36	9.76	113.93–123.69	11.33
13H,	112.10–122.13	10.03	124.71–134.74	12.61
14H,	121.60–131.67	10.07	135.58–145.65	13.98
15H,	131.10–141.13	10.03	146.96–156.99	15.86
16H,	140.60–150.62	10.02	158.33–168.35	17.73
17H,	150.10–159.95	9.85	168.91–178.76	18.81
18H,	159.60–169.69	10.09	178.88–188.97	19.28
19H,	169.10–179.16	10.06	189.76–199.82	20.66
20H,	178.60–188.73	10.13	200.93–211.06	22.33
21H,	188.10–198.13	10.03	211.33–221.36	23.23
22H,	197.60–207.59	9.99	222.83–232.82	25.23
23X,	207.10–216.60	9.50	232.33–241.83	25.23
24X,	216.80–218.25	1.45	242.03–243.48	25.23
25X,	226.50–236.09	9.59	251.73–261.32	25.23
26X,	236.10–245.52	9.42	261.33–270.75	25.23
27X,	245.80–255.53	9.73	271.03–280.76	25.23
28X,	255.00–264.56	9.56	280.23–289.79	25.23
29X,	264.60–274.35	9.75	289.83–299.58	25.23
30X,	274.20–283.87	9.67	299.43–309.10	25.23
31X,	283.90–290.91	7.01	309.13–316.14	25.23
138-845B-1H,	3.10–9.73	6.63	5.46–12.09	2.36
2H,	12.60–21.49	8.89	16.13–25.02	3.53
3H,	22.10–27.95	5.85	26.40–32.25	4.30
4H,	31.60–41.19	9.59	35.48–45.07	3.88
5H,	41.10–48.40	7.30	46.50–53.80	5.40
6H,	50.60–59.97	9.37	57.33–66.70	6.73
7H,	60.10–69.85	9.75	66.71–76.46	6.61
8H,	69.60–79.57	9.97	77.98–87.95	8.38
9H,	79.10–89.06	9.96	87.96–97.92	8.86
10H,	88.60–98.57	9.97	98.93–108.90	10.33
11H,	98.10–108.02	9.92	110.21–120.13	12.11
12H,	107.60–117.62	10.02	120.58–130.60	12.98
13H,	117.10–127.04	9.94	131.86–141.80	14.76
14H,	126.60–136.60	10.00	143.00–153.00	16.40
15H,	136.10–144.56	8.46	154.40–162.86	18.30
16H,	145.60–155.55	9.95	165.30–175.25	19.70
17H,	155.10–165.17	10.07	174.90–184.97	19.80
18H,	164.60–174.53	9.93	184.90–194.83	20.30
19H,	174.10–183.73	9.63	194.60–204.23	20.50
20H,	183.60–193.55	9.95	205.40–215.35	21.80
21H,	193.10–203.18	10.08	214.40–224.48	21.30
138-845C-1H,	20.00–29.84	9.84	21.00–30.84	1.00
2H,	29.50–39.52	10.02	31.38–41.40	1.88
3H,	39.00–48.63	9.63	42.30–51.93	3.30

See text for details.

Accumulation Rates

Following the methodology outlined in the “Explanatory Notes” chapter (this volume), we calculated the average values of several sedimentary parameters (%CaCO₃, %C_{org}, LSR, and DBD) in the 23 time intervals delimited by the chronostratigraphic levels discussed in the “Sedimentation Rates” section (this chapter). The average values of percentages of CaCO₃ and C_{org}, linear sedimentation rate (LSR), dry-bulk density (DBD), bulk-sediment mass accumulation rate (bulk MAR), CaCO₃ MAR, and C_{org} MAR for the 23 time intervals between 0 and 16.65 Ma are listed in Table 14. Mean values

Table 10. Control points for accumulation rates.

Composite depth (mcd)	Sediment rate (m/m.y.)	Age (Ma)	Comments
0		0	Top of sedimentary section
12.32	30.0	0.41	T <i>Sylatractus univertus</i>
37.20	20.7	1.61	T <i>Pterocanium prismatium</i>
53.88	12.1	2.92	Kaena (t)
65.55	12.2	3.88	Cochiti (t)
72.05	11.0	4.47	Sijdufjall (o)
76.00	13.2	4.77	Thvera (o)
87.51	19.8	5.35	C3A-n1 (t)
96.28	16.3	5.89	C3A-n2 (o)
104.46	13.4	6.50	C3A-n3 (o)
120.53	18.9	7.35	C4-n3 (t)
129.71	16.6	7.90	C4-n1 (t)
141.53	19.6	8.50	C4A-n2 (o)
164.93	12.2	10.42	C5-n1 (t)
166.83	11.2	10.59	C5-n2 (o)
174.21	16.7	11.03	C5-n3 (t)
183.73	18.4	11.55	C5A-n1 (t)
186.93	17.8	11.73	C5A-n1 (o)
205.08	24.9	12.46	C5A-n3 (t)
215.93	29.3	12.83	C5AA-n (t)
226.08	27.4	13.20	C5AB-n (t)
275.23	17.6	16.60	T <i>Helicosphaera ampliaperita</i>
			845A-27X-3, 42/845A-27X-5-42
309.10	52.1	16.65	845A-30X-CC older than B <i>Cestodiscus</i>
			<i>peplum</i> (16.4 Ma) but younger than B
			<i>Crucidenticula kanayae</i> (16.9 Ma)

(t) = termination; (o) = onset; T = top; B = bottom.

are presented in Figures 43 and 44 in histogram form. Superimposed on these mean values are instantaneous estimates of MAR calculated for each sample. Mean bulk sediment MAR decreased over time from 4 g/cm²/k.y. in the middle Miocene to 0.3 g/cm²/k.y. in the middle Pliocene (Fig. 44) and exhibited temporal patterns similar to, but with values twice as high, as those at Site 844. In the Pleistocene, MARs appear to increase steadily, with C_{org} MARs rising steadily to 10 mg/cm²/k.y. This increase in C_{org} MARs was accompanied by an increase in the noncarbonate MAR, which may be attributed to increasing opal accumulation at this site.

The sudden transition from a regime of high carbonate accumulation prior to 10 Ma to the opaline sedimentary regime that was recognized at Site 844 is considerably less abrupt at Site 845. This difference may be a function of superior age control at Site 845 that shows a series of steplike decreases of bulk sediment MAR from 13 to 10 Ma.

Gas Geochemistry

Sediment samples for gas analysis using the headspace technique were taken every third core from all holes drilled at Site 845. Because the concentrations of hydrocarbon gas yielded by this simple thermal desorption technique did not exceed a background value of about 2 to 3 ppm methane, no data have been presented. The diagenetic situation at Site 845 is similar to that encountered at Site 844. At both sites, the absence of methane may be attributed to continuously oxic to suboxic conditions in both the water column and the sediment; results of sulfate analyses in interstitial waters provide evidence that the diagenetic phase of sulfate reduction, which precedes fermentation and methanogenesis, has not progressed significantly (see “Inorganic Geochemistry” section, this chapter). These observations are puzzling, because organic carbon concentrations were not low enough to attribute the absence of sulfate reduction and fermentation at these sites to the absence of substrate for microbial activity. A possible reason for the low rate of sulfate reduction and, consequently, the absence of methanogenesis, may be that organic matter was present in the sediments in forms that are not readily accessible for microorganisms. This may be the result of thorough microbial degradation of

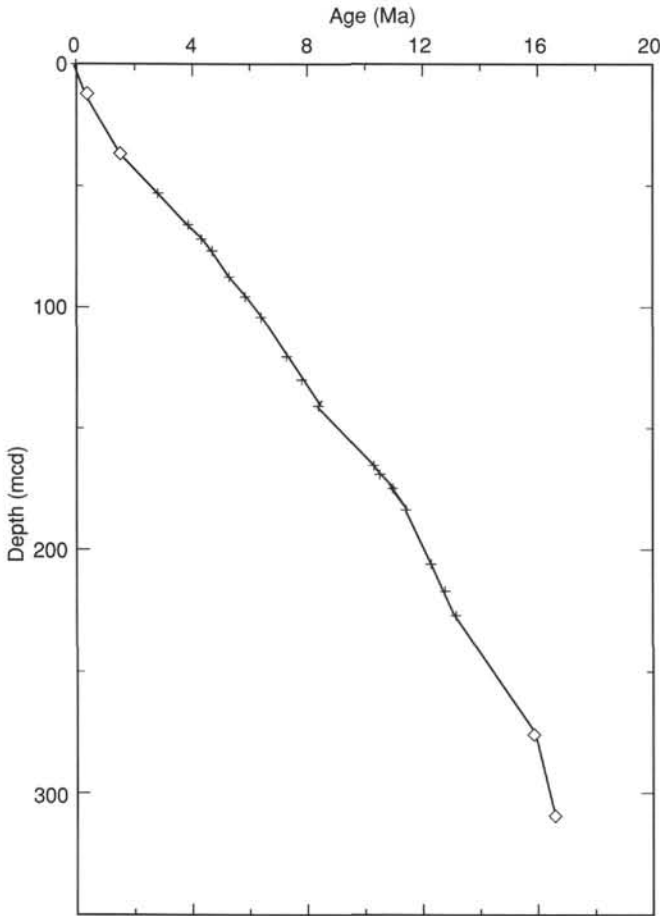


Figure 35. Plot of age vs. depth for Site 845, based on the calibration points in Table 10. Pluses = paleomagnetic control points; open diamonds = biostratigraphic control points.

the organic matter in the oxygenated water column and at the sediment/water interface, so that the remaining organic matter, after screening by aerobic microorganisms, is a poor substrate for anaerobic microbial activity. A second possibility is that part of the organic matter has been preserved from microbial remineralization by the mineral matrix of biogenic hard parts (e.g., diatom frustules).

PHYSICAL PROPERTIES

Introduction

Physical property measurements for whole-round samples of cores recovered at Site 845 include GRAPE-density, compressional-wave velocity (both using the MST), and thermal conductivity. Measurements from split-cores included (1) index properties, such as wet-bulk density, dry-bulk density, water content and porosity; (2) *P*-wave velocity, using the digital sonic velocimeter (DSV); and (3) vane shear strength, using the Wykeham-Farrance vane shear device. In Hole 845A, index properties and *P*-wave velocities were measured twice, and vane-shear strengths were determined once per section. Thermal conductivity was measured in Sections 2 and 5 from each core in Hole 845A. In Hole 845B, *P*-wave velocities and index properties were measured once per section. Measurements of index properties were always performed at the same depth interval as the velocity measurements. Methods of analyses are described in the "Explanatory Notes" chapter (this volume).

The sedimentary section at Site 845 was divided into three major physical property units. Physical property units are defined as depth

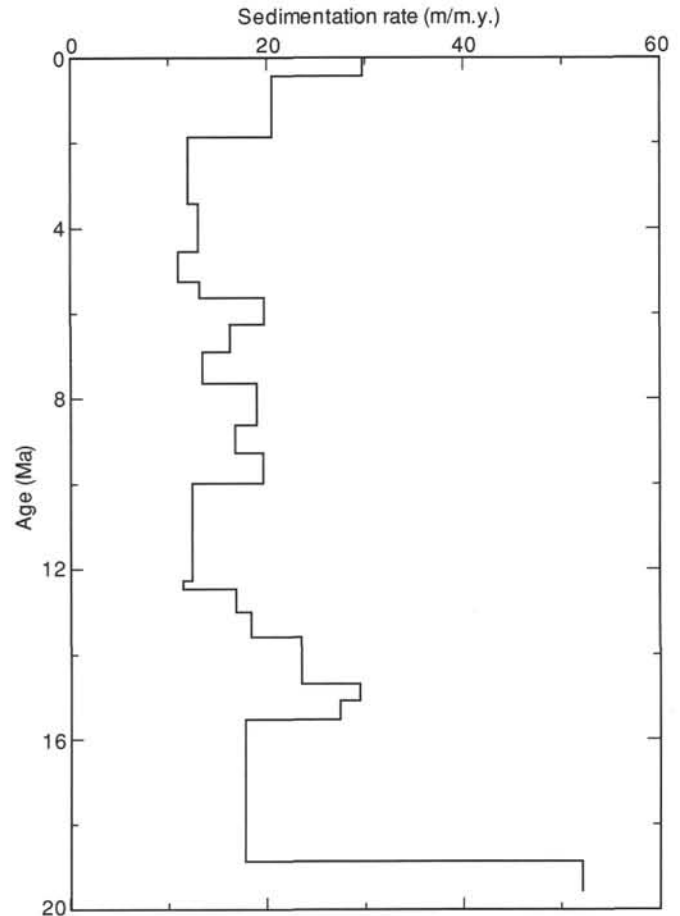


Figure 36. Linear sedimentation rate vs. age, based on data in Table 10.

intervals where similar trends of index properties were recorded. The means and ranges of physical properties for each physical property unit are listed in Table 15. In this section, we describe the downhole distributions of the index properties, DSV data, shear strength, and thermal conductivity from Hole 845A because this hole's data set has the highest resolution. The physical data at Site 845 are summarized in Tables 16 through 19 (CD ROM) and plotted relative to depth below seafloor (mbsf) in Figures 45 through 51.

Index Properties

Physical property Unit I is characterized by little change in index properties with depth and extends from the seafloor to 137.5 mbsf. Physical property Unit II was subdivided into Subunit IIA and Subunit IIB. Subunit IIA (137.7–152.6 mbsf) is characterized by a sharp increase (offset of 0.23 g/cm^3) in wet-bulk density (Fig. 45) and decreases in water content (Fig. 47) and porosity (Fig. 48). Subunit IIB (152.6–247.7 mbsf) is characterized by a gradual increase in wet-bulk density with depth (offset of 0.2 g/cm^3) and gradual decreases in porosity and water content with depth. Physical property Unit III (247.7–base of hole) is characterized by a slight decrease in wet-bulk density (offset of $0.8\text{--}1.0 \text{ g/cm}^3$) and slight increases in water content and porosity.

Compressional-Wave Velocity

Compressional-wave velocity was measured perpendicular to bedding. Compressional wave velocities (Fig. 49) are constant in the upper 50 m of the section. From 50 to 127 mbsf, an increase in *P*-wave velocity is seen and then a decrease in velocity from

Table 11. Interstitial-water geochemical data for Holes 845A and 845C.

Core, section, interval (cm)	Depth (mbsf)	pH	Salinity	Chloride (mM)	Sodium (mM)	Alkalinity (mM)	Sulfate (mM)	Magnesium (mM)	Calcium (mM)	Potassium (mM)	Strontium (μ M)	Lithium (μ M)
Hole C												
138-845C-1H-1, 147-150	21.5	7.59	35.8	560	478	4.391	27.96	52.43	10.60	12.1	89.1	26.0
1H-3, 146-150	24.5	7.56	35.5	559	477	4.294	28.24	52.45	10.58	12.7	92.0	26.3
2H-6, 145-150	38.9	7.56	35.8	560	476	4.253	26.96	52.57	10.78	11.7	95.2	25.0
Hole A												
138-845A-6H-4, 145-150	51.6	7.68	35.8	560	475	4.360	27.04	52.36	10.91	12.4	96.1	24.6
9H-4, 145-150	80.1	7.53	35.8	558	474	4.329	27.32	52.18	11.09	11.8	106.0	22.6
12H-4, 145-150	108.6	7.55	35.5	560	475	4.188	26.96	51.83	11.43	12.0	110.0	21.3
15H-4, 145-150	137.1	7.39	35.5	561	476	4.377	26.69	51.64	11.79	11.1	123.0	20.3
18H-4, 145-150	165.6	7.42	35.3	559	475	3.901	26.46	51.51	11.43	11.3	130.0	19.2
21X-4, 145-150	194.1	7.30	35.3	551	468	3.894	26.83	51.61	11.49	11.0	137.0	18.9
25X-4, 145-150	232.5	7.45	35.5	558	474	2.973	26.76	52.22	11.05	11.5	137.0	18.9
27X-4, 142-150	251.8	7.39	35.5	558	474	3.329	27.22	52.20	11.56	10.7	138.0	19.6
28X-4, 142-150	261.0	7.57	35.5	560	475	3.409	26.86	52.49	11.50	10.5	132.0	20.3
29X-4, 147-150	270.6	7.55	35.5	558	476	3.074	27.75	52.54	11.13	10.5	122.0	21.3
30X-2, 142-150	277.2	7.46	35.5	558	475	3.077	28.13	53.06	11.02	10.9	110.0	21.9
31X-5, 142-150	291.4	7.58	35.5	550	471	2.499	27.80	51.25	10.16	11.1	94.0	27.7

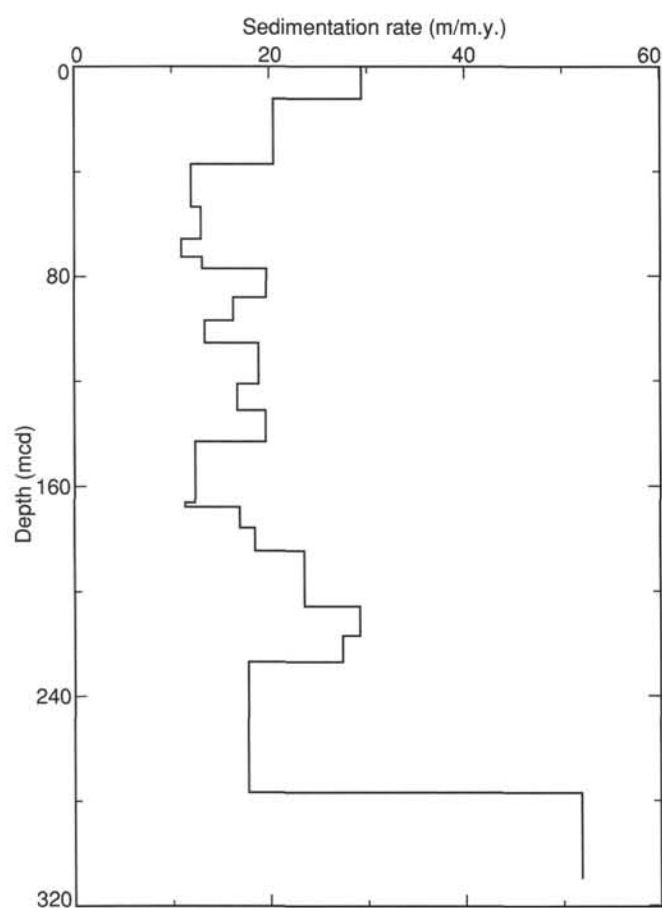


Figure 37. Linear sedimentation rate vs. composite depth, based on data in Table 10.

127 to 152 mbsf. From 152 mbsf to the base of the hole, the *P*-wave velocity increases. Compressional-wave velocities become more variable after the change from APC- to XCB-coring. This variability may result from disturbances of the sediments during XCB-coring and/or difficulty when measuring velocity in stiffer sediments.

Thermal Conductivity

Thermal conductivity (Fig. 50) is constant with depth throughout physical property Unit I and increases from 0.82 to 0.95 W/(m • K) in Subunit IIA. Thermal conductivity increases from 0.95 to 1.2 W/(m • K) in Subunit IIB, while in physical property Unit IIIB, thermal conductivity varies with depth. Because thermal conductivity is a function of the density of a sediment, thermal conductivity profiles generally mirror the wet-bulk density profile and are inversely related to water content and porosity.

Shear Strength

Undrained shear strength (Fig. 51) values range from 2.2 to 119.1 kPa and generally increases with depth below the seafloor. Shear strength increases steadily from 0 to 70 mbsf. From 70 to 92 mbsf, shear strength values are offset upward by 20 kPa. Shear strength is highly variable from 92 mbsf to the bottom of Hole 845A. The variability in shear strength values results from changes in lithology between diatom-rich ooze to nannofossil ooze. Peak shear strength values were seen at 110, 127, and 166.6 mbsf and may be related to an increase in the siliceous component of the sediments, which contain 20% diatoms in these intervals. A marked decrease in shear strength at 209.6 mbsf corresponds to the change from APC- to XCB-coring.

Relationships of Physical Properties to Lithology

A comparison of physical properties reveals that physical property Unit I correlates with lithologic Unit I. The low wet-bulk density and high water content correlate with the siliceous diatomaceous sediments of lithologic Unit I. The absence of any systematic change with depth and the high water content in this unit may be attributed to the interlocking structure of the diatom frustules. High framework strength is capable of supporting a sediment load and maintaining open pore spaces (Hill, 1990). Here, this high framework strength also is reflected in the shear strength profile, where peak shear strengths generally occur within diatomaceous sediments.

The sharp changes in physical properties Subunit IIA correspond to the transition from siliceous to carbonate-rich sediments. Within this interval, bulk density increases and shear strength becomes more variable. The continued increase in bulk density (decreased porosity and water content) with depth in physical properties Subunit IIB is the result of gravitation compaction from increasing overburden.

Table 11 (continued).

Core, section, interval (cm)	Silica (μM)	Ammonia (μM)
Hole C		
138-845C-1H-1, 147-150	772	116
1H-3, 146-150	780	129
2H-6, 145-150	647	151
Hole A		
138-845A-6H-4, 145-150	716	153
9H-4, 145-150	730	108
12H-4, 145-150	820	133
15H-4, 145-150	720	131
18H-4, 145-150	830	68
21X-4, 145-150	939	59
25X-4, 145-150	1014	32
27X-4, 142-150	908	11
28X-4, 142-150	845	4
29X-4, 147-150	904	4
30X-2, 142-150	787	4
31X-5, 142-150	505	7

Summary

Results from Site 845 illustrate that the downhole distribution in physical properties primarily is controlled by sediment type. The diatomaceous sediments in the upper 135 m are associated with low wet-bulk density and high water content and shear strength. Within these sediments, index properties show no systematic change with

depth. The underlying carbonate-rich sediments have higher wet-bulk densities and lower water content and shear strengths. In addition, within these carbonate-rich sediments, downhole trends in index properties (increasing wet-bulk density, decreasing water content) are indicative of sedimentary compaction.

DOWNHOLE MEASUREMENTS

Data Quality

In general, the quality of the logs from logging runs of all three tool strings was good. We used the natural gamma-ray log (NGT) to correlate logs from three runs to a common depth scale (Table 20). The FMS log was shifted downward by 2 m; no shift was required in the geophysical or geochemical logs.

The only dropout observed in the density log at this site was found at the base of the log. In addition, because the heave compensator was operating, FMS data are generally of high quality, at least below 130 mbsf. We observed few occurrences of "chattering," intervals of vertical lines caused by uncompensated heave, in the FMS logs. Above 130 mbsf, large hole size resulted in only two of the four pads of the tool contacting the borehole wall.

Log Stratigraphy

We used density, velocity, resistivity, natural gamma-ray, and GST Ca logs to distinguish three log units at Site 845. These units were chosen independently of laboratory data, but as discussed next, correlate well with the lithologic units (see "Lithostratigraphy" section, this chapter) and with other laboratory measurements.

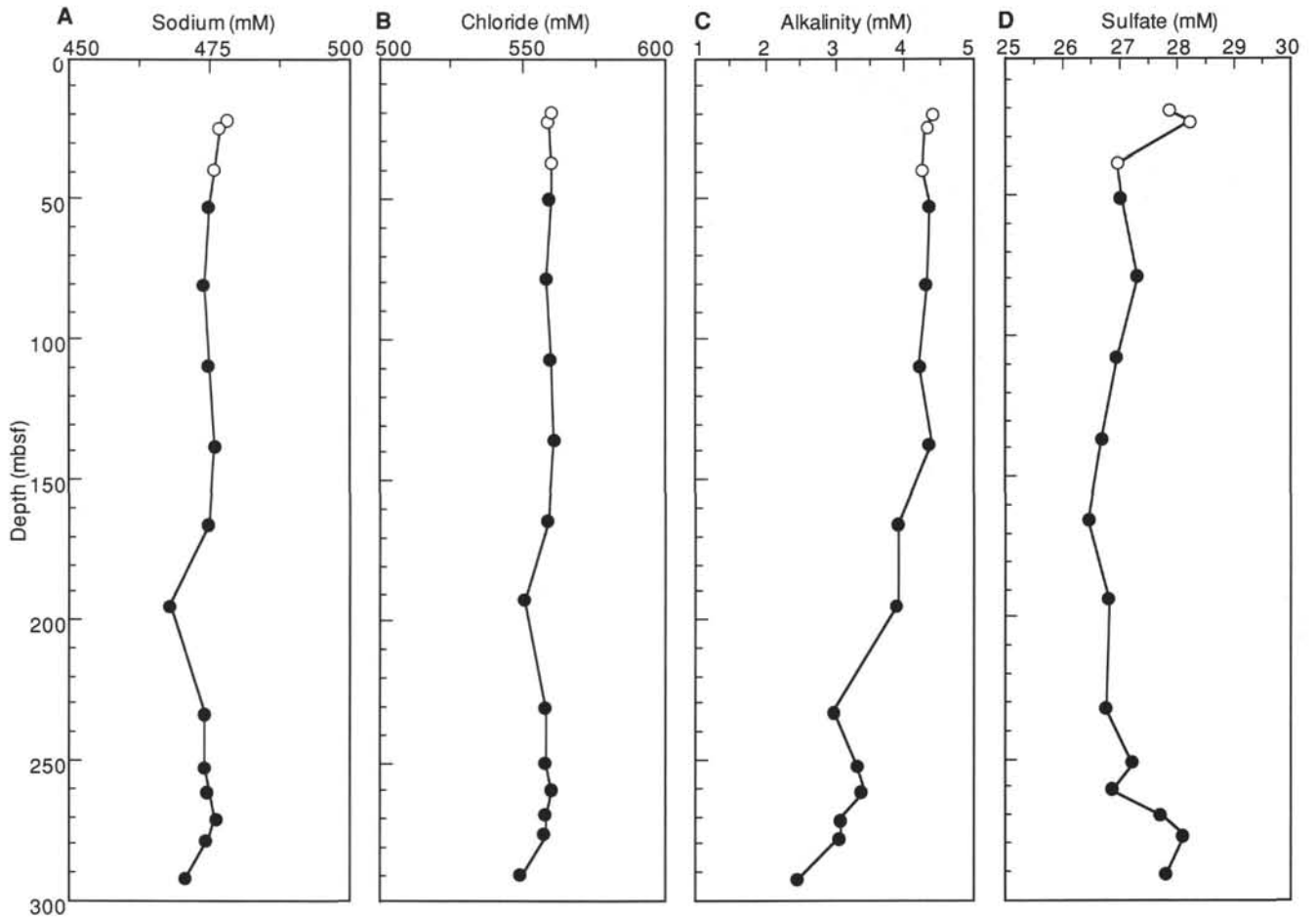


Figure 38. Interstitial-water geochemical data vs. depth (mbsf) for Holes 845A (solid circles) and 845C (open circles). A. Sodium. B. Chloride. C. Alkalinity. D. Sulfate.

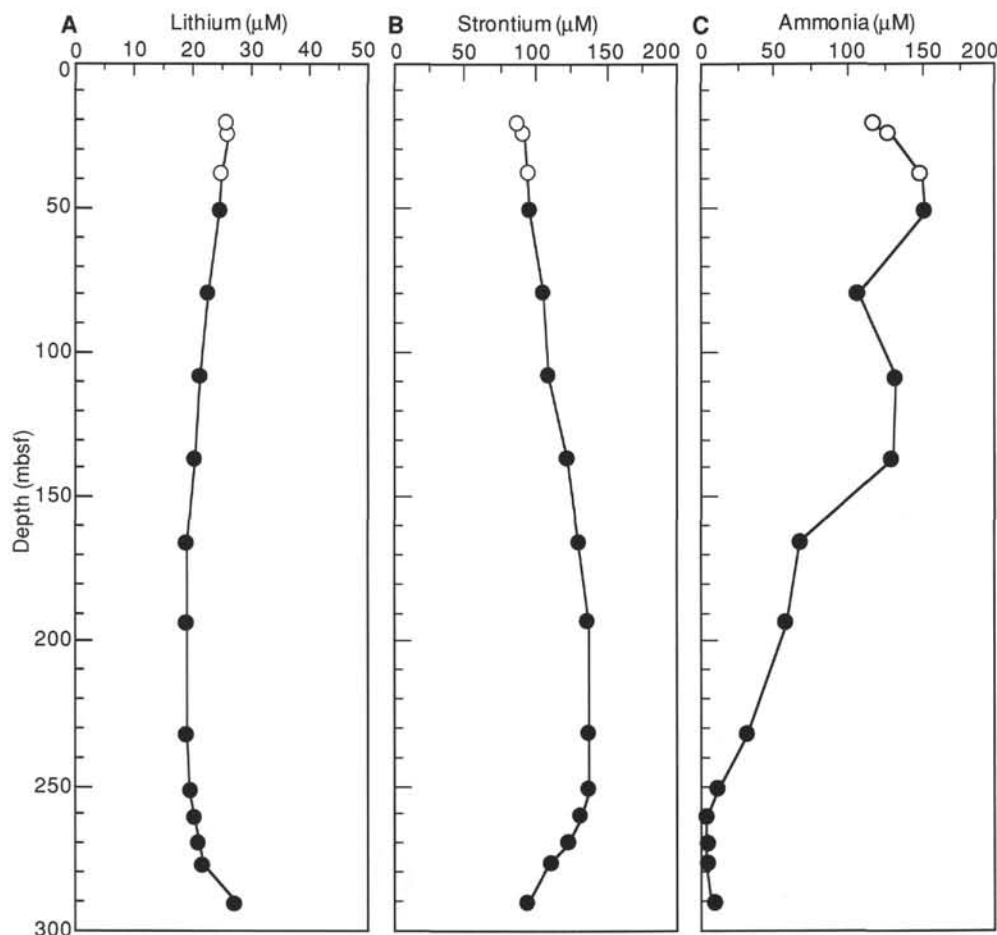


Figure 39. Interstitial-water geochemical data vs. depth (mbsf) for Holes 845A (solid circles) and 845C (open circles). A. Lithium. B. Strontium. C. Ammonia.

Log Stratigraphic Unit 1 (78–151 mbsf; 5.3–10.6 Ma)

Unit 1, from the base of the pipe to approximately 150 mbsf, is characterized by low and nearly constant velocity/density values (Table 21, Figs. 52 and 53). Conversely, gamma-ray measurements in Unit 1 are high and variable (Fig. 53). This variability probably was caused by alternation of layers of high gamma-ray-emitting clays and low emitting biogenic material. The decreasing trend in gamma-ray measurements in this unit correlates with a general decrease in clay minerals (see “Lithostratigraphy” section, this chapter).

Unit 1 is the only log unit that was distinguished by any strong chemical signature. The calcium yield in Unit 1 is significantly lower than in either Units 2 or 3 (Table 21, Fig. 54), because of the low calcareous microfossil content in the upper 150 mbsf of this site (see “Lithostratigraphy” section, this chapter). Average values of Si-yields in the three log units differ. Unit 1, which contains the highest concentration of siliceous biogenic material and clay minerals, has the highest mean Si-yield (Table 21). However, the three populations are not statistically distinct.

Log Stratigraphic Unit 2 (151–210 mbsf; 10.6–13.4 Ma)

The boundary of log Unit 1/Unit 2 coincides with the boundary of lithologic Unit II/Unit III (see “Lithostratigraphy” section, this chapter). In the logs, this boundary is delineated by an abrupt increase in density between 150.5 and 151.4 mbsf (Figs. 52 and 55). Resistivity values also increase sharply, but not to the same degree; velocity values actually decrease in the interval where density increases.

Natural gamma-ray activity exhibits the opposite trend by decreasing at 150 mbsf. Gamma-ray activity remains low and much less variable throughout both log Units 2 and 3 (Table 21, Fig. 53). Average gamma-ray activity changes little over the interval of Unit 2, while density, velocity, and resistivity all increase slightly. Cyclic variations in all four measurements overprint the general trends.

Two distinct relationships in velocity vs. depth subdivide Unit 2. A linear increase in velocity was observed from the top of Unit 2 at 151 to about 173 mbsf. At 183 mbsf, velocity decreases sharply, then increases again, but at a lower rate (Fig. 55). The local maximum between 173 and 183 mbsf corresponds to maxima in density and carbonate content (Fig. 55; see “Organic Geochemistry” section, this chapter).

Log Stratigraphic Unit 3 (210–~280 mbsf; 13.4–16 Ma)

The Unit 2/Unit 3 boundary at approximately 210 mbsf coincides with a sharp velocity increase between 209.4 and 210.7 mbsf, from a mean value of 1.54 km/s in Unit 2 to 1.66 km/s in Unit 3 (Table 21, Fig. 55). Similarly abrupt, but smaller, increases were observed in density and resistivity. Unit 3 is characterized by high values of all three parameters; variability is also highest in Unit 3 (Table 21). As in Unit 1, gamma-ray measurements in Unit 3 decrease slightly (Fig. 53).

Correlations with Lithology

Log Unit 1 is characterized by the dominance of siliceous microfossils and clays. The boundary between Units 1 and 2 marks an increase in calcareous components (see “Lithostratigraphy” section,

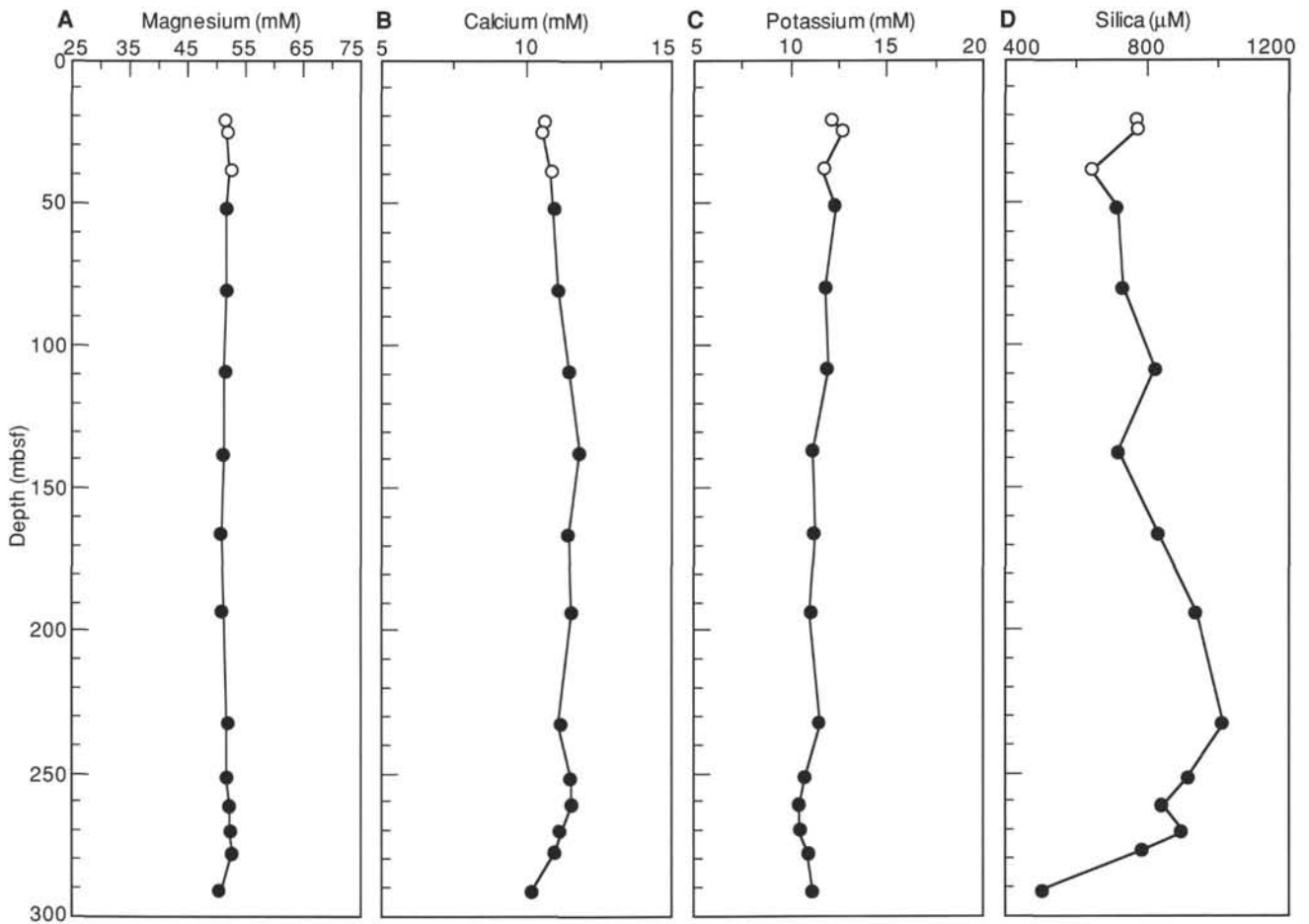


Figure 40. Interstitial-water geochemical data vs. depth (mbsf) for Holes 845A (solid circles) and 845C (open circles). **A.** Magnesium. **B.** Calcium. **C.** Potassium. **D.** Silica.

this chapter), which are distinguished by higher bulk densities and velocities and lower porosities than either clay minerals or siliceous material. Lower porosities manifest themselves by higher resistivity log measurements. The Unit 2/Unit 3 boundary is not marked by any obvious lithologic change. However, this depth is the point at which drilling changed from piston coring to XCB-drilling because of increased stiffness of the sediment. This point marks the onset of lithification of the deposit (see below).

FMS Logs

Between about 220 and 280 mbsf, distinct layering, appearing in the FMS logs as light/dark banding, was observed in many intervals and was replicated in both passes of the FMS log. Layering on the scale of ~5 m thick may correlate with density variations in this interval. Very thin bands, on the order of 5 cm, are present from 260 to 280 mbsf in both FMS logs. However, this scale was beyond the resolution of our log density tool. Evaluation of these thin layers with different resistivity properties ultimately may be matched with GRAPE density measurements.

Density and Velocity Controls

Trends in log density near 150 mbsf are similar to trends in carbonate contents (see "Organic Geochemistry" section, this chapter). Both parameters increase at 143 mbsf, plateau, and then increase to even higher values at about 149 mbsf. Smaller peaks in carbonate

that are shallower in Unit 1 also correlate with local maxima in density (e.g., 91 and 106 mbsf; Fig. 52). This relationship suggests that bulk density in Unit 1 and in the shallow portions of Unit 2 are controlled primarily by carbonate variations. Below approximately 153 mbsf, however, density appears less strongly related to bulk carbonate content. In general, density trends in Unit 3 correlate with variations in nannofossil concentrations, the dominant component below approximately 140 mbsf (see "Lithostratigraphy" section, this chapter). Relationships among density, foraminifer content, and bulk carbonate contents in this interval are less coherent, which suggests that bulk density below about 200 mbsf was controlled more by the dominant sedimentary component (nannofossil tests) than the dominant lithology (carbonate), which also includes lower density foraminifers.

Two processes are responsible for the velocity increases observed in Site 845 deposits. In Unit 2, increasing consolidation reduced porosity and caused slight increases in velocity (Fig. 56). Porosity values were calculated from density logs and average values of grain density, based on laboratory measurements (see "Physical Properties" section, this chapter). The velocity trend parallels Wood's equation (Wood, 1930), which models the behavior of unconsolidated sediment deposits (Wilkins et al., 1990) and describes the interactive effects of increasing density and decreasing porosity on velocity. Unit 1 and the shallowest 10 m of Unit 2 display a wide range of porosities (70%-85%), with virtually no change in velocity (Fig. 56). The slope of Unit 1 velocity vs. porosity is positive, in accord with Wood's equation, which predicts a minimum in velocity at 78% porosity. We suspect that these very low velocities are related primar-

Table 13. Duplicate analyses of percentages of CaCO₃ in samples from Site 845.

Core, section, interval (cm)	ODP depth (mbsf)	Composite depth (mcd)	First run CaCO ₃ (%)	Second run CaCO ₃ (%)	Absolute value of CaCO ₃ (difference)
845A-2H-3, 40-42	11.01	11.89	6.17	5.83	0.33
2H-6, 40-42	15.51	16.39	24.34	23.17	1.17
3H-2, 40-42	19.01	19.87	2.50	2.00	0.50
3H-3, 40-42	20.51	21.37	10.50	10.17	0.33
10H-6, 100-102	92.11	100.59	27.09	26.34	0.75
11H-6, 100-102	101.61	111.37	2.17	1.58	0.58
16H-2, 110-112	143.21	160.94	68.09	67.59	0.50
16H-6, 110-112	149.21	166.94	39.17	38.09	1.08
25X-6, 145-150	235.48	260.71	75.92	75.84	0.08
27X-4, 110-112	251.41	276.64	60.92	64.09	3.17
27X-6, 145-150	254.78	280.01	62.42	62.89	0.47
29X-2, 106-108	267.17	292.40	58.59	57.67	0.92
31X-3, 38-40	287.29	312.52	55.34	54.00	1.33
Average					0.86

Note = The average difference between the original and duplicate analyses was 0.9% for CaCO₃. Average value of the original and the duplicate analyses are reported in Table 12.

Table 14. Averages values of sedimentary parameters calculated over time intervals defined by chronostratigraphic levels.

Composite depth (mcd)	Age (Ma)	Mean CaCO ₃ (%)	Mean C _{org} (%)	Mean sed. rate (m/m.y.)	Mean DBD (g/cm ³)	Mean bulk MAR (g/cm ² × k.y.)	Mean CaCO ₃ MAR (g/cm ² × k.y.)	Mean Non-CaCO ₃ MAR (g/cm ² × k.y.)	Mean C _{org} MAR (mg/cm ² × k.y.)
12.32	0.41	3.83	1.33	30.05	0.24	0.72	0.03	0.69	9.59
37.20	1.61	6.14	1.08	20.73	0.26	0.54	0.03	0.51	5.90
53.00	2.92	3.54	0.72	12.06	0.25	0.30	0.01	0.29	2.18
65.55	3.88	1.90	0.46	13.07	0.28	0.36	0.01	0.36	1.65
72.05	4.47	1.42	0.32	11.02	0.29	0.32	0.00	0.31	1.03
76.00	4.77	13.92	0.69	13.17	0.30	0.39	0.05	0.34	2.68
87.50	5.35	3.83	0.60	19.83	0.24	0.47	0.02	0.46	2.86
96.30	5.89	11.70	0.39	16.30	0.25	0.41	0.05	0.36	1.61
104.45	6.50	11.18	0.38	13.36	0.24	0.32	0.04	0.28	1.22
120.55	7.35	13.05	0.45	18.94	0.24	0.46	0.06	0.40	2.09
129.70	7.90	9.70	0.61	16.64	0.23	0.39	0.04	0.35	2.38
141.45	8.50	0.30	0.26	19.58	0.24	0.47	0.00	0.47	1.22
164.95	10.42	19.28	0.33	12.24	0.29	0.35	0.07	0.28	1.15
166.85	10.59	51.67	0.25	11.18	0.41	0.46	0.24	0.22	1.17
174.20	11.03	65.49	0.27	16.70	0.55	0.92	0.60	0.32	2.43
183.75	11.55	69.98	0.21	18.37	0.59	1.09	0.76	0.33	2.32
186.95	11.73	71.34	0.23	17.78	0.61	1.09	0.78	0.31	2.50
205.10	12.46	81.42		24.86	0.69	1.72	1.40	0.32	
215.95	12.83	78.17		29.32	0.70	2.06	1.61	0.45	
226.08	13.20	81.34		27.38	0.75	2.04	1.66	0.38	
275.23	16.00	82.59		17.55	0.82	1.44	1.19	0.25	
309.10	16.65	75.56		52.11	0.74	3.87	2.92	0.94	

Note: For discussion of chronostratigraphic levels, see "Sedimentation Rates" section (this chapter). Parameters are percentages of CaCO₃, C_{org}, dry-bulk density (DBD), linear sedimentation rate (LSR), mass accumulation rate (MAR), CaCO₃ MAR, and C_{org} MAR. After this table was constructed on board the ship, depths of the age control points were changed (see "Sedimentation Rates" section, this chapter, for the final selection of age control points). These depth changes were minor (less than 5 m). None were incorporated in this table, nor in the accompanying Figures, 42, 43, and 44.

ily to the open sediment structure of the siliceous sediments in the upper 160 mbsf at this site. The change in lithology to carbonate-rich sediments is apparent in the decreases in porosity observed in Unit 2.

Porosity reduction also is a key factor in the increase of velocity observed in Unit 3. Cementation, however, is a more significant influence in Unit 3, as shown by the steeper slope of the velocity-vs.-porosity relationship for Unit 3 (Fig. 56), which parallels the Wyllie (Wyllie et al., 1956) line developed for lithified rocks (Wilkins et al., 1990). In addition, a distinct velocity increase clearly delineates Units 2 and 3, suggesting significant lithification of Unit 3. Independent evidence of cementation was observed in interstitial-water silica values, which reach a maximum near 210 mbsf (see "Inorganic Geochemistry" section, this chapter), an abrupt decrease in the state of preservation of siliceous microfossils at this depth (see "Biostratigraphy" section, this chapter), and the need to change from APC- to XCB-coring at this depth. Cementation of the sediment particles by recrystallized silica may be occurring at this depth,

producing an increase in the rigidity of the sediment structure. This increased rigidity also can be seen in shear strength measurements, which increase significantly between 210 and 214 mbsf in Core 138-845A-23X, despite the higher core disturbance associated with XCB-drilling (see "Physical Properties" section, this chapter).

Formation factors (FF) were calculated as the ratio of intermediate resistivity values to the average resistivity of seawater (0.368 ohm-m; Keller, 1982). A linear regression of log FF vs. log porosity yields equations that can be manipulated into the form of the empirical Archie's relationship (Archie, 1942) as follows:

$$FF = A F^{-m},$$

where F = porosity and A and m are empirically determined constants.

Relationships developed for Units 1 and 2 (Table 22) are similar to the Archie's equation for carbonate deposits: $FF = F^{-2}$. The lower

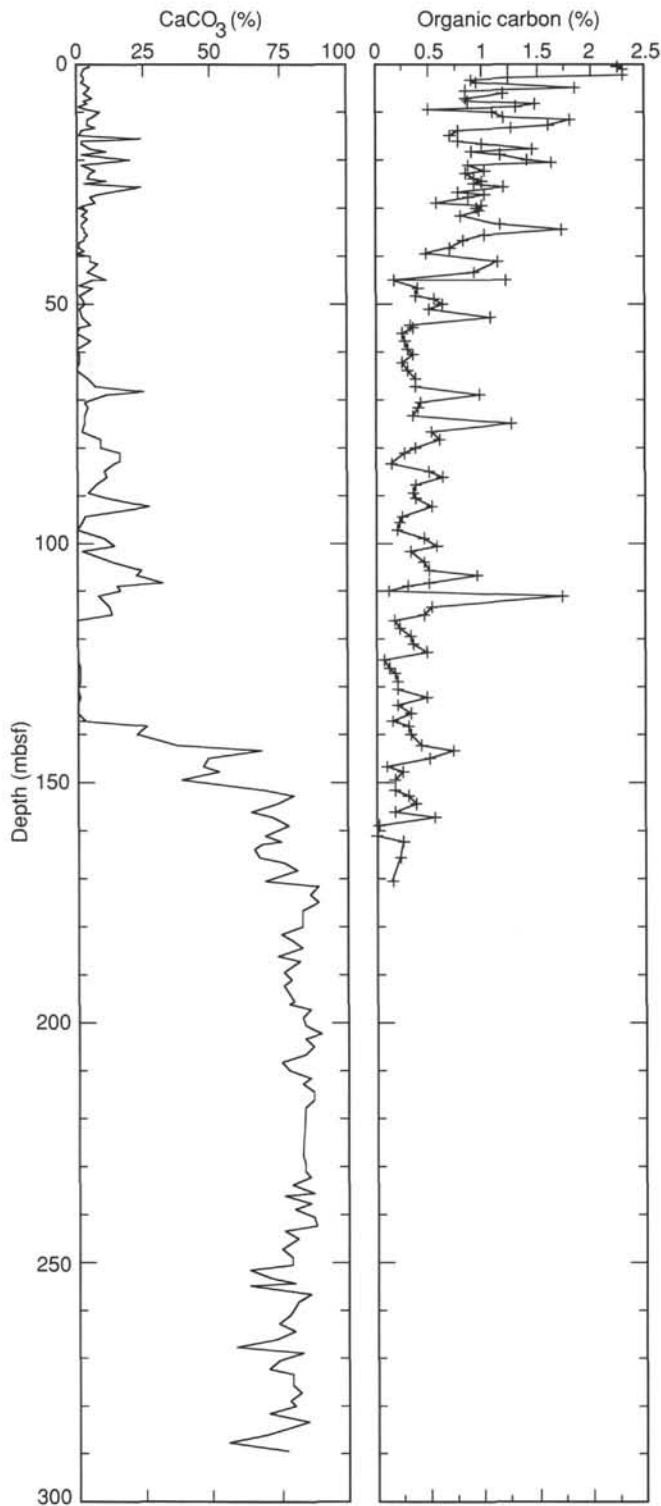


Figure 41. Downhole profile of percentages of CaCO_3 and C_{org} vs. ODP depth (data from Hole 845A).

values of m in Site 845 samples indicate relatively high particle sphericity (Lovell, 1984). The FF–porosity relationship in Unit 3, however, is different (Fig. 57) and suggests either a different lithology, or more likely, a different degree of lithification. The different lithologies in Unit 1, on the other hand, are obvious in the plot of log FF vs. log porosity (Fig. 57). The relationship with the lower slope corre-

sponds to samples from depths of higher silica content. The relationship with the higher slope, which parallels that of Unit 2, corresponds to samples having higher clay and carbonate contents (see “Lithostratigraphy” section, this chapter).

Log vs. Laboratory Physical Property Correlations

Log and GRAPE density values at Site 845 are similar throughout the borehole, when depth shift corrections were applied using CORPAC (Martinson et al., 1982). The difference between log and GRAPE density values fluctuates on or about zero and rarely is greater than about 0.1 g/cm^3 (Fig. 58). Log densities between approximately 95 and 135 mbsf are slightly higher than GRAPE values; log values below about 240 mbsf also, on average, are slightly higher (Table 23; Fig. 58). The low gravimetric density values in the interval from 72 to 140 mbsf may be the result of expansion of the pore fluid and sediment structure in these clay-rich layers (clay content in this interval averages about 50%; see “Lithostratigraphy” section, this chapter). Density correlations below about 150 mbsf are excellent between log and GRAPE measurements; gravimetric density values are slightly lower than those in the log and GRAPE data (Fig. 58).

Differences in the density characteristics between the upper and lower sections of the hole are the result of differences in the sedimentary components. As first observed by Hamilton (1976), any expansion that occurs as a result of retrieval of the core from the seafloor differs, depending on sediment type. Pelagic clays expand more than either carbonate or siliceous oozes. Cemented carbonate-rich deposits, on the other hand, show evidence of little expansion (Urmos et al., in press), primarily because of the high rigidity of the sedimentary framework.

SEISMIC STRATIGRAPHY

Modeling Procedure

Synthetic seismograms were generated from velocity and density models for Site 845 to correlate reflectors in the seismic section to stratigraphic changes.

A density model was created by merging laboratory density with *in-situ* logging density. Depth-shifted logging density (to correlate with Hole 845A GRAPE density) was used over the interval from 89.7 to 279.0 m (89.0–278.3 mbsf; see “Downhole Measurements” section, this chapter). Over the interval from 0 to 89.0 mbsf, 10-point boxcar filtered GRAPE densities from Hole 845A were merged with depth-shifted log densities. Beyond 278.3 mbsf to the basement depth of 291.6 mbsf, we used a constant density of 1.55 g/cm^3 .

A velocity model was created in a similar manner as the density model. From 89.0 to 278.3 mbsf, we used depth-shifted logging velocities. To fill the gap in the upper part of the section, laboratory velocities collected with the DSV were corrected to *in-situ* conditions for changes of sound speed as a function of temperature and pressure, assuming a temperature gradient of 12.6°C/km and a bottom-water temperature of 1.98°C determined from the temperature log. To facilitate a match at the splicing depth of 89.0 mbsf, 10 m/s was subtracted from the corrected DSV velocity data. From 278.3 to 291.6 mbsf, we used a constant velocity value equal to the final log velocity value (1651 m/s).

The accuracy of the traveltime-vs.-depth conversion may be evaluated by generating synthetic seismograms and subsequently comparing them with the seismic record collected over the site. Synthetic seismograms were generated using the above merged velocity and density data. These data were resampled at sample intervals of 1 ms (approximately 60 cm) and then used to calculate acoustic impedance and reflection coefficients and, finally, a synthetic seismogram. Density and velocity values typical of basalt (2.5 g/cm^3 and 3000 m/s, respectively) were added at the basement depth (291.6 mbsf) to generate a basement reflector in the synthetic seismogram. The model we used to generate the synthetic seismogram assumed plane waves,

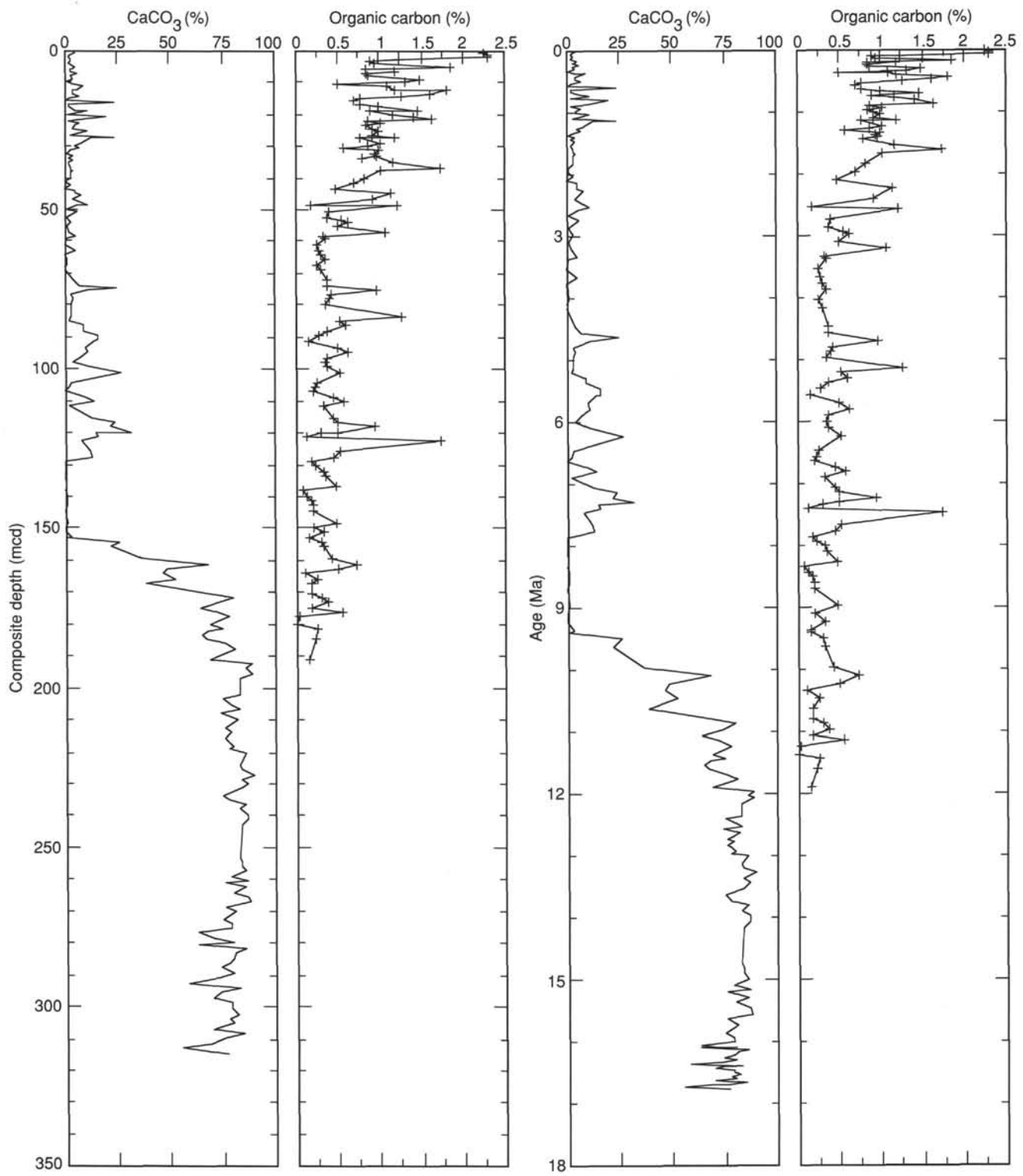


Figure 42. Downhole profiles of percentages of CaCO_3 and C_{org} vs. composite depth and age (data from Hole 845A).

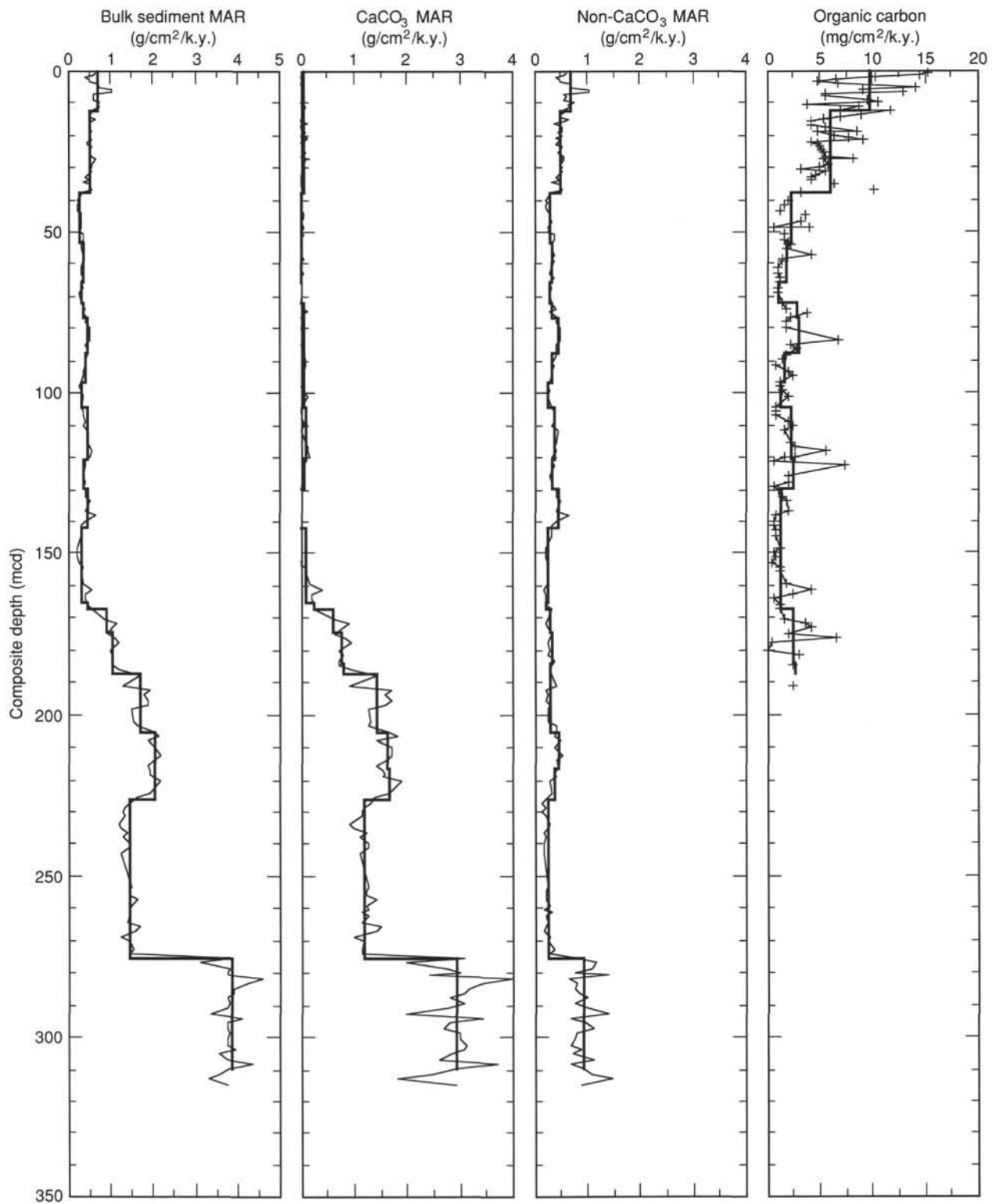


Figure 43. Accumulation rates of bulk sediment, CaCO₃, non-CaCO₃, and C_{org} sedimentary components vs. composite depth at Site 845. Note different units for C_{org}. Thick line = mean value between each stratigraphic datum plane; thin line = discrete accumulation rates calculated for each sample.

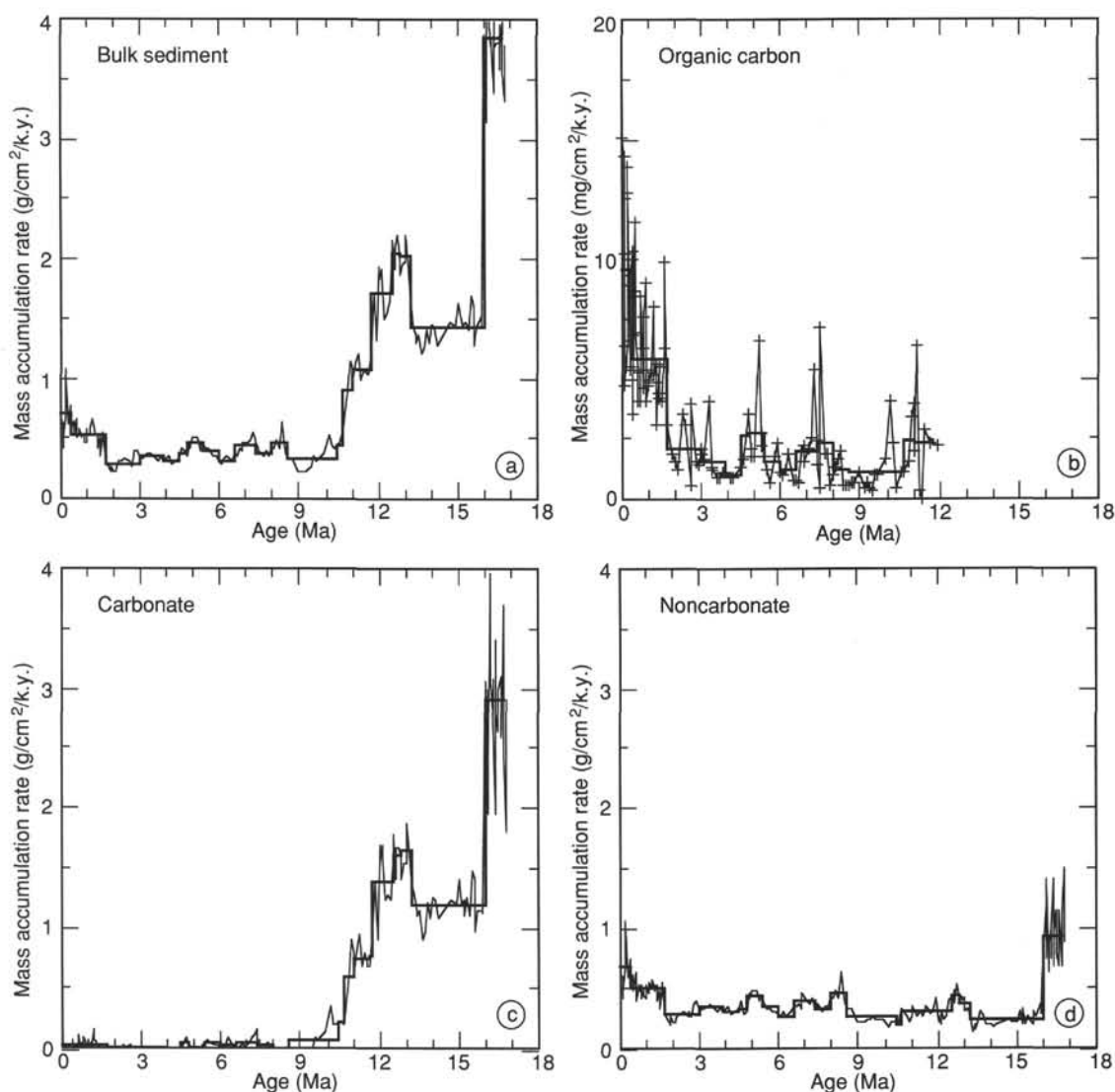


Figure 44. Accumulation rates of bulk sediment (A), C_{org} (B), $CaCO_3$ (C), and non- $CaCO_3$ (D) vs. age in sediments from Site 845. Thick line = mean value between each stratigraphic datum plane; thin line = discrete accumulation rates calculated for each sample. Note different rates for C_{org} .

no multiples, and no signal attenuation; this model was described in Mayer et al. (1985). Our final synthetic seismogram was filtered from 70 to 250 Hz, the same filter parameters as the field record collected during the site survey cruise aboard the *Thomas Washington*.

Results

A comparison of the synthetic seismogram with the seismic profile collected at Site 845 shows a good match between the two (Fig. 59).

Good correspondence is seen between reflectors, with an excellent match at basement, which suggests that the travelttime-vs.-depth conversion is fairly accurate.

Given an acceptable velocity model, the origin of some of the reflectors at Site 845 can be analyzed. We emphasize that these are preliminary results that undoubtedly will be modified after more careful analysis. Fourteen major reflectors or reflector packages were identified. These reflectors were selected on the basis of amplitude and lateral coherence in the seismic record in the immediate area of

Table 15. Averages and ranges of index properties for each physical properties unit at Site 845.

	Wet-bulk density (g/cm^3)		Grain density (g/cm^3)		Dry water content (%)		Porosity (%)	
	Avg.	Range	Avg.	Range	Avg.	Range	Avg.	Range
Physical properties Unit I	1.17	1.10–1.23	2.41	1.93–2.96	376.5	166.7–640.6	89.9	79.9–93.6
Physical properties Subunit IIA	1.26	1.18–1.35	2.60	2.29–2.89	225.5	153.4–407.7	84.3	73.7–91.6
Physical properties Subunit IIB	1.47	1.34–1.66	2.66	2.29–2.83	103.7	70.9–158.6	72.7	65.0–81.0
Physical properties Unit III	1.46	1.30–1.59	2.60	2.01–2.82	100.6	76.1–87.9	71.8	67.5–83.1

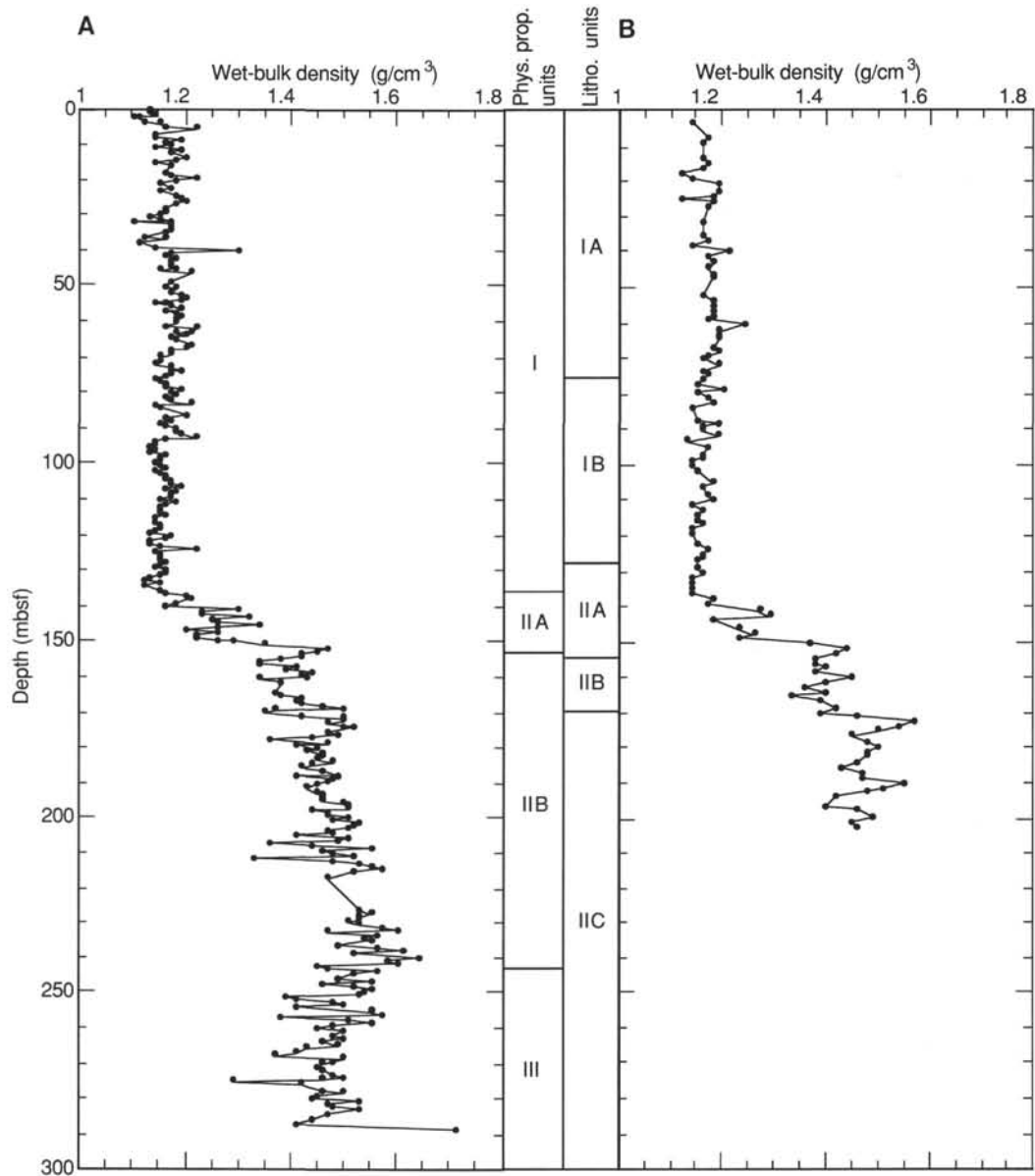


Figure 45. Wet-bulk density (g/cm^3) vs. depth for Holes 845A (A.) and 845B (B). Physical property and lithologic units are shown.

Site 845. Values of two-way traveltime in the synthetic seismogram of the top and bottom of each reflector were measured, and by using our assumed velocity model, we determined the depth range of each reflector.

Our velocity, density, and acoustic impedance models were compared to the depth ranges calculated from the traveltime to determine any changes in the physical properties that caused the selected seismic reflectors. In general, within 1 m of each calculated depth range, a large change in density and/or velocity could be associated with each reflector (Fig. 60). Reflector 8 is an exception to this rule; the large density change thought to cause this reflector was observed about 3.5 m below the value calculated from the synthetic seismogram and the velocity model. This finding clearly suggests a problem with the velocity model between Reflectors 7 and 9. Reflectors for the upper 170 m (Reflectors 0 through 12B) are related solely to large changes in density. Beyond 170 m, the reflectors result from primarily synchronous, large fluctuations in velocity and density, with relative changes in density being generally greater. However, Reflector 16 is

mostly the result of a large increase in velocity, which is associated with recrystallization of silica (see "Downhole Measurements" section, this chapter). Depths (synthetic, mbsf, and mcd) and ages (based on magnetostratigraphy and biostratigraphy of Site 845; see "Sedimentation Rates" section, this chapter) of these reflectors are presented in Table 24. A detailed understanding of the lithologic, biostratigraphic, and, ultimately, paleoceanographic significances of these events must await shore-based studies at this time.

SUMMARY AND CONCLUSIONS

Double (and where necessary, triple) APC-coring, in conjunction with the real-time analyses of continuous core logs (GRAPE, susceptibility, and color reflectance) assured the recovery of a continuous record of sedimentation at Site 845 that spanned the last 17 Ma. Before presenting a general description of the geologic history contained in this sediment section, we must first present the tectonic setting of the

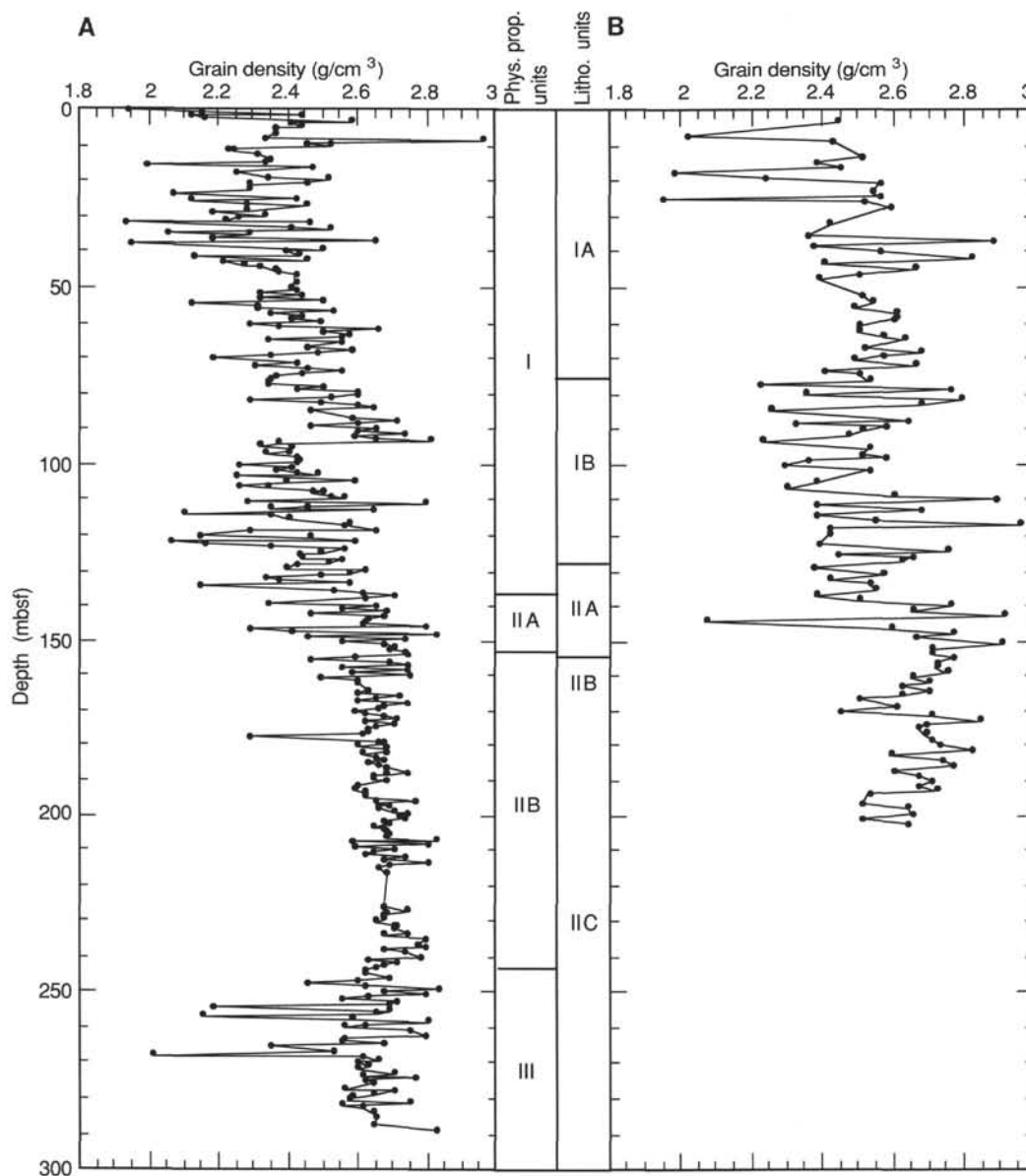


Figure 46. Grain density (g/cm^3) vs. depth for Holes 845A (A) and 845B (B). Physical property and lithologic units are shown.

site and some implications of the estimated basement age. While the local tectonic history of this area of the Pacific Ocean was not an important objective of Leg 138, drilling results do provide an age for the previously undated magnetic anomalies of the region and, more importantly, provide important constraints on the backtrack history of Site 845. An accurate backtrack path is required for understanding the paleoceanographic record of the site.

Site 845 is located within a region where the magnetic anomaly pattern has been mapped, but has not been correlated with the known magnetic time scale (Klitgord and Mammerickx, 1982). Based on estimated East Pacific Rise spreading rates for the Cocos Plate (71 mm/yr; Hey et al., 1977) and from crustal subsidence models, we expected the age of the basement to be about 15 Ma (see Fig. 2). Initial biostratigraphic analyses of Site 845 samples place the basement in the lower Miocene (CN3, NN4) at about 17 Ma. While the 2-m.y. discrepancy may be dismissed as the result of inaccuracies in spreading rate,

subsidence rate, and biostratigraphic determinations, one might also deduce that this discrepancy requires our rethinking the existing plate reconstruction models for the region. For example, the spreading rate for the East Pacific Rise may not represent the true, long-term, average spreading rate for this part of the Pacific, or, the Berlanga Rise to the west of Site 845 may be a fossil spreading center (as suggested by Klitgord and Mammerickx, 1982) and thus the basement at Site 845 may not have been formed at the East Pacific Rise.

The basement age at DSDP Site 495, which may have formed along the same spreading segment of the Cocos Plate, provides a means of estimating early Miocene spreading rates. The sediment above the basement at Site 495 was biostratigraphically dated as early Miocene (Auboin and von Huene, 1982). Assuming 22 Ma as the oldest possible age for the basement at Site 495 and an age of 17 Ma for that at Site 845, we estimated a minimum spreading rate of about 65 mm/yr during the early Miocene. Should this estimate represent

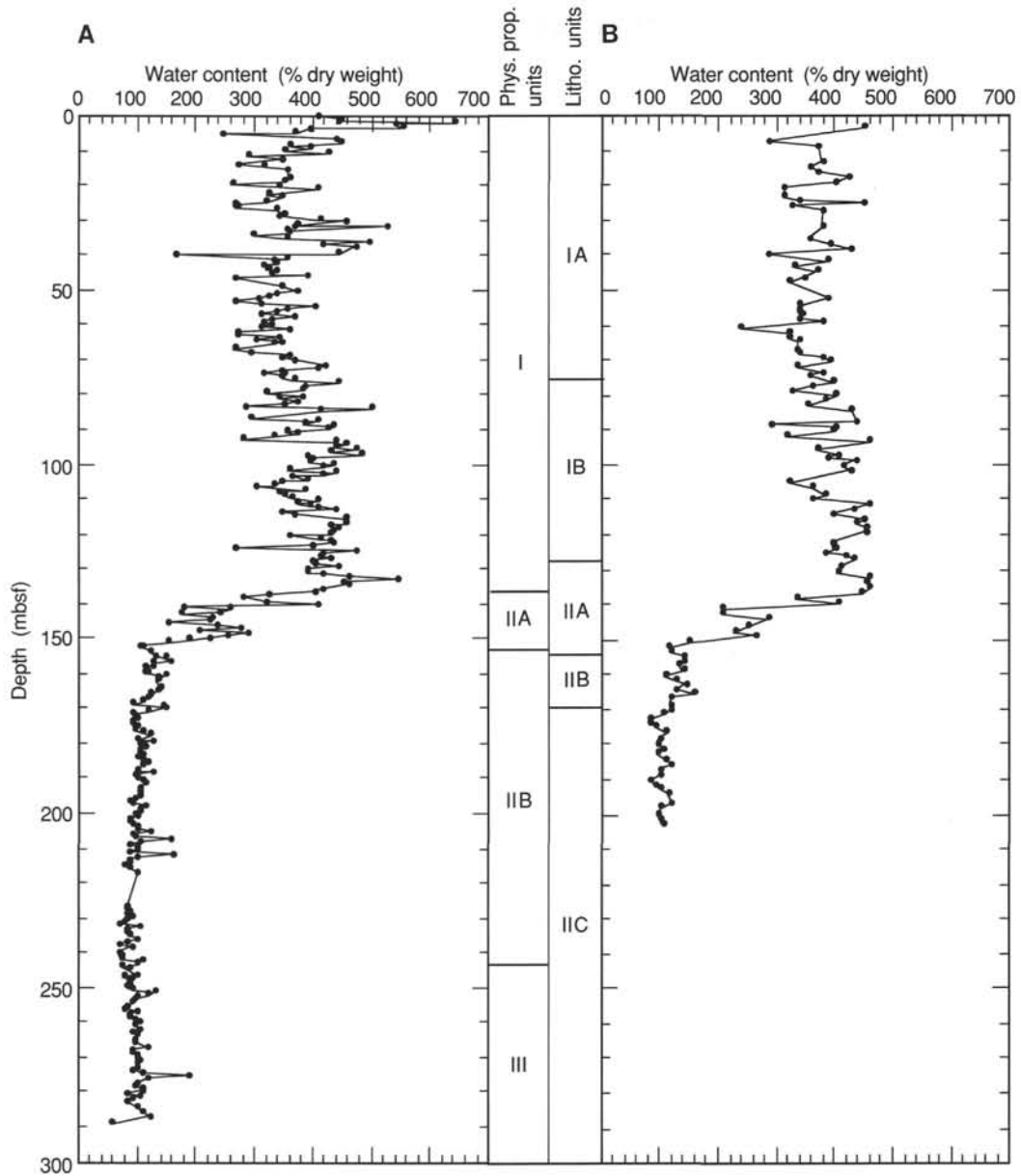


Figure 47. Water content (% dry weight) vs. depth for Holes 845A (A) and 845B (B). Physical property and lithologic units are shown.

the average rate for East Pacific Rise spreading, then the estimated age of the basement at Site 845 is about 16.5 Ma—not much different from the age derived on the basis of micropaleontological results from Site 845. If the Berlanga Rise is indeed a fossil spreading center, then this estimate of the minimum spreading rate suggests that the ridge became inactive about 2 m.y. after the formation of the crust at Site 845. In addition, these estimated spreading rates would not require a large change in spreading rate from the Berlanga Rise to the new East Pacific Rise.

Mammerickx and Klitgord (1982) suggested that the spreading history of the Cocos Plate has been uniform since the major reorganization of the eastern Pacific spreading centers at about 12.5 Ma. Assuming 15 Ma as the end of spreading on the Berlanga Rise, we postulate that the absolute pole for the Cocos Plate is a reasonable representation of the backtrack path for Site 845 over at least the last 15 m.y. (see Fig. 2). Thus, we have a higher degree of confidence in the paleolatitudes listed in Table 25 for Site 845

during the last 12 m.y., a lesser degree of confidence for the period of 12 to 15 Ma, and the least confidence in the oldest 3 m.y. of paleolatitude estimated.

The initial paleolatitude of the site was between 4° and 5° north of the equator. Within the present oceanographic setting, this would place Site 845 at the northern limit of the South Equatorial Current (SEC) at the time of its creation. Sedimentation at Site 845 began with the accumulation of metalliferous nannofossil ooze, followed by an interval of high carbonate accumulation. Initially, sedimentation rates may have been as high as 50 m/m.y., but over the interval of high carbonate accumulation (17–11.5 Ma), sedimentation rates averaged about 26 m/m.y. (Fig. 61A). The average sedimentation rate was about 35% less than the rate we observed for the same interval at Site 844, whose latitudinal position was about 2° farther south. This difference may reflect a gradient in surface production across the 2° of latitude, a gradient even less than that observed today, and/or a difference in water depth and its associated dissolution differences.

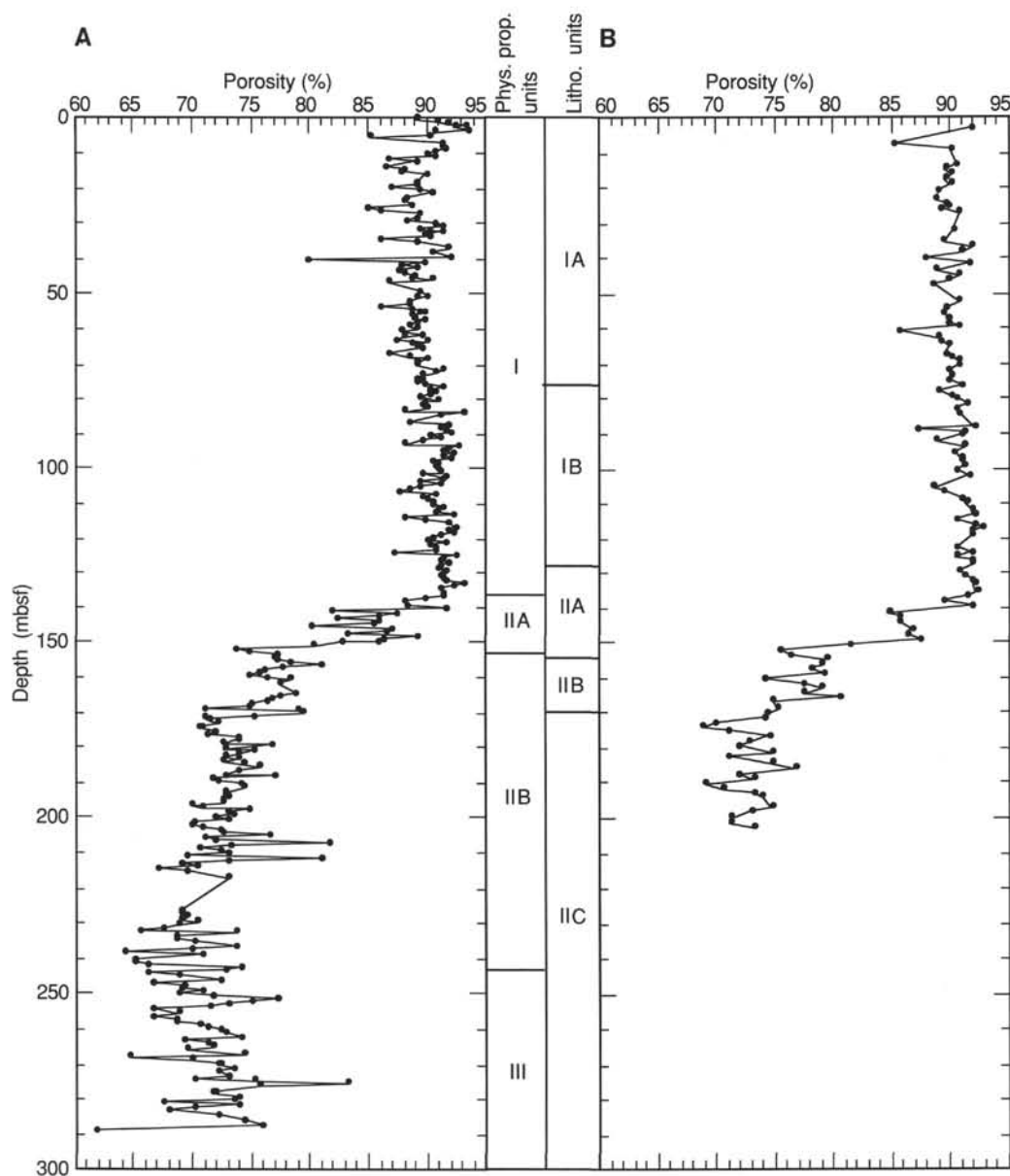


Figure 48. Porosity (%) vs. depth for Holes 845A (A) and 845B (B). Physical property and lithologic units are shown.

While the sharp decrease in sedimentation rate at about 16 Ma most probably is an artifact of the limited number of datums we used for constructing the sedimentation rate curve, it is likely that this interval did see a reduction in sedimentation rate as the site traveled out from under the influence of the equatorial divergence. This conclusion is supported by examination of the GRAPE record (often a proxy for carbonate content; Mayer, 1991), which shows a trend of decreasing density in the interval from 16.5 to 14 Ma (Fig. 61B). A decrease in wet-bulk density in the deepest part of the section (where compaction should be greatest) can only be explained by the presence of siliceous microfossils, which have low grain densities and maintain an open structure even under substantial overburden. As the site moved out from under the very productive waters associated with the equator (from 16.5 to 14 Ma), the proportion of siliceous microfossils decreased, resulting in lower overall sedimentation rates. Sedimentation after this time (14–11.5 Ma) was dominated by the deposition of carbonate, indicative of a moderately productive environment coupled with a relatively deep CCD.

The interval between 9.5 and 10.5 Ma was marked by a significant transition in sedimentation. Sedimentation rates decrease to about 15 m/m.y. over this interval, and the sediment section is characterized by a transition between high carbonate sediments of the middle Miocene to the more siliceous clay sediments of the late Miocene. This transition in sediment type is well characterized by the color reflectance data (Fig. 62), in which the red and near-infrared bands show a marked increase that is associated with the more reddish appearance of the sediment. The sediment over this interval is a clay and radiolarian clay sediment with manganese oxides. These sediments are consistent with reduced sedimentation rates between 8.5 and 10.5 Ma (Fig. 61A) and oxidized conditions, as opposed to the previous sedimentary environment. The timing of this carbonate decrease may be coincident with similar ones noted in many areas of the Pacific Ocean and may be a manifestation of a major oceanographic event that affected the position of the CCD (see discussion in Site 844, "Sedimentation Rates" section, or Theyer et al., 1989). In addition, chemical analyses indicate elevated Fe/Al ratios in this interval, which suggests a possible

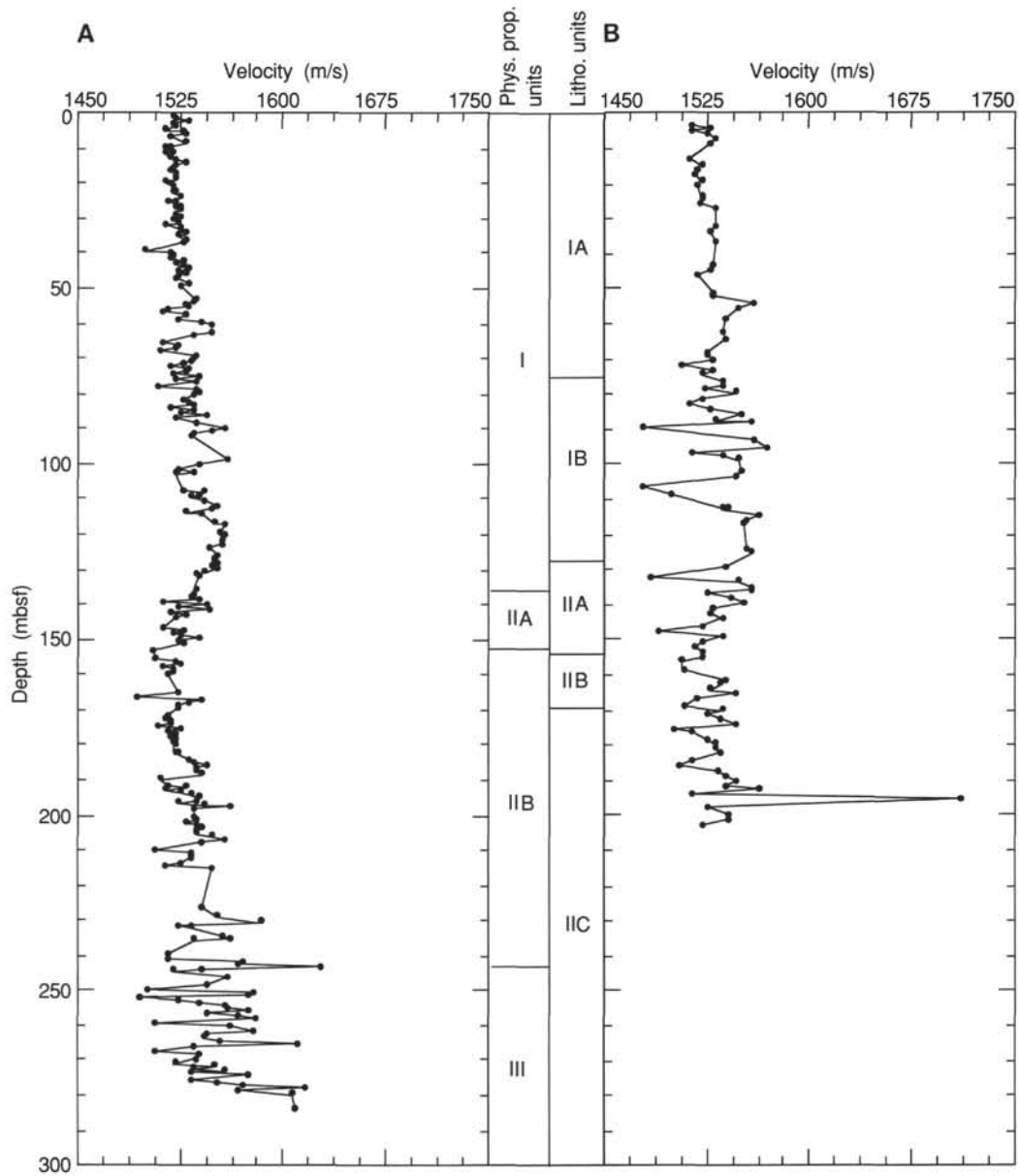


Figure 49. Velocity (m/s) vs. depth for Holes 845A (A) and 845B (B). Physical property and lithologic units are shown.

hydrothermal component in this section, as compared to other sediments of Site 845.

The oxidized character of the sediment section in this interval is also paralleled by a marked increase in magnetic susceptibility (Fig. 61C), which also coincides with the beginning of the interval in which paleomagnetic stratigraphy could be established for the site. Throughout this entire interval, the paleolatitude of the site was about 6°N ; thus, the site was well away from the influence of equatorial divergence. Detailed sedimentological, geochemical, and paleoceanographic studies of this and other sites of the eastern transect should help resolve the nature of this transition.

Sedimentation during the late Miocene to late Pliocene was characterized by mixtures of radiolarians, diatoms, and clays. Sedimentation rates vary between about 10 and 20 m/m.y., with the average for the interval (1.6–8.5 Ma) of 15 m/m.y. Color reflectance (Fig. 62) and sediment density data (Fig. 61B) show the relatively uniform nature of the sediments, but carbonate data do demonstrate short intervals of

increased carbonate content in this otherwise biogenic silica-dominated sequence (see Fig. 42).

This interval of late Miocene to late Pliocene sedimentation was terminated by a marked increase in sedimentation rates during the Pleistocene. This increase in sedimentation rate was associated with a marked increase in organic carbon accumulation, but not with an increase in the carbonate content of the sediment (see Fig. 42). The late Pliocene and Pleistocene interval was also one in which magnetic susceptibility was much reduced (Fig. 61C), and we could not define a paleomagnetic stratigraphy. A decrease in susceptibility seems to precede an increase in sedimentation; comparison with Site 844 shows that this interval was marked by a similar decrease in susceptibility. Thus, the susceptibility signal in Site 845 during this interval may have contained both a primary signal of magnetic mineral accumulation, as well as a diagenetic signal associated with increased organic carbon degradation and reducing conditions in the youngest part of the sediment section.

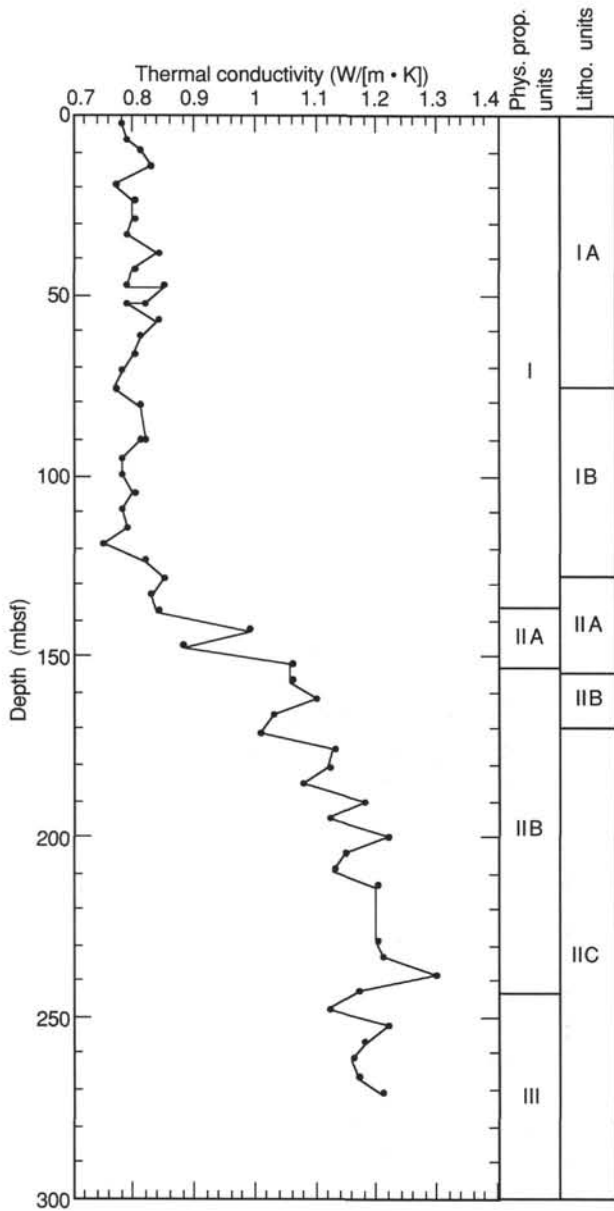


Figure 50. Thermal conductivity (W/[m • K]) for Hole 845A. Physical property and lithologic units are shown to the right.

The marked increase in sedimentation during the Pleistocene may have been associated with the movement of the site to near its present latitudinal position at the boundary between the North Equatorial Current and the North Equatorial Countercurrent, where off-equator divergence takes place, which would have helped to enhance surface production and helped contribute to the increased accumulation of organic carbon and biogenic siliceous sediments. In addition, we may be seeing the influence of the eastern boundary current. Again, detailed shore-based studies will be necessary to resolve these questions.

Geochemical analyses revealed little gas or sulfate reduction in the sedimentary section; a surprising fact, given the concentration of organic matter. The absence of sulfate reduction (and thus methanogenesis) may be the result of the initial screening of organic matter by aerobic microorganisms that rendered the remaining organic matter unusable by anerobic microbes or, the inaccessibility of organic matter interwoven with skeletal matrices to microorganisms.

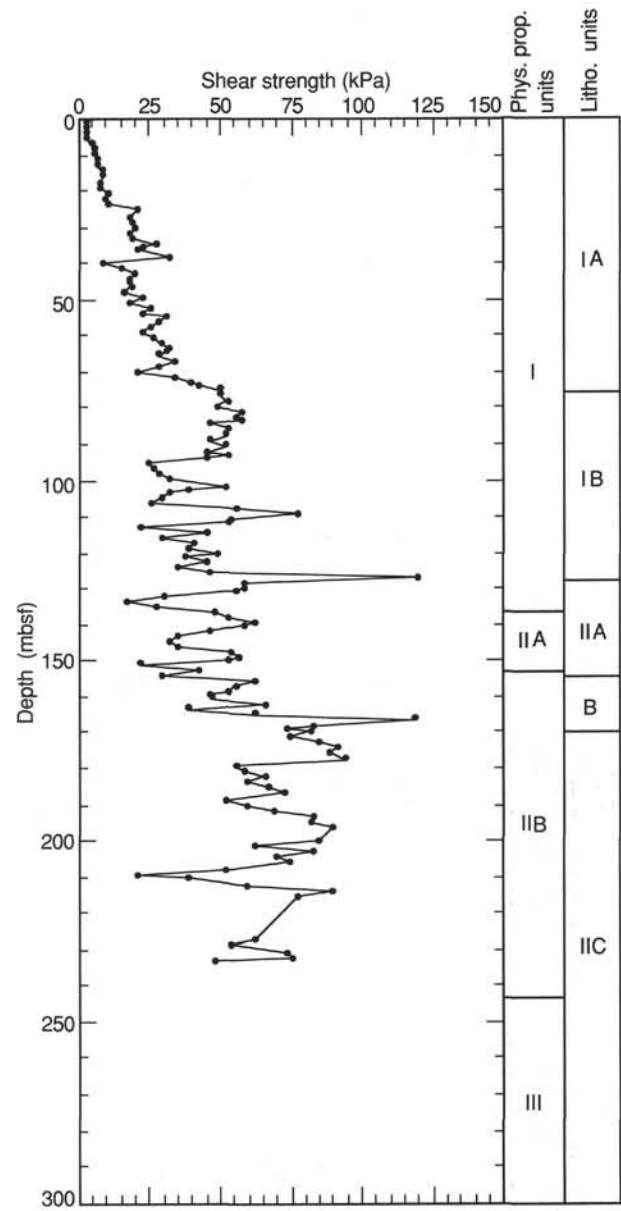


Figure 51. Undrained shear strength (kPa) for Hole 845A. Physical property and lithologic units are shown to the right.

Of critical importance to paleoceanographic and sedimentologic studies of the eastern equatorial Pacific Ocean are the paleomagnetic results from Site 845. Excellent paleomagnetic stratigraphy was determined that spanned the middle Miocene to middle Pliocene (about 13.4 to 2.7 Ma). This high-resolution record represents a unique sequence that should prove of great value for calibrating biostratigraphic datums to an absolute age scale. In addition, this high-resolution sequence contains three short normal polarity features not recognized in accepted polarity time scales. Should these features be further verified, they might provide important new information not only for paleomagnetic stratigraphy, but also about the behavior of Earth's magnetic field.

REFERENCES

- Archie, G. E., 1942. The electrical resistivity log as an aid in determining some reservoir characteristics. *Trans. AIME*, 146:54-62.

Table 20. Well log data from Hole 845A.

Log type	Depth mbsf ^a
Resistivity	97.1–280.4
Bulk density	92.3–278.6
Sonic velocity	77.3–272.4
Sonic waveforms	77.3–272.4
Gamma ray/ U-Th-K	0–281.2
Aluminum	0–273.3
Geochemistry	0–288.7
Caliper	72.5–290.9
Formation microscanner	72.5–288.0
LDGO temperature	0–290.9

Note: Intervals represent depths in borehole of good logging measurements. Values assume seafloor is at 3317.9 mbrf (meters below rig floor). A common depth scale for all logs was obtained by shifting the FMS logs (formation microscanner and caliper) downward by 2.0 m.

Auboin, J., von Huene, R., et al., 1982. *Init. Repts. DSDP*, 67: Washington (U.S. Govt. Printing Office).

Barron, J. A., 1985. Late Eocene to Holocene diatom biostratigraphy of the equatorial Pacific Ocean, Deep Sea Drilling Project Leg 85. In: Mayer, L., Theyer, F., Thomas, E., et al., *Init. Repts. DSDP*, 85: Washington (U.S. Govt. Printing Office), 413–456.

Elderfield, H., and Gieskes, J. M., 1982. Sr isotopes in interstitial waters of marine sediments from Deep Sea Drilling Project cores. *Nature*, 333:493–497.

Gieskes, J. M., 1974. Chemistry of interstitial waters of marine sediments. *Annu. Rev. Earth Planet. Sci.*, 3:433–394.

Hamilton, E. D., 1976. Variations of density and porosity with depth in deep-sea sediments. *J. Sediment. Petrol.* 46:280–300.

Harrison, W. E., Hesse, R., and Gieskes, J. M., 1982. Relationship between sedimentary facies and interstitial water chemistry of slope, trench, and Cocos Plate sites from the Middle America Trench transect, active margin off Guatemala, Deep Sea Drilling Project Leg 67. In Aubouin, J., von Huene, R., et al., *Init. Repts. DSDP*, 67: Washington (U.S. Govt. Printing Office), 603–613.

Hey, R., 1977. Tectonic evolution of the Cocos–Nazca spreading center. *Geol. Soc. of Am. Bull.*, 88:1404–1420.

Hey, R., Johnson, L., and Lowrie, A., 1977. Recent plate motions in the Galapagos area. *Geol. Soc. Am. Bull.*, 88:1385–1403.

Hill, P. R., and Marsters, J. C., 1990. Controls on physical properties of the Peru continental margin sediments and their relationship to deformation.

In Suess, E., von Huene, R., et al., *Proc. ODP, Sci. Results*, 112: College Station, TX (Ocean Drilling Program), 623–632.

Keller, G. V., 1982. Electrical properties of rocks and minerals. In Carmichael, R. S. (Ed.), *Handbook of Physical Properties of Rocks, Vol. 1*: Boca Raton (CEC Press), 217–298.

Klitgord, K. D., and Mammerickx, J., 1982. Northern East Pacific Rise: magnetic anomaly and bathymetric framework. *J. Geophys. Res.*, 87(B8):6725–6750.

Lovell, M., 1984. Thermal conductivity and permeability assessment by electrical resistivity measurements in marine sediments. *Mar. Geotech.*, 6:205–240.

Mammerickx, J., and Klitgord, K. D., 1982. Northern East Pacific Rise: from 25 m.y. B.P. to the present. *J. Geophys. Res.*, 87(B8):6751–6759.

Martini, E., 1971. Standard Tertiary and Quaternary calcareous nannoplankton zonation. *Proc. 2nd Int. Conf. on Planktonic Microfossils (Roma 1970)*: Rome (Ed. Tecnoscienza), 739–785.

Martinson, D. G., Menke, W., and Stoffa, P., 1982. An inverse approach to signal correlation. *J. Geophys. Res.*, 87:4807–4818.

Mayer, L. A., 1992. Extraction of high-resolution carbonate data for paleoclimatic reconstruction. *Nature*, 352:148–151.

Mayer, L. A., Shipley, T. H., Theyer, F., Wilkens, R. W., and Winterer, E. L., 1985. Seismic modeling and paleoceanography at DSDP Site 574. In Mayer, L. A., Theyer, F., Thomas, E., et al., *Init. Repts. DSDP*, 85: Washington (U.S. Govt. Printing Office), 947–970.

Okada, H., and Bukry, D., 1980. Supplementary modification and introduction of code numbers to the low-latitude coccolith biostratigraphic zonation (Bukry, 1973; 1975). *Mar. Micropaleontol.*, 5:321–325.

Theyer, F., Vincent, E., and Mayer, L. A., 1990. Sedimentation and paleoceanography of the central equatorial Pacific. In Winterer, E. L., Hussong, D. M., and Decker, R. (Eds.), *The Geology of North America, N, The Eastern Pacific Ocean and Hawaii*. Geol. Soc. of Am., 347–372.

Urmos, J., Wilkens, R., Bassinot, F., Lyle, M., Marsters, J., and Mayer, L., in press. Laboratory and well-log velocity and density measurements from the Ontong Java Plateau: new *in-situ* corrections to laboratory data for pelagic carbonates.

van Andel, T. H., Heath, G. R., and Moore, T. C., 1975. Cenozoic tectonics, sedimentation, and paleoceanography of the central equatorial Pacific. *Geol. Soc. Am. Mem.*, 143:1–134.

Wilkens, R., McLellan, P., Moran, K., Schoonmaker-Tribble, J., Taylor, E., and Verdzo, E., 1990. Diagenesis and dewatering of clay-rich sediments, Barbados accretionary prism. In Moore, J. C., Mascle, A., et al., *Proc. ODP, Sci. Results*, 110: College Station TX (Ocean Drilling Program), 309–320.

Wood, A. B., 1930. *A Textbook of Sound*: London (G. Bell and Sons).

Wyllie, M. R., Gardner, A. R., and Gardner, L. W., 1956. Elastic wave velocities in herogenous and porous media. *Geophysics*, 21:41–70.

Ms 138A-110

NOTE: For all sites drilled, core description forms (“barrel sheets”) and core photographs have been reproduced on coated paper and can be found in Section 4, beginning on page 397. Forms containing smear-slide data can be found in Section 5, beginning on page 663.

Formation microscanner images for this site are presented on microfiche in the back of Part 2.

Table 21. Means and standard deviations of physical property and geochemical measurements in each log unit.

Tool type	Unit I		Unit II		Unit III	
	Mean	Std. Dev.	Mean	Std. Dev.	Mean	Std. Dev.
Physical property tool string						
Depth (mbsf)	77–151		151–207		211–269	
Velocity (km/s)	1.51	0.004	1.53	0.019	1.66	0.03
Density (g/cm ³)	1.3	0.032	1.51	0.047	1.59	0.035
Gamma-ray (API units)	8.68	2.28	4.71	0.796	4.11	0.928
Resistivity (ohm-m)	0.467	0.027	0.674	0.044	0.829	0.049
FF	1.27	0.077	1.83	0.111	2.24	0.124
Geochemistry tool string						
Depth (mbsf)	80–143		143–207		207–269	
Calcium	0.015	0.021	0.06	0.022	0.094	0.024
Silica	0.0087	0.0146	0.00034	0.0139	0.0052	0.0163

FF = formation factor.

Table 22. Relationships between formation factor and porosity in the three logging units.

Log unit	Parameter
1	$FF = 0.94 F^{-1.45}$
2	$FF = 1.01 F^{-1.69}$
3	$FF = 1.39 F^{-1.13}$

FF = formation factor; F = porosity.

Table 23. Differences between log density values and density values determined gravimetrically and with the GRAPE for Hole 845A.

Depth (mbsf)	Log density – GRAPE density	Log Density – gravimetric density
72–140	0.085 ± 0.032	0.134 ± 0.031
140–203	-0.005 ± 0.034	0.073 ± 0.05
230–278	0.03 ± 0.054	0.095 ± 0.063

Table 24. Summary of traveltimes, depth, and ages for Site 845 reflectors.

Reflector	Traveltime (s)	Synthetic depth (m)	Depth (mbsf)	Depth (mcd)	Age (Ma)
R1	0.012	9.00	7.30	7.30	0.24
	0.020	15.00	9.00	9.80	0.33
R2	0.023	17.30	18.00	18.90	0.73
	0.028	21.00	21.00	22.60	0.91
R3	0.055	41.30	39.70	43.20	2.11
	0.061	45.80	41.30	44.80	2.16
R6	0.103	77.60	76.80	84.80	5.21
	0.107	79.20	79.10	89.00	5.44
R7	0.114	86.00	86.20	94.70	5.79
	0.121	90.30	89.00	97.90	6.01
R8	0.129	97.30	103.90	115.20	7.07
	0.133	100.30	105.60	116.90	7.10
R9	0.160	120.80	128.00	142.00	8.54
	0.166	125.40	129.00	143.00	8.63
R12A	0.199	150.30	150.10	168.90	10.71
	0.203	153.30	153.90	172.70	10.97
R12B	0.208	157.00	159.70	179.00	11.29
	0.217	163.90	163.60	182.80	11.50
R13	0.228	172.20	172.10	192.80	11.97
	0.231	174.50	175.20	195.90	12.09
R15	0.266	201.60	200.30	225.50	13.18
	0.269	204.00	204.50	229.70	13.26
R16	0.276	209.40	208.50	233.70	13.63
	0.280	212.80	211.80	237.00	13.82
R19	0.312	239.20	239.10	264.30	15.28
	0.314	241.00	242.00	267.20	15.54
R21	0.324	249.30	249.20	274.40	15.95
	0.328	252.60	253.70	278.90	16.05
R22	0.334	257.60	255.40	280.60	16.10
	0.336	259.30	257.40	282.60	16.14
Basement	0.370	291.00	291.00	317.00	16.76

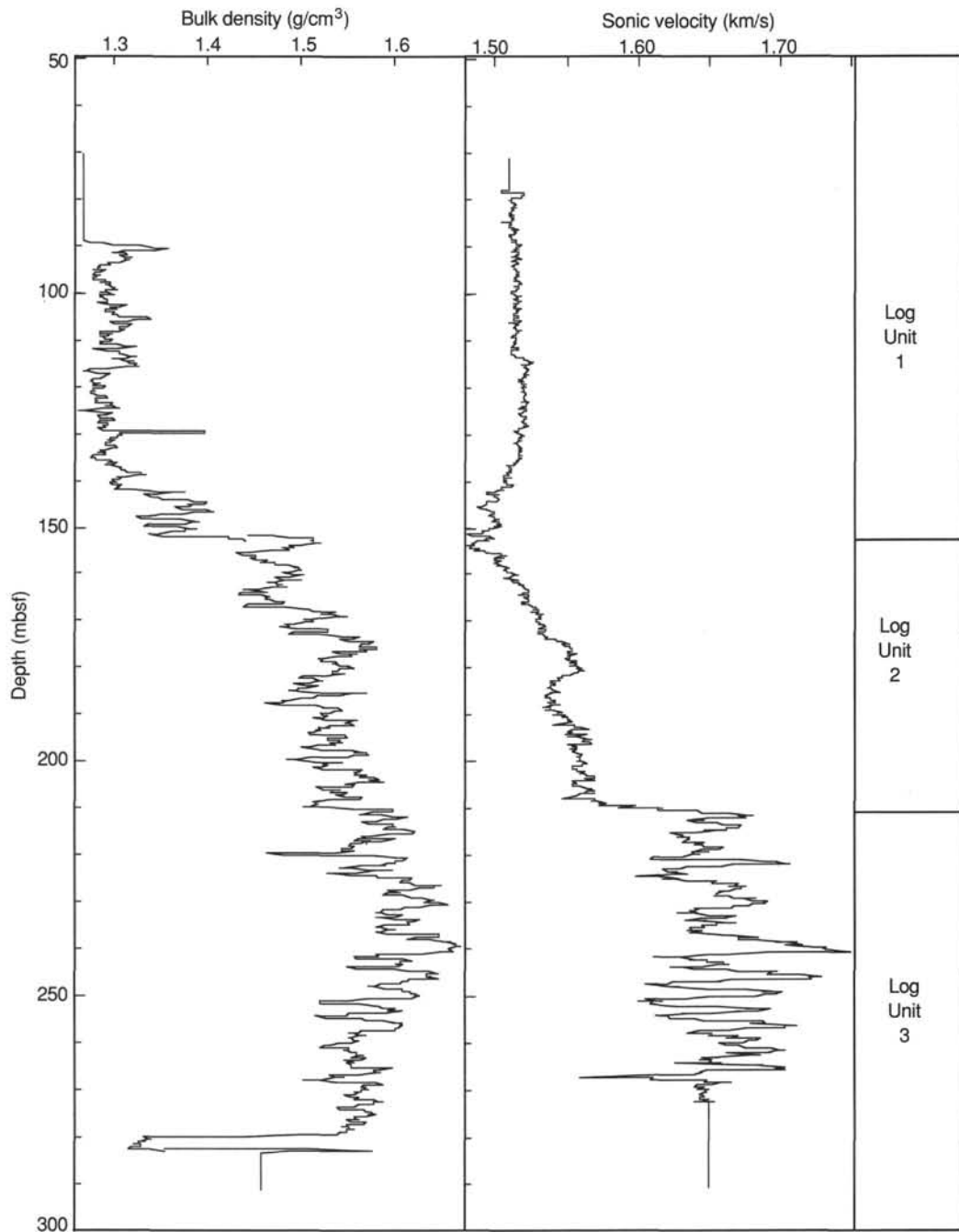


Figure 52. Logging bulk density and velocity vs. depth. Low density values near 280 mbsf are probably dropout values. Log stratigraphic units are shown to the right.

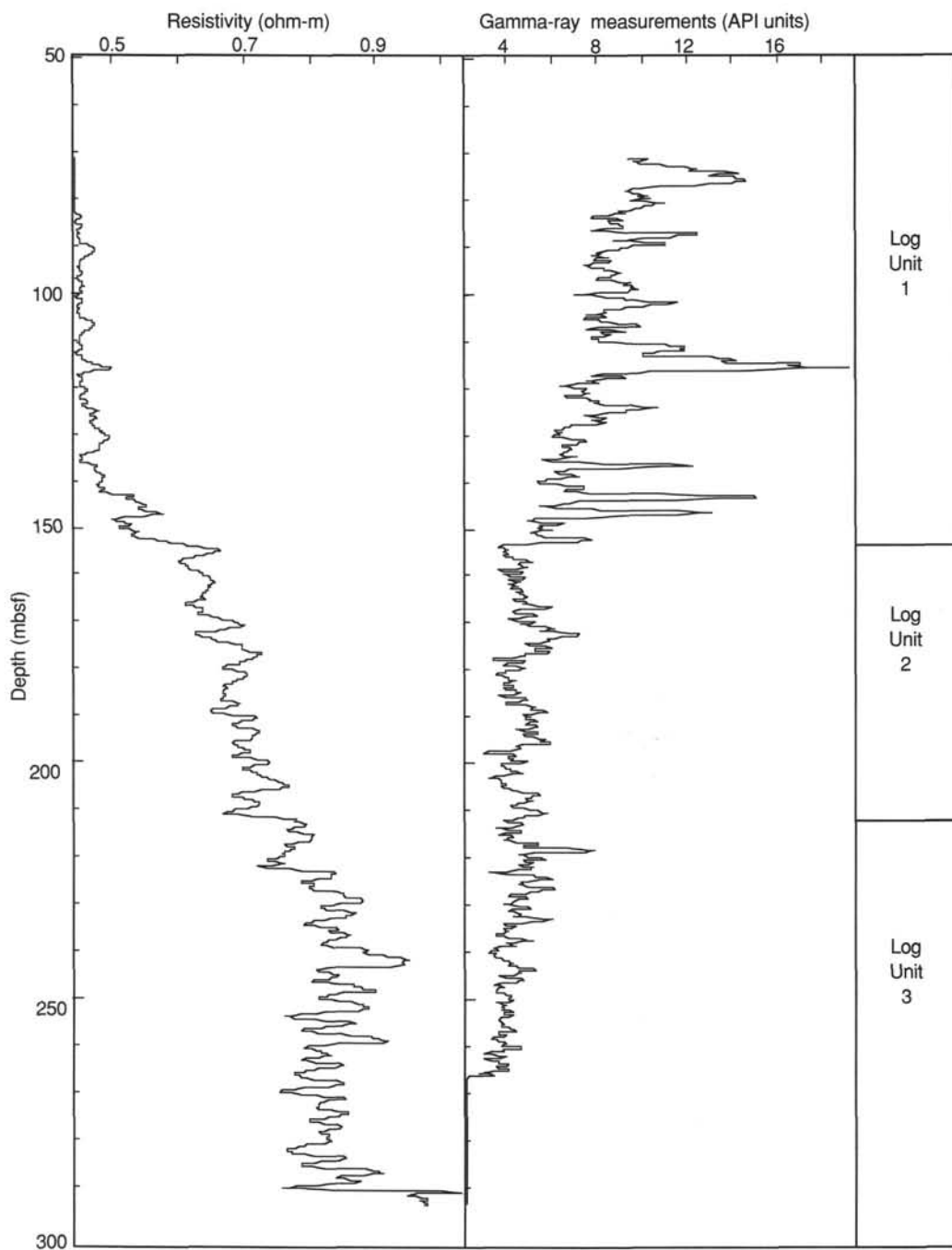


Figure 53. Resistivity and gamma-ray measurements from downhole logs vs. depth. Gamma-ray data were smoothed using a three-point Gaussian smoothing equation. Log stratigraphic units are shown to the right.

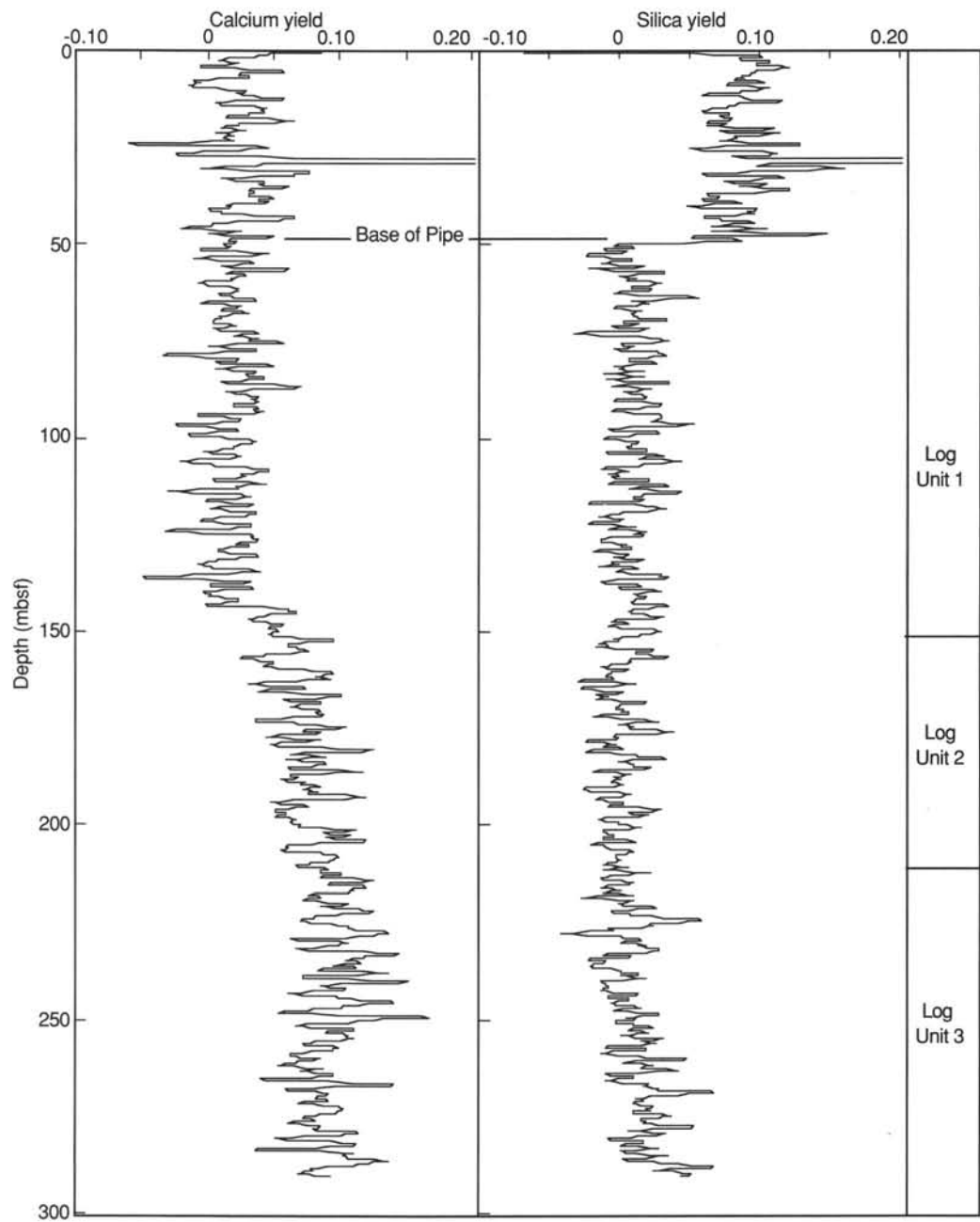


Figure 54. Calcium and silica yields (uncorrected) vs. depth. Both curves were smoothed using a five-point Gaussian relationship. Log measurements in pipe require extensive post-cruise processing. Log stratigraphic units are shown to the right.

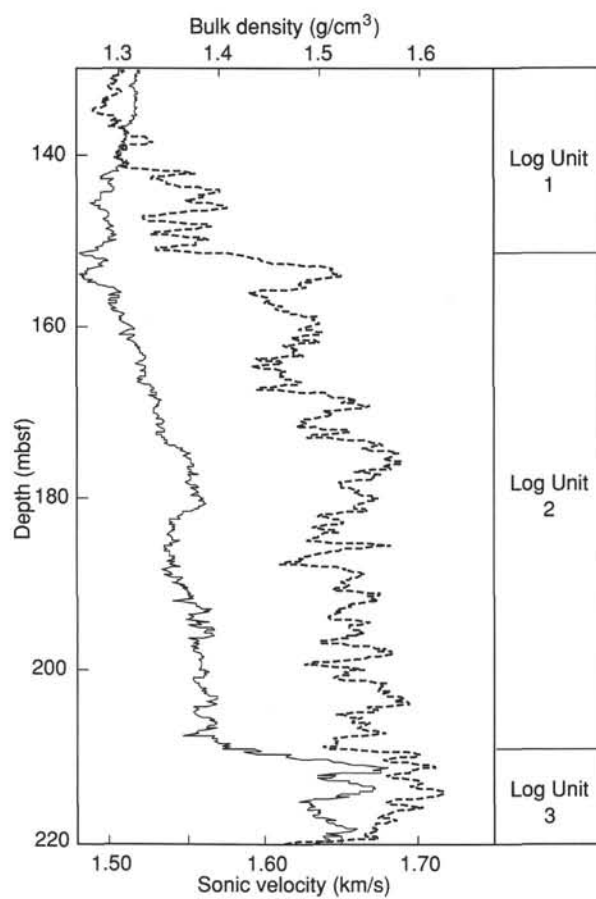


Figure 55. Bulk density (dashed curve) and velocity (solid curve) vs. depth in the interval from 130 to 220 mbsf. This figure clearly illustrates the abrupt changes observed at the two log stratigraphic boundaries.

Table 25. Paleolatitudes of Site 845.

Age (Ma)	Latitude (°N)
0	9.58
1	9.38
2	9.07
3	8.76
4	8.46
5	8.16
6	7.86
7	7.56
8	7.27
9	6.98
10	6.70
11	6.42
12	6.14
13	5.87
14	5.60
15	5.33
16	5.07
17	4.81

Pole of rotation = 21.9°N, 115.5°W; angular velocity = -0.948°/m.y.

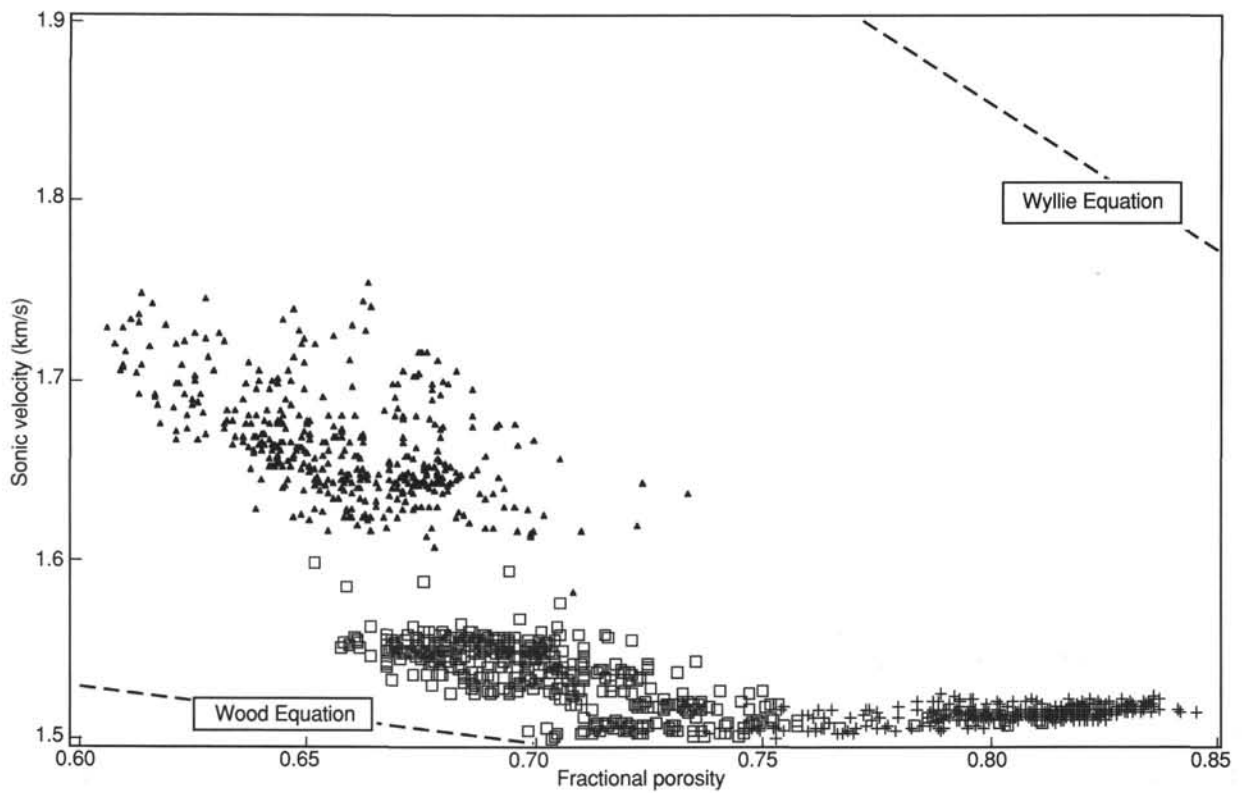


Figure 56. Velocity vs. porosity in the three log stratigraphic units; Unit 1 = crosses, Unit 2 = open squares, Unit 3 = solid triangles. The Wood and Wyllie relationships are included as dashed lines. Note the distinct separation of Unit 3 from Units 1 and 2.

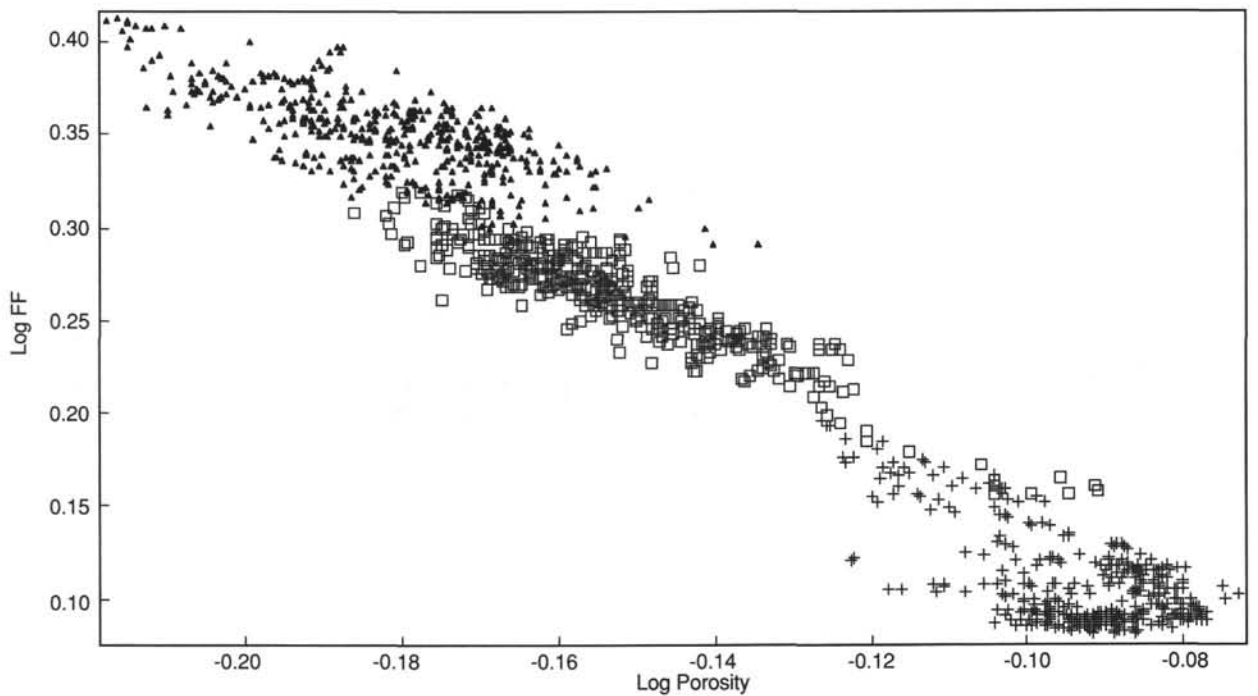


Figure 57. Logarithm FF vs. logarithm porosity for the three log units (symbols are the same as Fig. 56). Unit 3 has a different trend relative to the other two units. In addition, a mixture of lithologies within Unit 1 results in two separate and distinct trends.

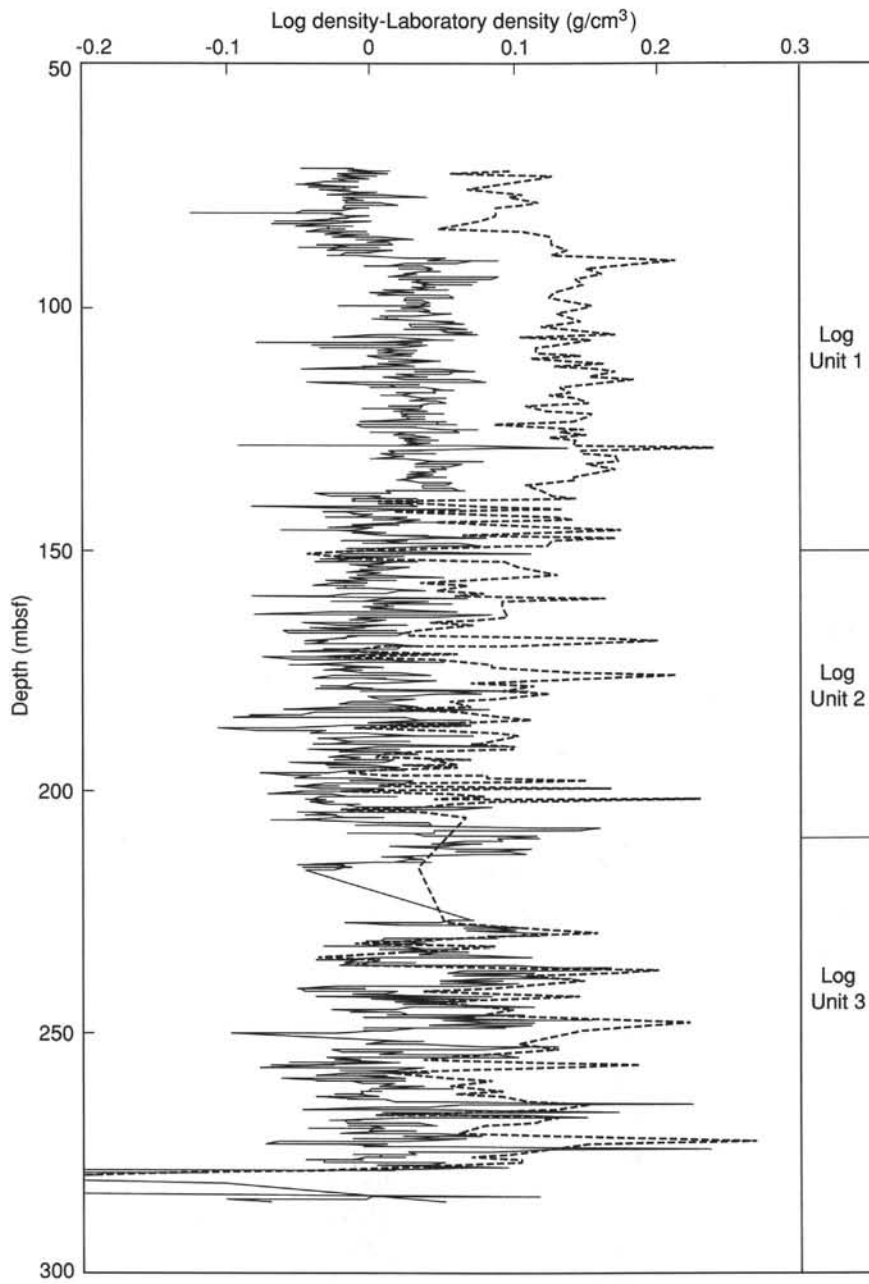


Figure 58. Log densities minus GRAPE values (solid line) and gravimetric data (dashed line).

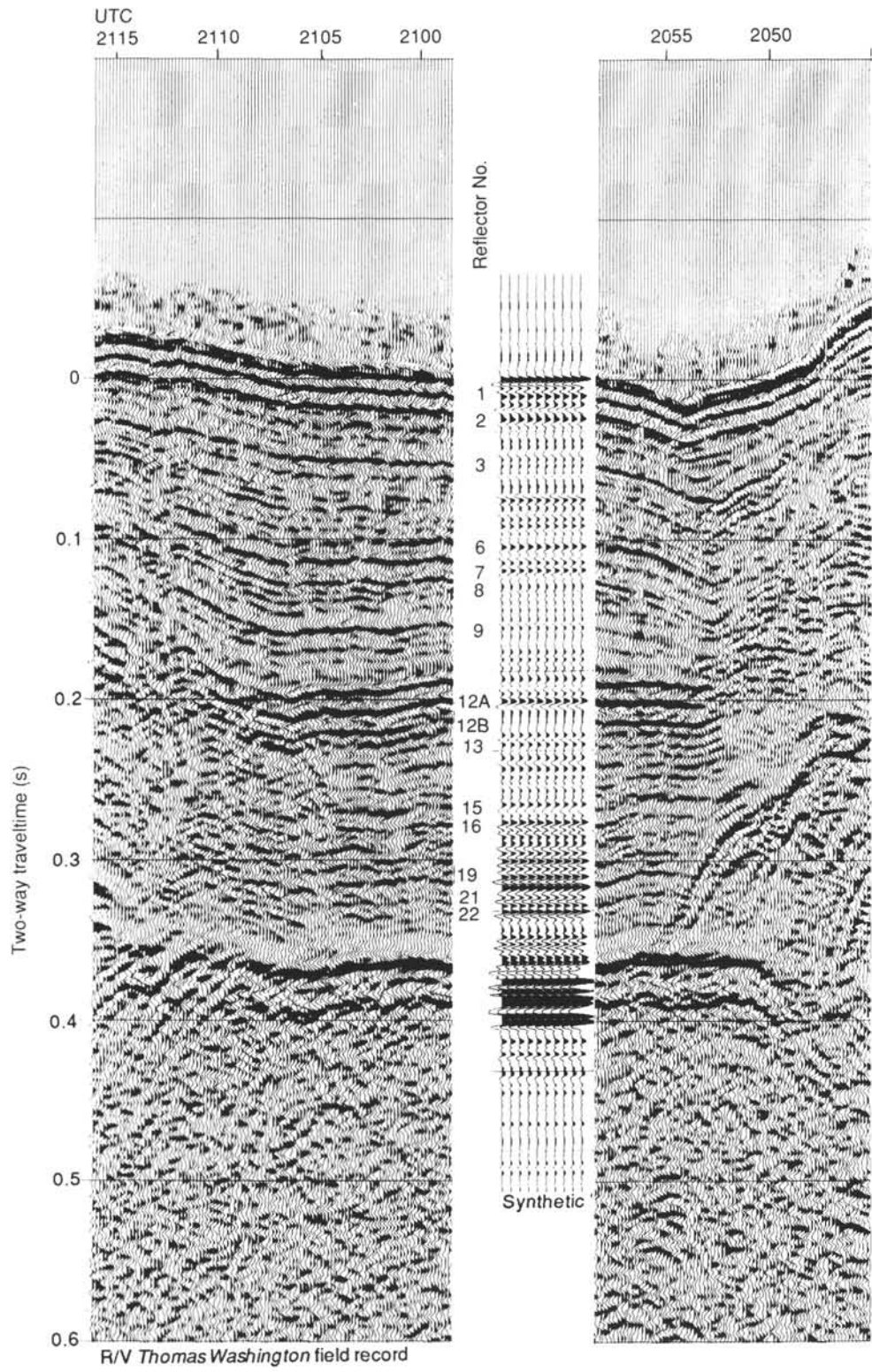


Figure 59. Comparison of synthetic seismogram with field record, Site 845.

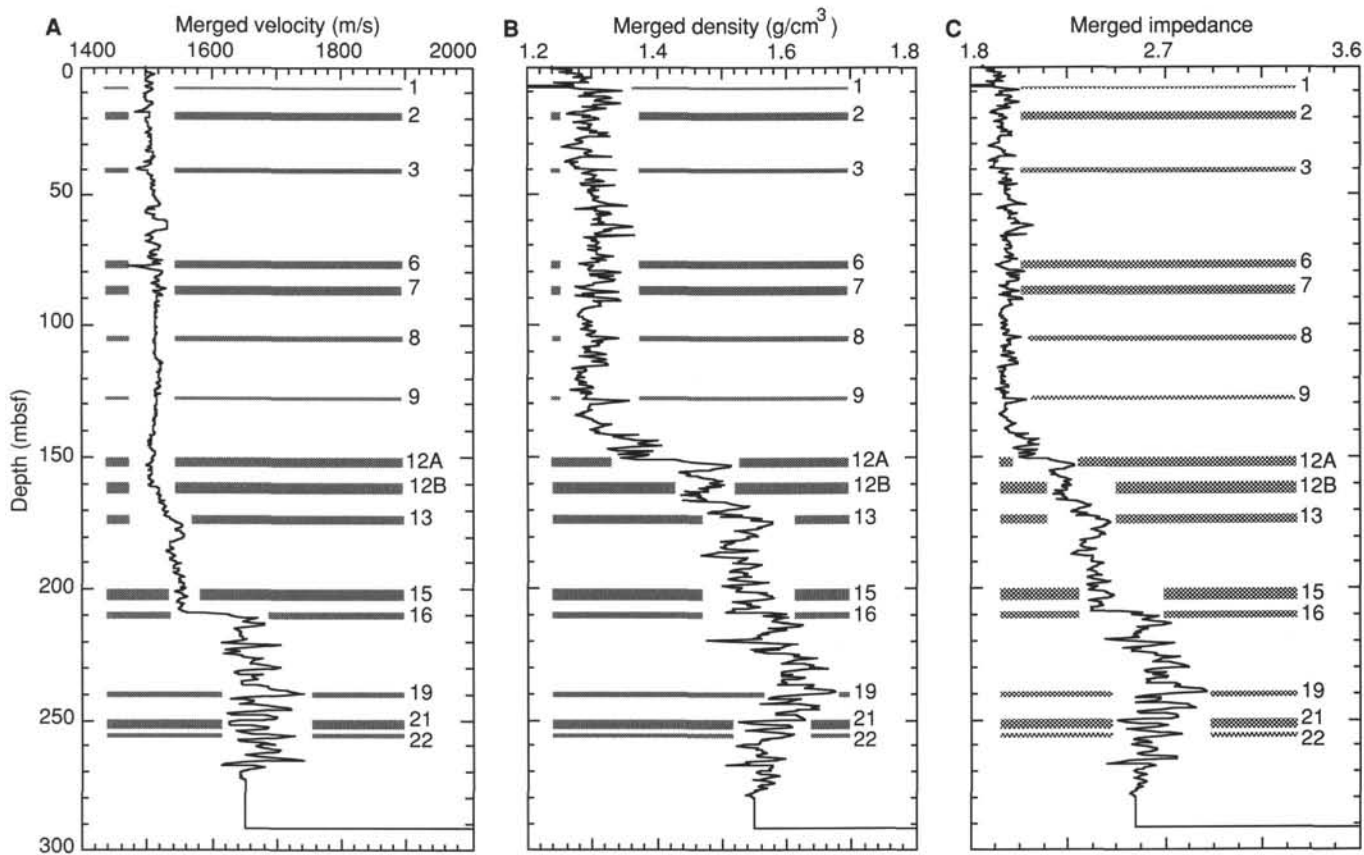


Figure 60. A. Velocity. B. Density. C. Acoustic impedance. Data used for generating Site 845 synthetic seismograms. The 15 reflectors selected from the synthetic seismogram are shown for comparison.

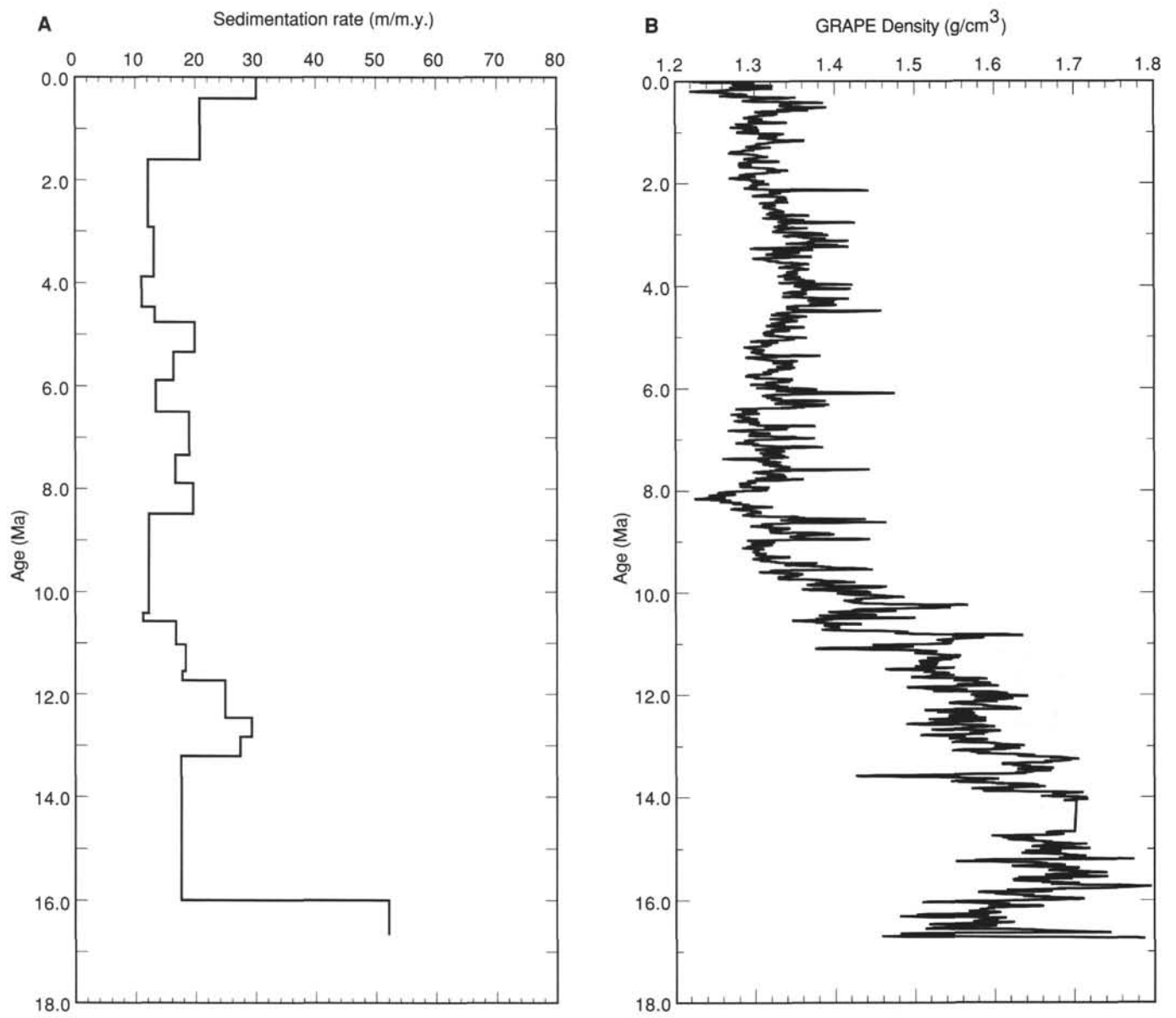


Figure 61. A. Sedimentation rate vs. sediment age. B. Sediment density vs. age. C. Sediment magnetic susceptibility vs. age.

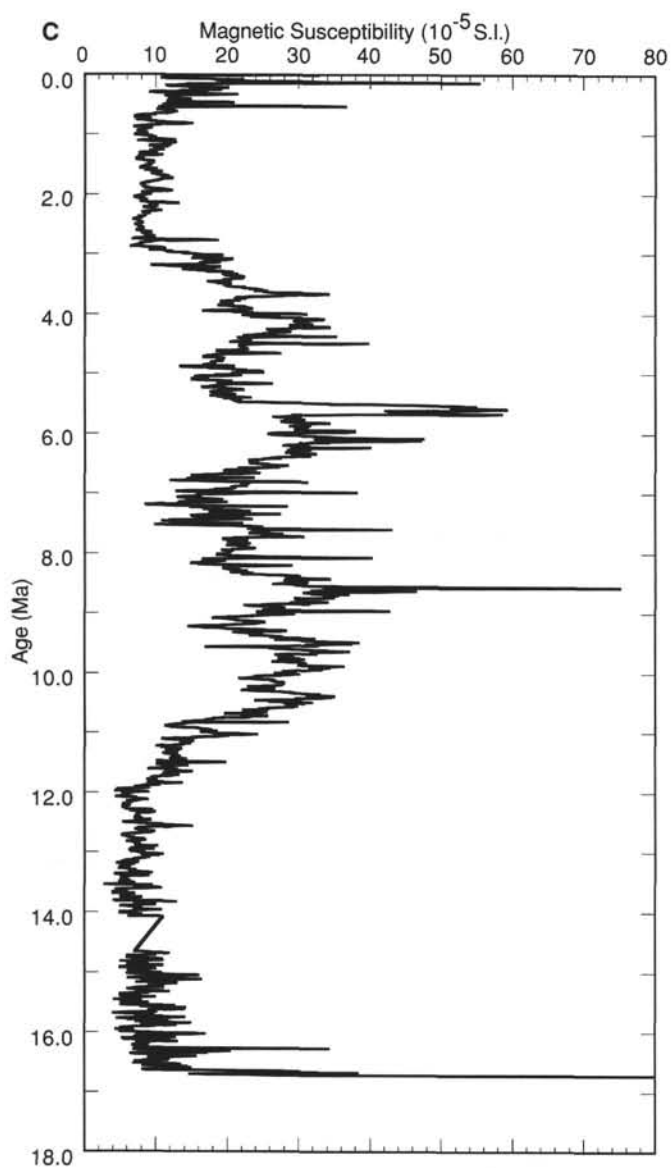


Figure 61 (continued).

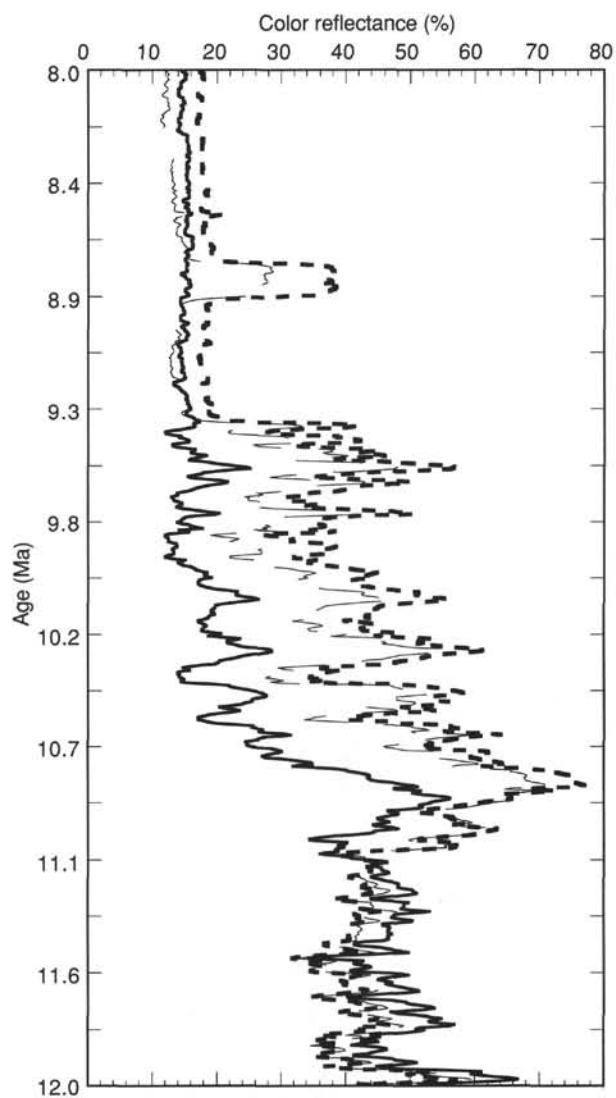
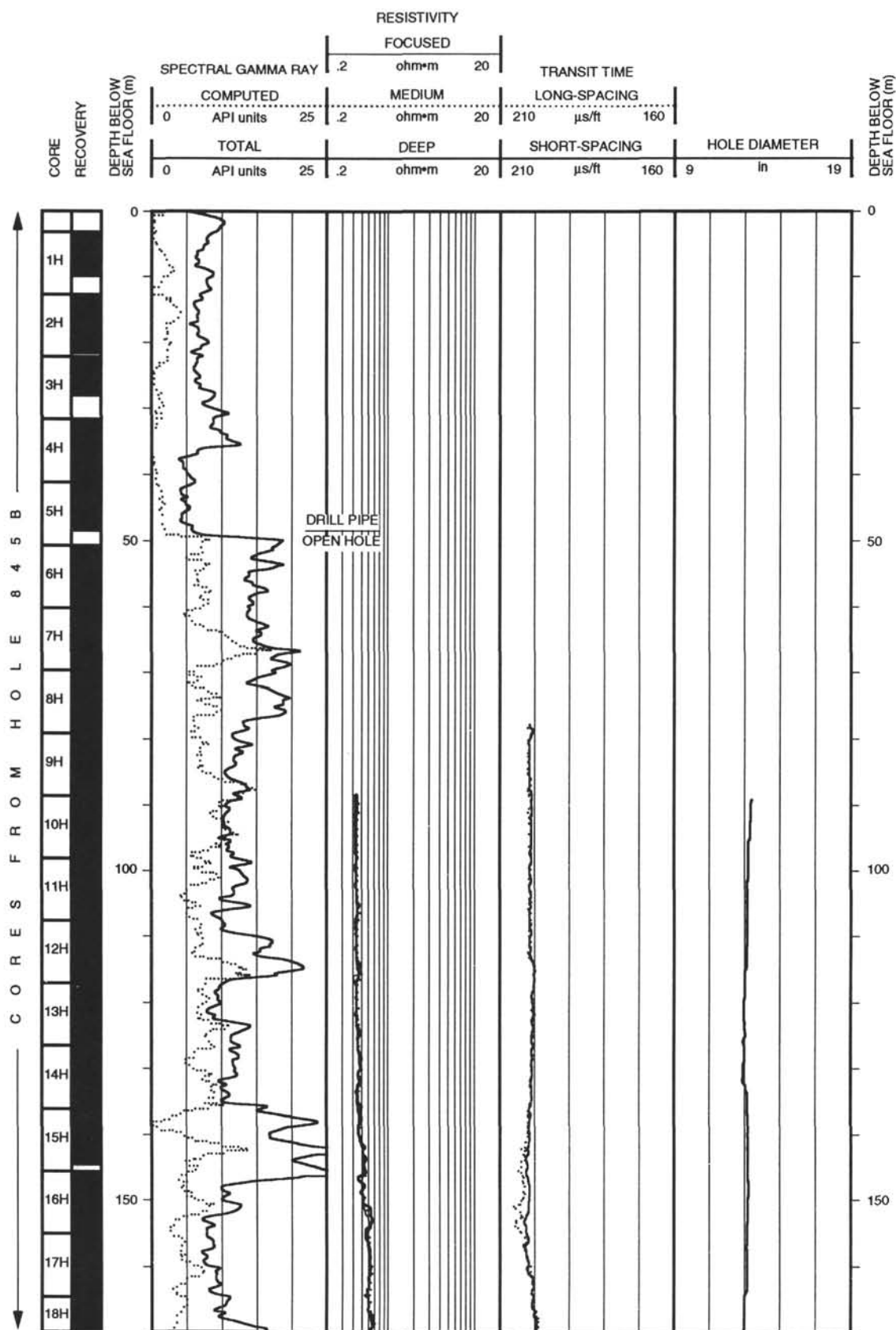
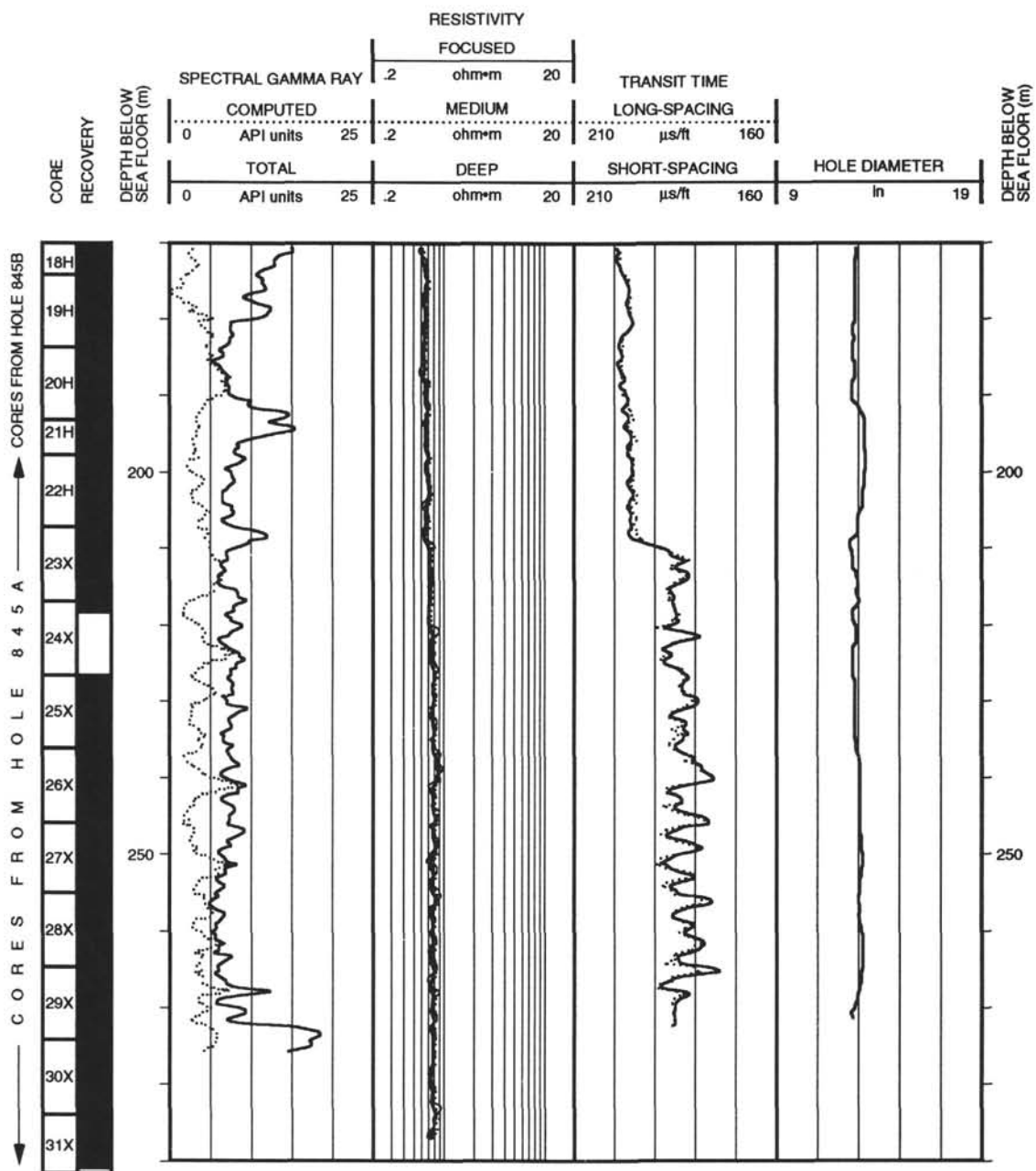


Figure 62. Color reflectance of three color bands (blue [solid], red [thin dashed], and near infrared [thick dashed line]) over the transition in sediment between 9 and 10.5 Ma.

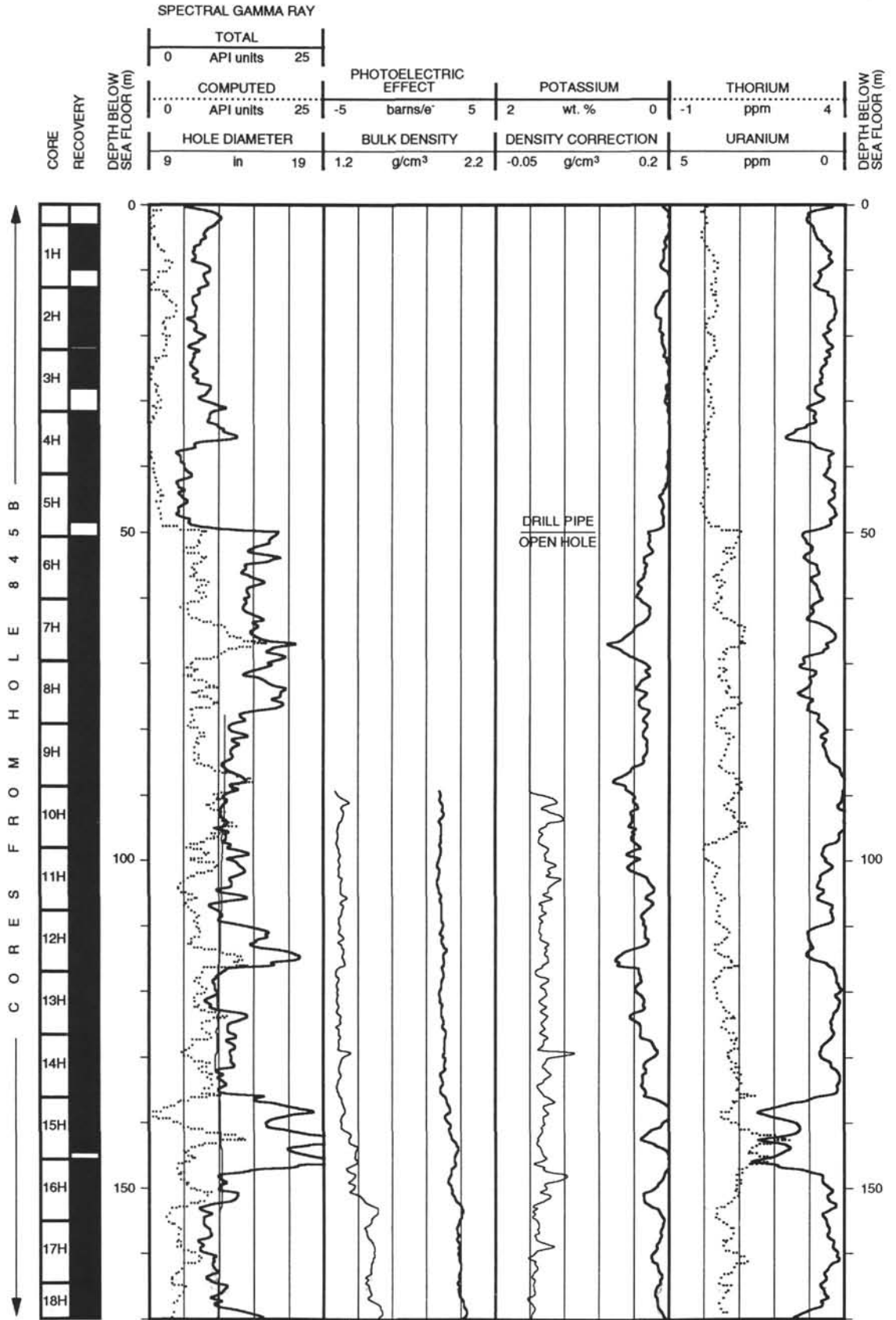
Hole 845B: Resistivity-Sonic-Natural Gamma Ray Log Summary



Hole 845B: Resistivity-Sonic-Natural Gamma Ray Log Summary (continued)

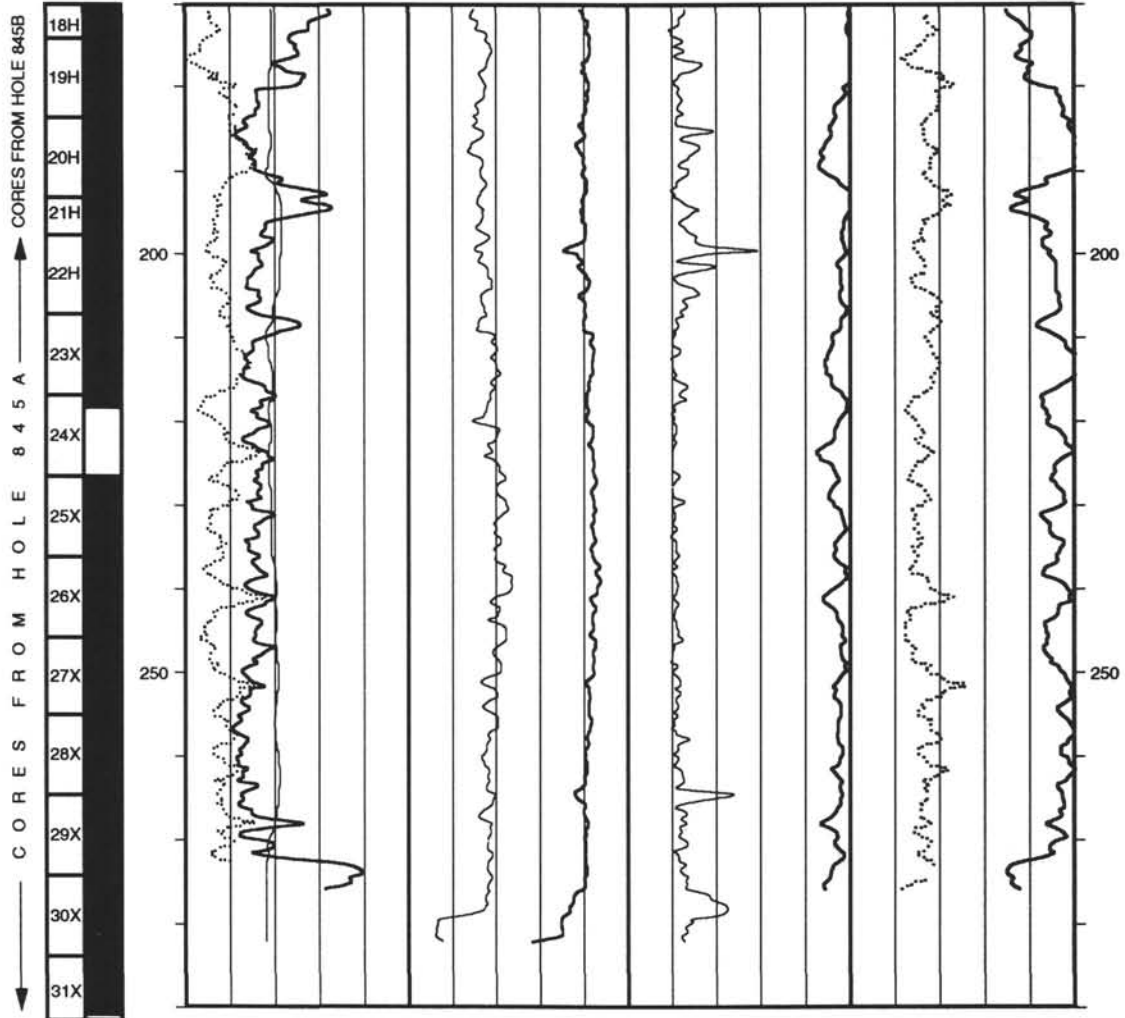


Hole 845B: Density-Natural Gamma Ray Log Summary

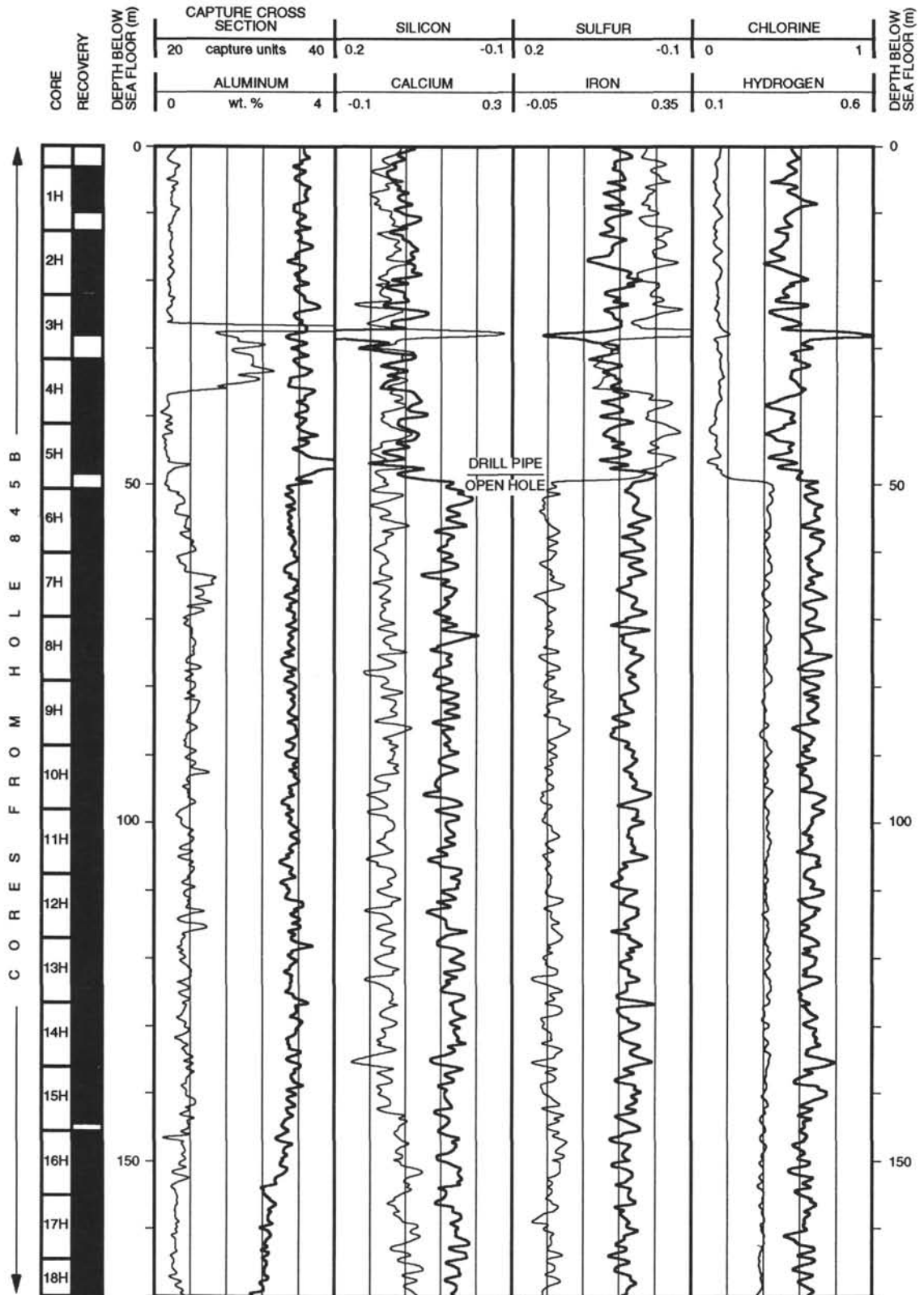


Hole 845B: Density-Natural Gamma Ray Log Summary (continued)

SPECTRAL GAMMA RAY	
TOTAL	
0	25
API units	
COMPUTED	
0	25
API units	
PHOTOELECTRIC EFFECT	
-5	5
barns/e ²	
POTASSIUM	
2	0
wt. %	
THORIUM	
-1	4
ppm	
HOLE DIAMETER	
9	19
in	
BULK DENSITY	
1.2	2.2
g/cm ³	
DENSITY CORRECTION	
-0.05	0.2
g/cm ³	
URANIUM	
5	0
ppm	



Hole 845B: Geochemical Log Summary



Hole 845B: Geochemical Log Summary (continued)

